MICROCOPY RESOLUTION TEST CHART

NATIONAL BUREAU OF STANDARDS

LEVEL II ②

AN EXPERIMENTAL INVESTIGATION OF THE INTERACTION
BETWEEN A KÁRMÁN VORTEX STREET AND A PREMIXED LAMINAR FLAME

Izak Namer

DTIC
ELECTE
S DEC 30 1980 D
D

COLLEGE OF ENGINEERING
UNIVERSITY OF CALIFORNIA, Berkeley

80 12 29 111

SECURITY CLASSIFICATION OF THIS PAGE (When Data Entered)

REPORT DOCUMENTATION PAGE	READ INSTRUCTIONS BEFORE COMPLETING FORM

1. REPORT NUMBER	2. GOVT ACCESSION NO.	3. RECIPIENT'S CATALOG NUMBER
AFOSR-TR-80-1325	AD-A093 419	

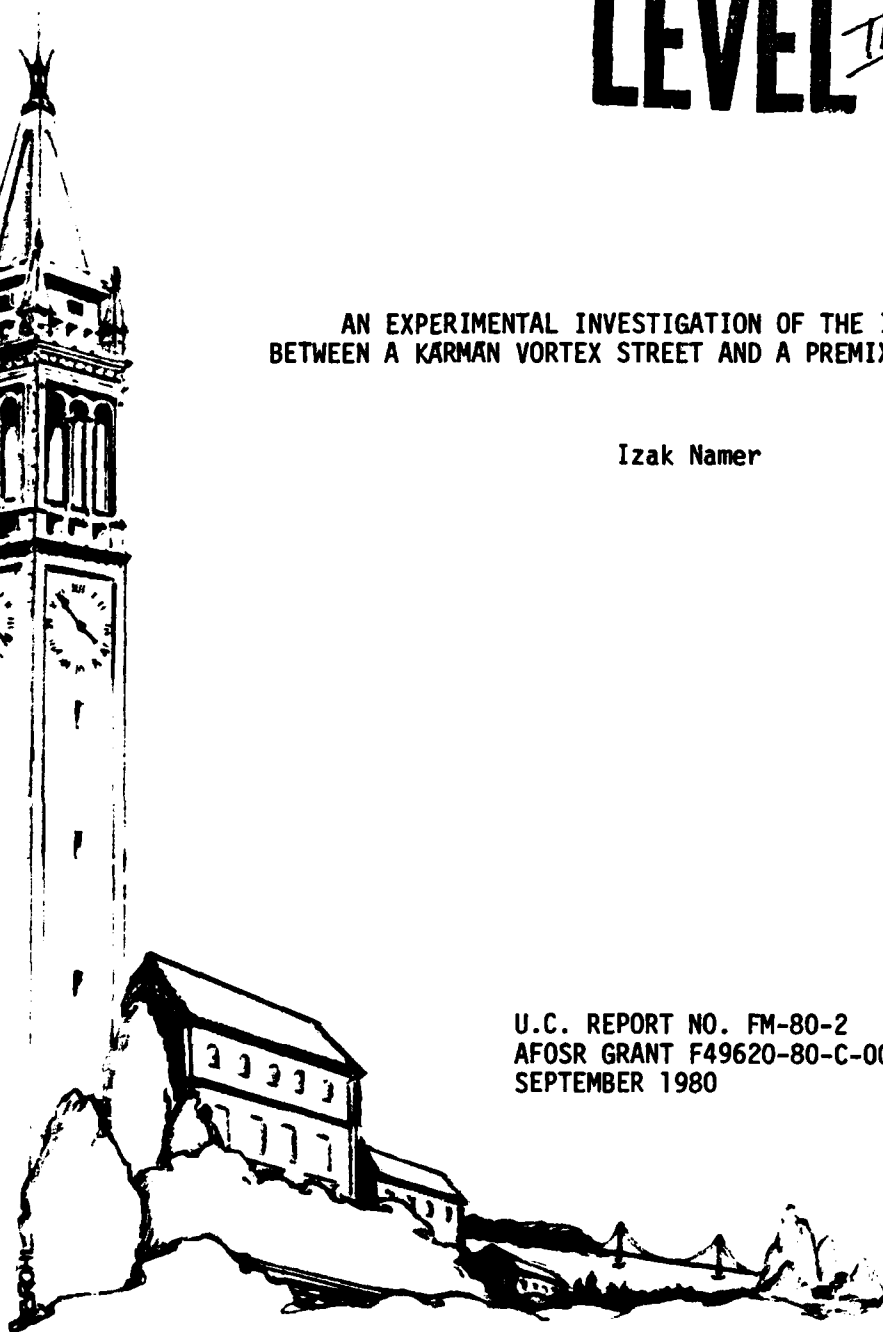| 4. TITLE (and Subtitle)	5. TYPE OF REPORT & PERIOD COVERED
AN EXPERIMENTAL INVESTIGATION OF THE INTERACTION BETWEEN A KARMAN VORTEX STREET AND A PREMIXED LAMINAR FLAME.	Interim rept.
	6. PERFORMING ORG. REPORT NUMBER FM-80-2

7. AUTHOR(s)	8. CONTRACT OR GRANT NUMBER(s)
Izak Namer	F49620-80-C-0065

9. PERFORMING ORGANIZATION NAME AND ADDRESS	10. PROGRAM ELEMENT, PROJECT, TASK AREA & WORK UNIT NUMBERS
UNIVERSITY OF CALIFORNIA, BERKELEY DEPARTMENT OF MECHANICAL ENGINEERING BERKELEY, CA 94720	2308/A2 61102F

11. CONTROLLING OFFICE NAME AND ADDRESS	12. REPORT DATE
AIR FORCE OFFICE OF SCIENTIFIC RESEARCH/NA BLDG. 410 BOLLING AIR FORCE BASE, D.C. 20332	September 1980
	13. NUMBER OF PAGES 111

14. MONITORING AGENCY NAME & ADDRESS(if different from Controlling Office)	15. SECURITY CLASS. (of this report)
UCB/FM-80-2	UNCLASSIFIED
	15a. DECLASSIFICATION/DOWNGRADING SCHEDULE

16. DISTRIBUTION STATEMENT (of this Report)

Approved for public release; distribution unlimited.

17. DISTRIBUTION STATEMENT (of the abstract entered in Block 20, if different from Report)

18. SUPPLEMENTARY NOTES

19. KEY WORDS (Continue on reverse side if necessary and identify by block number)

Turbulent combustion   Ensemble averaging
Vortex street
Wrinkled-laminar flame
Rayleigh scattering
Laser Doppler anemometry

20. ABSTRACT (Continue on reverse side if necessary and identify by block number)

The interaction of a premixed C_2H_4-air flame with a Kármán vortex street was studied. Laser Doppler anemometry was used for velocity measurements and Rayleigh scattering was used to measure total gas density. A reference hot-wire was used to enable phase-locked ensemble averaging to be performed on the data. The velocity measurements, for vortex shedding cylinder Reynolds numbers $(UD/\nu) \approx$ 73 and 110, indicated that the vortex street and, hence, the flow field upstream of the flame is deflected by the flame. This is due to the pressure drop across the flame which is necessary to accelerate the flow behind

(over)

DD FORM 1473 EDITION OF 1 NOV 65 IS OBSOLETE   UNCLASSIFIED

20. ABSTRACT (cont'd)

the flame. The vortices were not observed behind the flame. The combination of dilatation and increased dissipation "consumed" the vortices. Density statistics obtained from Rayleigh scattering measurements were compared with predictions by the Bray-Moss-Libby (B-M-L) model which neglects intermediate states. Density fluctuations were overpredicted by the B-M-L model by a small amount for (UD/ν) = 73 and 110. The flame was essentially a wrinkled-laminar flame for these conditions. However, for (UD/ν) = 500 the flame consisted of a distributed reaction zone and intermediate states accounted for as much as 80% of all states encountered in portions of the flame. The B-M-L model significantly overpredicted density fluctuation statistics for this condition. A qualitative comparison was made with numerical calculations by Karasalo and Namer for the time dependent interaction of a flame with an ideal Kármán vortex street and suggestions for improving the model were made. Nevertheless, considering the significant differences in details between this experiment and the numerical calculations, the general behavior of the measured and calculated flames was comparable.

Accession For	
NTIS GRA&I	X
DTIC TAB	☐
Unannounced	☐
Justification	
By	
Distribution/	
Availability Codes	
Dist	Avail and/or Special
A	

AN EXPERIMENTAL INVESTIGATION OF THE INTERACTION
BETWEEN A KARMAN VORTEX STREET AND A PREMIXED LAMINAR FLAME

Izak Namer

Submitted in partial satisfaction of the requirements for

the Ph.D. Degree

DTIC
ELECTE
DEC 30 1980
S
D
D

September 1980

UNIVERSITY OF CALIFORNIA
Department of Mechanical Engineering
Berkeley, California 94720

ABSTRACT

The interaction of a premixed C_2H_4-air flame with a Kármán vortex street was studied. Laser Doppler anemometry was used for velocity measurements and Rayleigh scattering was used to measure total gas density. A reference hot-wire was used to enable phase-locked ensemble averaging to be performed on the data. The velocity measurements, for vortex shedding cylinder Reynolds numbers (UD/ν) = 73 and 110, indicated that the vortex street and, hence, the flow field upstream of the flame is deflected by the flame. This is due to the pressure drop across the flame which is necessary to accelerate the flow behind the flame. The vortices were not observed behind the flame. The combination of dilatation and increased dissipation "consumed" the vortices. Density statistics obtained from Rayleigh scattering measurements were compared with predictions by the Bray-Moss-Libby (B-M-L) model which neglects intermediate states. Density fluctuations were overpredicted by the B-M-L model by a small amount for (UD/ν) = 73 and 110. The flame was essentially a wrinkled-laminar flame for these conditions. However, for (UD/ν) = 500 the flame consisted of a distributed reaction zone and intermediate states accounted for as much as 80% of all states encountered in portions of the flame. The B-M-L model significantly overpredicted density fluctuation statistics for this condition. A qualitative comparison was made with numerical calculations by Karasalo and Namer for the time dependent interaction of a flame with an ideal Kármán vortex street and suggestions for improving the model were made. Nevertheless, considering the significant differences in details between this experiment and the numerical calculations, the general behavior of the measured and calculated flames was comparable.

TABLE OF CONTENTS

CHAPTER 1: INTRODUCTION

In recent years the world has become conscious of the fact that traditional energy sources, i.e. fossil fuels, are finite and dwindling and that new renewable sources of energy must be found and implemented. It is imperative, in the meantime, that conservation measures be taken in order to prolong the lifetime of fossil fuel supplies. To this end, the engineering community has been required to reassess the criteria and methods for designing combustion powered power plants, whether it be a jet engine, a utility boiler, or an internal combustion engine. This reassessment has emphasized the need for a better understanding of the relationships between the combustion process and fluid mechanics which, in almost all practical combustors, consists of a turbulent flow.

The effects of fluid mechanical turbulence on premixed combustion, most apparent of which are the large increase in effective flame speeds and volumetric burning rates, have been studied both theoretically and experimentally for many years. These studies are extensively reviewed by Karlovitz [1], Scurlock and Grover [2], Williams [3], and Andrews et al. [4]. However, progress has been impeded by a limited understanding of turbulence even in isothermal flows as well as by the lack of diagnostic probes capable of providing accurate time-resolved velocity, density, temperature, and concentration fields in a combustion environment. Recently, Rayleigh scattering and laser Doppler anemometry have been developed as non-intrusive diagnostic techniques to measure space and time resolved density and velocity,

respectively [5-8]. These techniques were applied in this study to investigate the interaction of a premixed flame with a Kármán vortex street, an idealization of a turbulent flow.

Damkohler [9] was the first to study the effect of turbulence on flame propagation. He defined two limiting conditions. The first occurs at relatively low Reynolds numbers [4,10] where the length scales of the turbulence are much larger than the laminar flame thickness. The effect of turbulence in this case is simply to wrinkle an otherwise laminar flame (hence the name "wrinkled-laminar flame model") and increase the effective flame speed by increasing the flame's surface area. The second regime occurs for Reynolds numbers for which the length scales are smaller than the flame thickness. In this case the turbulence serves to increase heat and mass transport within the reaction zone. It has been suggested [11] that for this regime the effect of turbulence may be modelled by replacing molecular diffusivities by turbulent eddy diffusivities. These and other models based on the original ideas of Damkohler have had very limited success in correlating experimental data. Karlovitz et al. [12], for example, obtained results which indicate increases in burning rates not accountable by these theories and suggested that the flame was itself a source of turbulence. The concept of flame-generated turbulence has been advocated and subscribed to by various researchers [13-15], however, others [16-19] suggest there are large errors in most measurements of turbulent flame speed. Since the concept of flame-generated turbulence is invoked to explain the available data, it may be that

the data were interpreted incorrectly and the concept of flame-gene-
rated turbulence may be inappropriate. Therefore the wrinkled-laminar-
flame model may yet be a reasonable first approximation of some
turbulence-combustion interactions.

The major shortcoming of the wrinkled-laminar flame model is
that it is necessary to make assumptions about the geometry of the
wrinkling. The importance of these assumptions has been emphasized
by Clavin and Williams [20] among others [1,2,21-25]. The work done
by Markstein [21,23] and Peterson and Emmons [22] imply that the geo-
metry of wrinkling may be understood, at least in part, in terms of
flame stability. (Here flame stability refers to the growth or decay
of small perturbations and not to the flammability limits). Landau
[see Ref. 26] showed that a flame with constant flame speed is unstable
to disturbances at any wave number. However, Markstein [21] found
that assuming a dependence of the local flame speed on the local radius
of curvature, expressed mathematically as

$$S_L' = S_L(1 + \mu L/R) \qquad (1.1)$$

where S_L is the one-dimensional premixed laminar flame speed, L is a
thermal length proportional to the flame thickness, R is the radius
of curvature, and μ is the Markstein parameter, the flame was stable
to disturbances at wave numbers above some critical value. This has
been confirmed by Peterson and Emmons [22] and by the fact that stable
laminar flames can be produced. It appears that models, with suitable
modifications of the wrinkled-laminar-flame concept of turbulent flame

propagation, may be obtained given a more detailed understanding of the wrinkling process. Such models have had some success [20,27,28] but there is still a need for experimental data to test and confirm the models as well as to provide phenomenological bases for developing and improving these models. In the present study, with a view toward advancing the understanding of the interaction of turbulent eddies with flames, the interaction of an otherwise laminar flame with a two-dimensional Kármán vortex street was studied using Rayleigh scattering and LDA. Although this is an idealization of a turbulent flow, many of the important features of turbulent flame propagation are exhibited [28,29].

The wake behind a cylinder for Reynolds numbers ($Re_D \equiv U D/\nu$) between 40 and 5000 exhibits a fairly regular pattern of alternately rotating vortices known as a Kármán vortex street. This phenomenon has been studied extensively by many investigators (see the review by Marris [30]). A result of the stability analysis of an ideal Kármán vortex street [see Ref. 31], which consists of two staggered infinite parallel rows of vortices whose strengths are equal but opposite in sense (see Fig. 1.1) is that the only arrangement which exhibits neutral stability is one in which $h/\ell = 0.281$. Fage and Johansen [32], Rosenhead and Schwabe [33], Kovasznay [34], and Roshko [35,36], measured the variation of the vortex shedding frequency with Reynolds number and provided considerable data on the dependence of the Strouhal number ($St = f D/U$) on the Reynolds number. Kovasznay [34] and Roshko [35] found that a stable, regular vortex street is obtained

only for Reynolds numbers between 40 and about 150. Various authors quote different values of the upper limit. This may be due to the fact, not generally realized, that for Reynolds numbers below a critical value the vortex street is not shed from the cylinder but develops from a laminar wake instability [30,34]. When the Reynolds number increases to some critical value, there is a transition and the vortices begin to be shed directly from the cylinder. In this transition regime vortex shedding becomes irregular but becomes regular again once beyond it until the wake becomes turbulent. Tritton [37] and Marris [30] suggest that the critical value of Reynolds number for this transition is about 90. During this study this transition was observed over a range of Reynolds numbers as low as 75. The data of Roshko [35] suggests that he may have observed this phenomenon at a Reynolds number of 150, although he attributed the transition to scatter and not to a fundamental change in the fluid dynamics.

The regularity of the vortex street permits the use of phase-locked signal averaging to produce details of the complete two-dimensional flow field as a function of time. Thus models for the wrinkling geometry may be compared to these results and appraised as to how well they predict the flame behavior for a relatively simple fluctuating flow field with essentially one frequency and length scale. A schematic of the problem studied is shown in Fig. 1.2. The fuel used was ethylene, C_2H_4, for all the cases studied. The conditions at which measurements were made are summarized in Table 1. Because of the irregular nature of the wake for $Re_D = 500$, ensemble averaging could

not be performed on the measurements for this condition. Nevertheless, statistical moments of density, such as the mean and the root-mean-square (RMS), as well as spectra and probability density functions (P.D.F.) were calculated for this condition as well as for the lower Reynolds number cases. Only mean, RMS, and ensemble averaged velocities were calculated from the LDA data.

In addition to the measurements and calculations mentioned, a comparison was made with the predictions of the Bray-Moss-Libby model [14,38,39] for turbulent flame propagation. Bray and Moss [39] derive transport equations for a Favre averaged reaction progress parameter, $\tilde{c}$ and find that all statistical properties depend on state variables only, and these state variables depend solely on $\tilde{c}$ and a heat release parameter, τ. Assuming fast chemistry, the intermediate states are neglected. The reaction progress parameter is defined by

$$\frac{\rho}{\rho_u} = (1 + \tau c)^{-1} \qquad (1.2)$$

where ρ_u is the unburned gas density and

$$\tau = \frac{\rho_u}{\rho_b} - 1 \qquad (1.3)$$

where ρ_b is the density of the burned gas. From eqns. (1.2) and (1.3) the time averaged density is

$$\frac{\overline{\rho}}{\rho_u} = (1 + \tau \tilde{c})^{-1} \ . \qquad (1.4)$$

The ratio of the Favre averaged to time averaged density is then

$$\frac{\tilde{\rho}}{\bar{\rho}} = \frac{\overline{\rho^2}}{\bar{\rho}^2} = 1 + \frac{\overline{\rho'^2}}{\bar{\rho}^2} = 1 + \frac{\tau^2 \tilde{c}(1 - \tilde{c})}{1 + \tau} , \qquad (1.5a)$$

and the density fluctuation intensity is

$$\frac{\overline{(\rho'^2)}^{1/2}}{\rho_u} = \frac{\bar{\rho}}{\rho_u} \tau \left[\frac{\tilde{c}(1 - \tilde{c})}{1 + \tau} \right]^{1/2} . \qquad (1.5b)$$

In the present experiment the quantities $\tilde{c}$, $\bar{\rho}$, $\tilde{\rho}$, $\overline{(\rho'^2)}^{1/2}$ and τ were calculated from the density measurements and compared with eqn. (1.5).

It should be noted that eqns. (1.2) - (1.5) impose no restriction on the turbulence. The only assumption involved is that the flame be treated as a flame sheet and intermediate states neglected. This assumption is more valied for wrinkled-laminar flames than for highly turbulent flames where there will be a thicker, more diffuse reaction zone. Since Libby and Bray [38] apply this model to highly turbulent flames, their predictions may be somewhat less accurate. However, since some of the flames considered here should be in the wrinkled-laminar-flame regime, the flame sheet approximation seems appropriate and eqns. (1.2) - (1.5) should be valid. In fact, Bray and Moss [39] comment that the approximation of negligible intermediate state "should be applicable to situations where wrinkled-laminar flame and related physical models are valid. On the other hand, if combustion

corresponds more closely to a distributed reaction model, [inter-mediates] will tend to be large, and the ... approximation will not be valid...".

CHAPTER 2: EXPERIMENTAL APPARATUS AND TECHNIQUE

Flow Apparatus

The test section consisted of an open jet wind tunnel. A coaxial jet was used in which the premixed gases of ehtylene and air flow through the inner jet. The diameter of the inner jet at the exit of the nozzle was 51 mm. An outer coaxial annular jet with an outside diameter of 102 mm was used to shield the inner flow from mixing with the stagnant surroundings. The flow velocity of the inner and outer jets were matched using the output of calibrated DISA hot-wire 55P11 and 55D01 anemometer system. The flow rates were also monitored using standard rotameters or a calibrated standard orifice meter. A 200 mm diameter stagnation chamber, 400 mm in length, was used to quiet the inner flow. There were three 16 mesh screens inside the chamber to subdue any turbulence in the flow. The flow for the outer jet was introduced into the outer nozzle via twelve 10 mm inlets to uniformly distribute the flow. In addition the flow passed through two 50 mesh screens, again to subdue any residual turbulence. The air was obtained from the high pressure house air supply. The ehtylene was supplied from standard bottles.

In order to further shield the test section from room currents and other disturbances a chimney about 150 mm high was used to partially enclose the test section. Access for collection optics was provided by making one of the walls a 3 mm thick pyrex window. Part of the chimney was left open in order to provide access for the laser beam. In preliminary investigations [40] it was found that if laser

access was provided by windows of standard quality, the light scattered by sub-surface micro-fractures would be collected and give a background signal which could be larger than the Rayleigh scattering signal. Under such conditions, Rayleigh scattering measurements would be quite difficult to make with any appreciable accuracy. The chimney and test section may be seen in the picture in Fig. 2.1.

Rayleigh Scattering

Rayleigh scattering is the scattering of photons by elastic collisions with particles which are small compared to the wavelength of light. The total Rayleigh scattering intensity is directly proportional to the number of scatterers and, when applied to gases, will be proportional to the number density.

The Rayleigh scattering intensity is given by [5],

$$I_R = C \, I_\ell \, N \sum_i X_i \, \sigma_{Ri} \qquad (2.1)$$

where C is a calibration constant for the optics, I_ℓ is the incident laser intensity, N is the total number density of the gas, X_i is the mole fraction of species i, and σ_{Ri} is the Rayleigh scattering cross-section of species i. σ_{Ri} is given by [41],

$$\sigma_{Ri} = \frac{4\pi^2}{\lambda^4} \left(\frac{n_i - 1}{n_0} \right)^2 \sin^2 \theta \qquad (2.2)$$

11

where the depolarization is assumed to be zero [42]. λ is the laser wavelength, n_i is the index of refraction of species i at S.T.P., n_0 is the Loschmidt number, and θ is the scattering angle as measured from the electromagnetic field vector.

It is convenient to non-dimensionalize the scattering intensity by the Rayleigh scattering at known conditions. Denoting this reference condition with subscript o the normalized intensity becomes

$$\frac{I_R}{I_{Ro}} = \frac{N}{N_0} \frac{\sum_i x_i \sigma_{Ri}}{(\sum_i x_i \sigma_{Ri})_o} \quad . \quad (2.3)$$

Substituting eqn. (2.2) into eqn. (2.3), one obtains

$$\frac{I_R}{I_{Ro}} = \frac{N}{N_0} \frac{\sum_i x_i (n_i-1)^2}{(\sum_i x_i (n_i-1)^2)_o} \quad . \quad (2.4)$$

Eqn. (2.4) shows that changes in the relative magnitude of Rayleigh scattering intensities are due to both changes in total number density and changes in chemical composition with accompanying changes in the index of refraction. With $N = \rho/W$, where ρ is the gas density and W is the mean molecular weight, eqn. (2.3) becomes

$$\frac{I_R}{I_{Ro}} = \frac{\rho}{\rho_0} \frac{W_0}{W} \frac{\sum_i X_i \sigma_{Ri}}{(\sum_i X_i \sigma_{Ri})_0} \quad . \tag{2.5}$$

To investigate to what degree Rayleigh scattering could be used as a direct measure of density Namer and Schefer [43] carried out calculations which indicated that for premixed C_2H_4-air flames at an equivalence ratio, $\phi = 0.5$, $I_R/I_{Ro} = 0.97 \rho/\rho_0$ in the post-flame zone, and for the worst case, within the flame where the concentrations of CO and H_2 peak, $I_R/I_{Ro} = 0.93 \rho/\rho_0$. Furthermore, the calculations show that the interpretation of the ratios of Rayleigh scattering as the ratio of densities will be more accurate than the interpretation as the inverse ratio of temperatures. Therefore, the Rayleigh scattering measurements made in C_2H_4-air flames, where $\phi = 0.5$ and 0.52, were essentially related directly to density and no corrections were made for changes in chemical composition through the flames. That is, within the accuracy of the measurements,

$$I_R/I_{Ro} \simeq \rho/\rho_0 \quad . \tag{2.6}$$

Figure 2.1 shows the test section and Rayleigh scattering optics. The optical system for Rayleigh scattering is shown in Fig. 2.2. A Spectra Physics 4-watt Argon ion laser is used as the light source for both the Rayleigh scattering and LDA measurements. The laser beam ($\lambda = 488$ nm) is focussed to 40 micron waist diameter by two lenses and the scattering is collected at 90° from the beam direction by an f/1.2,

55 mm focal length camera lens. The collection optics had an effective
f number of 2.8. The collected light passes through a 50 micron slit,
is collimated, and then filtered by a 1.0 nm band-pass filter centered
at 488 nm. The light is then refocused to the surface of a RCA 931A
type photomultiplier. The photomultiplier output is amplified by an
electrometer with a band-pass of approximately 1.8 KHz. The photo-
multiplier dark current was ~ 1% of the Rayleigh scattering signal of
air at 298°K.

Laser Doppler Anemometry

Laser Doppler anemometry (LDA) has become a widely used technique
for measuring velocity, particularly in reacting flows [6,8,19,44-46].
It is essentially an interferometric technique to determine the Doppler
shift in the frequency of light scattered by a moving particle [47].
The LDA system used is of the intersecting dual-beam type with real
fringes [48]. The laser beam is divided into two beams by an equal
path length beam splitter with a fixed beam separation of 50 mm. The
two beams are then focused by a 250 mm focal length lens to form the
probe volume. A standing fringe pattern is formed at the intersection
of the beams. When a particle crosses the fringes, it will scatter
light whose amplitude is modulated at the Doppler frequency, ν_D,
given by

$$\nu_D = 2 \, u \, \sin(\theta/2)/\lambda \tag{2.7}$$

where λ is the laser wavelength, θ is the angle formed by the inter-secting beams and u is the particle's velocity component perpendicular to the bisector of θ and in the plane of the two beams.

To employ LDA in gas flows it is usually necessary to seed the flow with scattering particles. These were generated by a cyclone-seeder using nominally 0.3 micron Al_2O_3 particles. Light scattering bursts from the particles were collected by a lens, filter and photo-multiplier assembly and the Doppler frequency was obtained using a TSI 1090 frequency tracker. A schematic of the LDA system is shown in Fig. 2.3. Only the streamwise velocity component, u, was measured.

It was found that the most effective way to obtain reasonable velocity data was by heavily seeding the flow so that the average data rate from the tracker was greater than 5000 /sec. The tracker output was sampled at a 1 KHz rate. Since the arrival times of the particles in the probe volume were Poisson-distributed, when the data rate was less than 5000/sec., there were significantly long periods of time in which no particles were recorded. This is illustrated in Fig. 2.4. However, for data rates greater than 5000/sec, the tracker output may then be treated as a continuous signal and individual particle arrival times did not have to be monitored. In addition, a 500 Hz low-pass filter was used at the output of the tracker. This cut-off frequency was about one order of magnitude greater than the frequencies of the velocity fluctuations of interest in the flow, which were of the order of the vortex shedding frequencies.

Vortex Generating Cylinder and Reference Hot Wire

Considerations of the properties of a Kármán vortex street, the laminar flame propagation speed, and stability and the physical dimensions of the experimental apparatus established constraints on the range of operating conditions. For instance, two flow velocities and two cylinders were used to generate the vortex street at different frequencies. The cylinder diameters were necessarily small (2.0 and 3.0 mm) to maintain the large length-diameter ratios (45 and 30 respectively) needed to obtain, essentially, a two-dimensional flow field. The flow velocities used were 55 and 250 cm/s. Thus, for $U = 55$ cm/s, the Reynolds numbers were 73 and 110 for the 2 and 3 mm rods respectively. For the flow velocity $U = 250$ cm/s the 3 mm rod was used to generate the vortex street. The Reynolds number for this condition was 500. In order to get stable flame propagation and avoid flashback or blowoff an equivalence ratio of 0.52 was chosen when $U = 55$ cm/s ($Re_D = 73$ and 110). The equivalence ratio was 0.5 when $U = 250$ cm/s ($Re_D = 500$). Furthermore, as illustrated in Fig. 1.2, the cylinder had to be placed far upstream of the flame in order to prevent the flame from attaching itself to the vortex generating cylinder. This precaution was quite important since the reference hot wire necessary for phase-locked measurements would be destroyed by the flame if flashback occurred. The flameholder was a 1.0 mm diameter rod located at the origin of the coordinate system used. Denoting the coordinates of the vortex generating cylinder location as (x_c, y_c), x_c was - 25.0 mm and y_c is tabulated in Table 1 for each case studied.

In order to make the phase-locked measurements a reference signal was needed in order to obtain the phase angle of the flow field at any instant of time. This reference signal was supplied by a hot-wire-anemometer whose location was fixed with respect to the vortex generating cylinder. Conventional hot-wire probes could not be used because conventional probe holders, being comparable in size to the vortex generating cylinder, would perturb the flame in a similar manner. A novel hot-wire probe was designed and constructed which incorporates the cylinder as both a vortex street generator and hot-wire probe holder. A schematic of the construction is shown in Fig. 2.5 and a top view of the test section and the vortex street generator are shown in Fig. 2.6. The vortex generating cylinders used were pyrex tubes. The wire sensor, 0.02 mm diameter gold plated tungsten, was spot welded to the tips of 0.5 mm diameter platinum wire supports 10 mm apart. The sensor position is fixed at 10 mm above the cylinder and offset to the side by about one cylinder radius where the fluctuating component of the signal from the sensor was a maximum.

As reported in the literature, it was found that the regularity of the vortex street was enhanced by reducing three-dimensional end effects. This was done by putting 2 cm square end plates, made of cardboard, on the cylinders to isolate the interaction between the cylinder and the edge of the jet. The end plates and their position can be seen in the picture of Fig. 2.6.

Computerized Data Acquisition

To facilitate the use of the diagnostic system a computerized data acquisition system based upon a Digital Equipment Corporation (DEC) PDP 11/10 was used. The computer system is operated under DEC RT-11 using an RK05 disk with 1.25 million (16 bit) words and two IBM 729 magnetic tape drives. The operating system was accessed by a Tektronix 4025 terminal with graphics display capable of plotting processed data and a high speed line printer was used for permanent page plots and data output listing.

The experimental apparatus was mounted on a three-axis traverse operated by separate stepping motors which were computer-controlled. Thus the flow field positions could be scanned automatically for Rayleigh scattering and LDA measurements. Profiles of velocity or density were obtained by scanning, under computer control, in the y-direction (see Fig. 1.2) for a particular x location. When the profile was completed the test section was moved to a new x location for the next profile. The distance, in x, between profiles to be used for phase-locked averaging was 2 mm and there were 18 profiles taken for each set of conditions. The profiles were started in the region of reactants. The spacing in the y-direction was 1.5 mm for the velocity measurements and data was taken at 20 locations in y. For making the density measurements an adjusting grid was used so that 1.5 mm steps were taken in the y-direction outside the flame and 0.5 mm steps inside the flame. To do this the mean signal level from 100 samples was calculated and compared with the mean at the previous location. If the

mean was less than 80% of the previous mean, the test section was backed up 1 mm and the spacing was 0.5 mm until outside the flame when the spacing was 1.5 mm again.

Measurements were obtained using an 8-channel, 12 bit A/D converter. Samples may be acquired at a constant sampling rate through clock control or individual samples may be initiated by a separate interrupt input by the user. In the latter mode, the time between samples may continuously be monitored by the clock. Raw data could be stored in disk memory files or on a 7-track magnetic tape for post-processing with either the PDP 11/10 or the Lawrence Berkeley Laboratory CDC 7600. Figure 2.7 illustrates the computer controlled data acquisition system for taking LDA measurements.

The hot-wire, described above, supplied the reference signal for the phase-locked averaging. The reference signal was sampled simultaneously along with the LDA tracker or, when making Rayleigh scattering density measurements, the electrometer output voltage, at a 1 KHz rate on two channels of the A/D converter and the data was stored in a data file. LDA measurements were made by taking 4070 samples at each location of a two-dimensional x-y grid. For comparison, LDA measurements of the wake with no combustion as well as the Rayleigh scattering measurements through the flame were made utilizing 2022 samples per channel per location.

When obtaining Rayleigh scattering data to be used to determine the power spectrum and the P.D.F., the reference hot-wire was not monitored. For this case the data rate was 1.0, or 2.0 KHz (see Table 1) as required by the vortex shedding frequency for each particular case. There were 5030 samples per location taken for these measurements.

CHAPTER 3: DATA REDUCTION TECHNIQUES

Ensemble Averaging Technique

The feature which made this study attractive is the regularity and the repetitive nature of the Kármán vortex street in the wake of a cylinder. Phase-locked or ensemble averaging is possible and highly resolved velocity and density fields can be determined as a function of time or phase. The ensemble average is obtained by averaging measurements at the same location and phase. Thus, for example, the velocity measurements are reduced from $u(x,y,t)$ to $\tilde{u}(x,y,\phi)$ and the desnity measurements are reduced from $\rho(x,y,t)$ to $\tilde{\rho}(x,y,\phi)$, where ϕ here is the phase angle of the flow field and $0 \leqslant \phi \leqslant 1.0$. (Note that here $\sim$ does not signify Favre averaging.)

The basis for ensemble averaging is the reference hot-wire signal which was used to establish the phase of the flow field. The method used to perform the ensemble averaging in this study is described below. Consider a function, $g(t)$, which may represent an oscillating velocity or density as a function of time at a given location, and which is sampled at discrete time intervals to generate a set of measurements $g(t_i)$. Further consider a reference function $R(t)$, where $R(t)$ is periodic with mean $\overline{R(t)} = 0$. There will be N roots or zero crossings t_n°, $n=1,\ldots, N$, which satisfy $R(t_n^\circ) = 0$ and $\frac{dR}{dt}(t_n^\circ) > 0$. Therefore, there are N-1 complete cycles whose periods are defined by $T_n = (t_{n+1}^\circ - t_n^\circ)$. The phase associated with a measurement $g(t_i)$ is defined by $\phi_i = (t_i - t_n^\circ)/T_n$, where $t_n^\circ < t_i < t_{n+1}^\circ$ and $0 < \phi_i < 1.0$. Thus $g(t_i)$ can be replaced by $g_n(\phi_i)$ which is the value of g at $\phi = \phi_i$

of cycle n. The ensemble average was thus calculated for 20 equally
spaced values of the phase angle Φ_j, $j = 1,20$, from

$$\tilde{g}(\Phi_j) = \frac{1}{M} \sum_{n=1}^{N-1} r \, g_n(\Phi_i) \tag{3.1}$$

where M is the number of measurements averaged and $r = 1$ if
$\Phi_j - 0.025 < \phi_i \leq \Phi_j + 0.025$ and $r = 0$ otherwise. The number of samples
averaged at each phase angle M, may be estimated by dividing the total
number of samples by 20. However, since the sampling rate is uncorre-
lated with the vortex shedding frequency, M can vary slightly for
different values of Φ and must be determined exactly for use in (3.1).

In order to insure that there were no significant irregularities
in the vortex street, data is only considered when the cycle period,
T_n is within 10% of the average period, TAU. In general, the amount
of data rejected by this criterion was small.

$\tilde{g}(\Phi_j)$ can be smoothed further by a truncated Fourier series
[cf. Ref 34] by defining

$$\tilde{g}(\Phi) = \sum_{m=o}^{2} \{A_m \cos(2\pi m\Phi) + B_m \sin(2\pi m\Phi)\} \tag{3.2a}$$

where

$$A_m = 2 \sum_{j=1}^{20} \tilde{g}(\Phi_j) \sin(2\pi m\Phi_j) \delta\Phi_j \tag{3.2b}$$

$$B_m = 2 \sum_{j=1}^{20} \tilde{g}(\Phi_j) \sin(2\pi m\Phi_j) \delta\Phi_j \tag{3.2c}$$

and

$$\delta\Phi_j = 0.05 \tag{3.2d}$$

With such an averaging technique at every point on a two-dimensional
x-y grid such quantities as $\hat{u}(x,y,\Phi)$ and $\hat{\rho}(x,y,\Phi)$ may be found. A
convenient way to present these are by plotting lines of constant $\hat{u}$ or
$\hat{\rho}$ for various values of Φ, thus reproducing a series of detailed
"snapshots" of the flow field.

Time Series Analysis

A time series analysis of the Rayleigh scattering data was performed
in which statistical moments, power spectra, and probability density
functions were calculated. Standard algorithms were used as discussed
in [49,50]. The mean and RMS densities were calculated from the data,
corrected for instrument noise as well as background signal as des-
cribed below in the section entitled Noise Removal. The power spectra
were calculated using a fast-Fourier transform routine from the
library of the Lawrence Berkeley Laboratory CDC 7600. These were cal-
culated from 4096 samples and yielded 2048 spectral points. To
increase accuracy the 2048 spectral points were grouped into 64
groups of 32 points each and an average was obtained for each group.
The resolution is thus decreased by a factor of 64 while the accuracy
increased by $\sqrt{32}$. The P.D.F. was obtained by forming a histogram from
the data. The histogram consisted of 60 equally spaced bins between
the minimum and the maximum of the data. The spectra and P.D.F. from
the Rayleigh scattering from cold reactants and hot products are shown
in Figs. 3.1 and 3.2 respectively. It should be noted that neither was
corrected for background or PMT noise, but were corrected for scattering

from occasional particles.

Noise Removal

There were various sources of noise in both LDA and Rayleigh scattering measurements which had to be removed. This noise is due to the statistical variations in photon arrival rates as well as general instrument noise in the PMT, electrometer, and LDA tracker.

For the velocity measurements the noise may be assumed to be uncorrelated with the vortex shedding frequency. Therefore, the mean and RMS velocities can be accurately determined directly from the ensemble averaged results. Therefore, no further analysis for the removal of noise was performed on the LDA velocity data.

In the case of Rayleigh scattering, the variance of the noise of the photomultiplier is proportional to the mean current [5]. Therefore at the beginning of each profile, photomultiplier fluctuations in the free stream outside the flame were recorded. Since no density fluctuations exist at this location, the signal's variance is due primarily to photomultiplier noise. Then at other locations this variance, adjusted for change in the mean current level of the photomultiplier, is subtracted from the total signal variance. For example, consider the total signal intensity, I_T, consisting of Rayleigh scattering, I_R, and photomultiplier noise, I_N. Then

$$I_T = I_R + I_N \ .$$

(3.3)

Since the average noise, $\overline{I_N}$, is zero,

$$\overline{I_T} = \overline{I_R} \quad . \tag{3.4}$$

From (3.3)

$$\overline{I_T^2} = \overline{I_R^2} + 2\overline{I_R I_N} + \overline{I_N^2} \tag{3.5}$$

and since I_R and I_N are uncorrelated, the quantity $\overline{I_R I_N} = 0$. By introducing the fluctuating component I' such that

$$I = \overline{I} + I'$$

eqns. (3.4) and (3.5) yield

$$\overline{I_T'^2} = \overline{I_R'^2} + \overline{I_N^2} \quad . \tag{3.6}$$

The P.D.F.'s of the Rayleigh scattering signal for (a) cold reactants and (b) hot products are shown in Figs. 3.2. For these conditions there are no density fluctuations. Since these P.D.F.'s are not corrected for PMT noise, the broadening is due solely to this noise, I_N. It can be seen that the broadening is greater for the cold reactants, where the total signal is larger, than for the hot products. From [5] $\overline{I_N^2}$ is proportional to $\overline{I_T}$, hence

$$\overline{I_N^2} = \overline{I_{N_0}^2}\left(\overline{I_T}/\overline{I_{T_0}}\right) \qquad (3.7)$$

The variance of the Rayleigh scattering signal from (3.6) and (3.7) is

$$\overline{I_R'^2} = \overline{I_T'^2} - \overline{I_{N_0}^2}\left(\overline{I_T}/\overline{I_{T_0}}\right) \qquad . \qquad (3.8)$$

In addition to the PMT noise the Rayleigh scattering signal may be contaminated by unrelated background light, the PMT dark current, and light scattered from occasional particles in the flow which is picked up by the collection optics. The background intensity plus the PMT dark current were removed by substracting the average signal when the collection optics was moved $\pm$ 0.6 mm in order to allow the slit to block the light scattered directly from the laser beam. This background level was $\leq$ 3% of the Rayleigh scattering intensity. The signal level rose by one or two orders of magnitude when a particle was present in the probe volume. During post-processing, if a sample was more than 3.5 standard deviations from the mean, the datum was assumed to be due to a particle and the value was reset to the value of the previous sample. If the value of the first sample was due to a particle, it was reset to the mean. The number of particles were $\leq$ 2% of the total number of samples and did not affect the mean, but would have significantly affected the RMS, P.D.F., and spectra, unless these were corrected for scattering from the particles.

CHAPTER 4:   RESULTS AND DISCUSSION OF VELOCITY MEASUREMENTS

The streamwise velocity component, u, was measured using LDA for three cases: a) in the wake of a 2.0 mm cylinder, b) through a flame in the wake of a 2.0 mm cylinder, and c) through a flame in the wake of a 3.0 mm cylinder. Presented here are the mean and standard deviation (RMS) of u along with contour plots of the smoothed ensemble averaged velocity field.

Mean and RMS

A typical velocity profile across the wake of a 2.0 mm cylinder is shown in Fig. 4.1. The velocity profile across the wake of a cylinder is characterized by the defect in the mean velocity which is associated with the drag on the cylinder. For example, in Fig. 4.1 the non-dimensionalized mean velocity, $\bar{u}/U \simeq 0.75$ at the center of the wake, which is located at $y = 12.5$ mm. The profile of the fluctuating intensity of velocity, $(\overline{u'^2})^{1/2}/U$, across a Kármán vortex street exhibits two peaks whose locations are associated with the centers of the two rows of vortices. In Fig. 4.1 these peaks are located at $y = 7.5$ and 17.5 mm. Therefore the lateral spacing of this vortex street, h, is 10 mm (see Fig. 1.1). The maxima in fluctuation intensity are essentially equal for the two rows and are about 0.07. This agrees quite well with measurements obtained by Refs. [34,35].

Mean and RMS velocity profiles across a flame in the wake of 2 and 3 mm cylinders are shown in Figs. 4.2(a) and (b) respectively.

Starting at $y = 30$ mm $\bar{u}/U \simeq 1.0$ and the velocity fluctuations are nearly negligible. At $y \simeq 25$ mm the mean velocity is decreasing and the fluctuations reach a local maximum which, from the above discussion of Fig. 4.1, indicates that the wake has been deflected about 7.5 mm to the right. Recall that for the cases represented in Figs. 4.1 and 4.2 the vortex generating cylinder is located at $y = 12.5$ mm. The deflection of the wake, and hence the flow upstream of the flame is due to the pressure drop across the flame which is necessary to accelerate the flow behind the flame. These data indicate that the pressure drop across the flame significantly affects the approach flow. Although the pressure drop across a flame is small compared to atmospheric pressure, it is large in comparison to the dynamic head of the approach flow. To estimate the pressure drop across a flame, consider a one-dimensional flame. From mass continuity

$$\rho_u \, u_u = \rho_b \, u_b = \dot{m} \tag{4.1}$$

and from conservation of momentum the pressure drop across the flame is

$$\Delta p \equiv p_u - p_b = \rho_b \, u_b^2 - \rho_u \, u_u^2 \quad . \tag{4.2}$$

With eqn. (4.1) this becomes

$$\frac{\Delta p}{\rho_u \, u_u^2} = \frac{\rho_u}{\rho_b} - 1 \quad . \tag{4.5}$$

The right-hand side of eqn. (4.3) is equal to τ from eqn. (1.3) and $\tau = 4$ for the conditions studied here. Since values for τ of 7 and 8 are common, it is clear that the pressure drop through a flame is not insignificant compared to the dynamic head. Comparison of the change in pressure across the flame with the static pressure is not appropriate except in order to justify neglecting variations of thermodynamic properties with pressure. Clearly the effect of combustion on the flow field upstream of the flame must be accounted for since this flow will in turn affect the combustion process. The present study along with [16-18] throw doubts on conclusions and models, such as the concept of flame-generated turbulence (see Refs. [1,15-18,38]), based on theories and data which do not take pressure variations into account. In contrast, the treatment and modeling of the flame proposed by Chorin [51] and used in [27], [28] and [52] does account for this interaction. In these studies the flame is modeled as a sheet which convects with and propagates into the flow. The effect of combustion on the flow field is modeled by representing the flame by a line source of specific volume. Thus the decrease in density, the acceleration of the flow, and the pressure field are correctly modeled.

At $y \simeq 12$ mm in Figs. 4.2 the velocity exhibits a sharp rise and the non-dimensional RMS velocity increases to ~ 0.15. This indicates the presence of a fluctuating flame at this location. Equation (4.1) indicates that as the density decreases through the flame the velocity must increase. The large value for the RMS velocity at the flame is due to an Eulerian effect when the flame fluctuates across the probe volume and should not be construed as flame-generated turbulence.

Behind the flame ($y \lesssim 7$ mm in Figs. 4.2) the velocity fluctuations become very small but the mean velocity continues to increase. This is because when the flow is accelerated across a flame, the acceleration is in the direction normal to the flame. For the type of flames studied here, this implies a significant acceleration inward in the cross-stream direction. If the x-axis ($y = 0$) may be considered to be an axis of symmetry across which no flow can pass, the cross-flow must be diverted parallel to the x-axis (in a fashion similar to stagnation flow) and a further acceleration behind the flame is observed.

A series of mean velocity profiles at various streamwise, x, locations across flames in the wake of a 2 and a 3 mm rod are shown in Figs. 4.3(a) and (b) respectively. The features discussed above are demonstrated in these figures. For example, the location of the velocity defect due to the wake is centered at $y \simeq 15$ mm for $x = 10$ mm and at $y \simeq 22$ mm for $x = 30$ mm. Furthermore, the flame location, associated with the large velocity gradients goes from $y \simeq 5$ mm at $x = 10$ mm to $y \simeq 22$ mm at $x = 40$ mm. The additional acceleration behind the flame due to the stagnation type flow is also observed. In addition, the linear behavior of $\bar{u}/U$ with x which is predicted by a simple stagnation flow solution is found, for example, at $y = 1.5$ mm.

An alternative representation of the mean velocity profiles can be obtained by plotting contours of constant mean velocity as a function of x and y. This is also usefull since the phase-locked results will be presented in this manner as well. Figures 4.4(a) and (b) show contour plots of the mean streamwise velocity component, in cm/s., for the flame in the wake of a 2 and a 3 mm rod respectively. The center

of the wake is indicated by the low velocity region. The flame loca-
tions or shape is not clearly defined in these pictures because the
manner in which the flow accelerates behind the flame does not lead to
a sharp interface between reactants and products. Rayleigh scattering
measurements will more accurately define the wrinkling of the flame.
However, the flame location is indicated by the region of largest flow
acceleration, therefore, the contours are densely concentrated at the
flame. Behind the flame the flow continues to accelerate. Because of
the range of velocities encountered, contour intervals were 2 cm/s
ahead of the flame and 5 cm/s behind the flame.

Phase-Locked Analysis

In order to determine what an ideal vortex street would look like
when represented by contours of the streamwise velocity, u, contours
were computed for the ideal vortex street in Fig. 4.5a and are shown in
Fig. 4.5b. It can be seen that each vortex is represented by a paired
structure consisting of a high and a low velocity center. This is
because the vortex retards the flow in the center of the street and
augments it on the outside. Figure 4.6 shows the wake of a 2 mm cylinder
at four phase angles, $\Phi \equiv T/TAU$. The vortex shedding frequency was
34 Hz and the convection velocity of the vortices was 50 cm/s. TAU, the
average period is the reciprocal of the vortex shedding frequency.

In Fig. 4.6 the paired high-low structures are more irregular than
was found for the ideal vortex street in Fig. 4.5. Although the data
is smoothed in time by the ensemble averaging, a suitable smoothing

function in space that was general enough to handle an arbitrary effect due to a flame at arbitrary location was not found. Since such smoothing in space was not feasible for measurements across the flame, it was deemed inappropriate to further smooth the data for the wake of cylinder in the absence of a flame. Therefore, some irregularities in the "snapshots" of the velocity field are to be expected. Nevertheless, the phase-locked averaging technique is capable of reproducing the two-dimensional flow field as a function of the phase angle.

A parameter in the calculations in [27,52] is the strength of the vortices in the vortex street. From the contours of u the vortex strength, κ, produced in the experiment can be estimated for each case studied here. For a potential vortex the strength, κ, is defined as

$$\kappa = r \, u_\theta(r) \tag{4.6}$$

where r is the distance from the center of the vortex and $u_\theta(r)$ is the velocity induced by the vortex at r. If κ is constant $u_\theta(r \to 0) \to \infty$. Therefore, a real vortex must depart from the ideal behavior for $r < R_{crit}$. It is reasonable to expect that the ideal and non-ideal regions should match at $r = R_{crit}$. Here it is assumed that the high and low centers of a vortex occur at $r = R_{crit}$ and (4.6) is applicable there. From symmetry considerations R_{crit} is one half the distance between the high and low centers and the convection velocity, which must be subtracted from u to obtain u_θ, is the average of the velocities of the high and low centers in the vortex. From this model the values of $\kappa \simeq 2.5$ and 6.0 are obtained for the vortices from the 2 and 3 mm cylinder, respectively. These values are comparable to those used in [52]. In

light of this it is interesting to note that the flame oscillations

calculated in [52] were not as large as those measured here. This point

will be discussed in detail later in Chapter 5.

A series of "snapshots" of the flow field are shown in Figs. 4.7

and 4.8 for the flame in the wake of a 2.0 and 3.0 mm rod respectively.

These consist of constant velocity contours at a given phase angle as

obtained from the phase-locked averaging. In these figures the vorti-

ces are less clearly defined than in Figs. 4.5 and 4.6. This is pri-

marily a consequence of the fact that the acceleration of the flow at the

flame precludes local highs and lows. The identity of the vortices on

the side of the wake furthest from the flame is maintained to a greater

degree than for the vortices partly in the flame. In addition, there

is no evidence of the vortices behind the flame. Again, this is due,

in part, to the continued acceleration of the flow behind the flame

which precludes the local highs and lows observed in Figs. 4.5 and 4.6

as well as ahead of the flame in Figs. 4.7 and 4.8. Nevertheless,

since the difference in velocity between the high and low centers in an

eddy is 20-25 cm/s. for the two cases, one might expect to see some

indication of the vortices beyond the flame since the contour level is

only 5 cm/s. in this region. However, no evidence of the vortices was

observed beyond the flame and it appears that the vortices were

"consumed" by the flame. This is due to a combination of dilatation or

stretching of the vortices in the direction normal to the flame, as

well as the increase in the dissipation rate due to increased viscocity

behind the flame. The kinematic viscosity, ν, varies approximately

as $T^{3/2}$ in the temperature range of the experiment. Since the temper-

ature increases by a factor of 5 across the flame, the rate of dissipation

is 11 time greater behind the flame than ahead of it.

To estimate the effect of increased dissipation consider a vortex
of strength $\kappa = 5$ cm^2/s. and $R_{crit} = 0.3$. Hence from (4.6) the velo-
city induced by a vortex at $r = R_{crit}$ is $u_\theta(R_{crit}) \simeq 15$ cm/s.
Schlichting [53] the solution for the decay of a vortex through the
action of viscosity is

$$u_\theta(r,t) = \frac{\kappa}{r} \{1 - \exp(-r^2/4\nu t)\} \quad . \tag{4.7}$$

Neglecting the effect of dilatation consider the time it takes for the
velocity induced by the vortex at $r = 0.3$ cm to become small enough so
that the vortex cannot be observed in the contour plots. The contour
intervals behind the flame are 5 cm/s. and are ~ 0.1 cm apart. There-
fore, for the vortex to be observable it would have to induce a velo-
city $u_\theta \simeq 10$ cm/s. Using a value for ν of 1.68 cm^2/s. (4.6) gives
$t \simeq 0.014$ sec. If the characteristic convection velocity is 75 cm/s.,
the vortex will have travelled about 1 cm before becoming undetectable.
The velocity contours at about 1 cm beyond the flame are still affected
by the unsready behavior of the flame. By the time a vortex is suffi-
ciently far from the flame so that the velocities induced by the
vortex can be discriminated from the velocity fluctuations induced by
the flame, the dissipation has reduced the velocities induced by the
vortex to the point where they cannot be observed. As mentioned earlier,

dilatation will further reduce the gradients in velocity induced by a vortex.

CHAPTER 5:   RESULTS AND DISCUSSION OF DENSITY MEASUREMENTS

Time Series Analysis

A typical density profile through a flame obtained, as described
in Chapter 3, from Rayleigh scattering measurement is shown in Fig. 5.1.
All densities are normalized by the density of the reactants at room
temperature. Recall that the flameholder is located at $y = 0$. The
flame is identified by the gradient in mean density seen here in the
region $20 \lesssim y \lesssim 30$. Note that the ratio of the burned gas density to
the unburned gas density is 0.2 and, therefore, from eqn. (1.3) $\tau = 4$.
This is also the region where large density fluctuations are found as
a consequence of the flame fluctuations. It can be noted that the peak
in density fluctuations occurs at approximately the location where the
mean density is one half the unburned gas density. Figures 5.2 and 5.3
illustrate the evolution of the mean and RMS density profiles, for the
various conditions studied, as a function of streamwise location, x.
Thickening of the flame with increasing x is seen in both the mean and
RMS profiles. The flame thickness for the undisturbed flames (no
vortex street) is ~ 1.0 mm as determined from Rayleigh scattering
profiles. The formation of what could be termed the flame brush is
apparent from these profiles. Furthermore, the mean position of the
flame is altered when the vortex street is introduced. This may
be seen in Figures 5.4 and 5.5. For the two cases of lower
vortex shedding Reynolds number ($Re_D = 73$ and 110) the mean flame posi-
tion is observed to move upstream from its undisturbed location. For
$Re_D = 500$ the effect of the vortex street on the flame is much more
pronounced. The flame brush becomes much thicker and is approximately

20 mm thick. Surprisingly the mean flame position is downstream of the undisturbed flame. This may be due to a change in the nature and character of the flow in the vicinity of the flameholder when the vortex street is introduced. However, this cannot be determined from the available data.

A summary of the Reynolds number, Strouhal number, and the vortex shedding frequency for the conditions investigated is given in Table 2. Power spectra of density fluctuations are shown in Fig. 5.6. Table 2 and Fig. 5.6 show that for all three cases the peak in the spectrum of density fluctuations correlates fairly well with the vortex shedding frequency. The discrepancies are not unreasonable considering the scatter in the data of [35]. Additional power may also be seen at the double frequency.

As discussed in Chapter 1, the Favre averaged reaction progress parameter, $\tilde{c}$, may be determined at each location from the mean density, $\bar{\rho}$. The Favre averaged density can also be computed from the measurements of density. These can be compared with the values of $\tilde{\rho}/\bar{\rho}$ and $(\overline{\rho'^2})^{1/2}/\rho_u$ calculated from eqn. (1.5). The theoretical evolution of the density fluctuation with $\tilde{c}$ were computed from eqn. (1.5b) for $\tau = 4.0$. The experimental results are plotted in Figs. 5.7 and 5.8. For all conditions the theory overpredicts the fluctuations in density. The maximum fluctuation intensity is overestimated by $\sim 10\%$ for the lower Reynolds number cases. This overprediction is not too severe and the fluctuations in the flame can be modeled with reasonable accuracy by the wrinkled-laminar flame model and by neglecting intermediate states. However, for $Re_D = 500$, when the flame brush becomes 20 mm

thick, the flame consists of a distributed reaction zone and interme-
diate states cannot be neglected. If they are neglected as in (1.5b),
the maximum density fluctuation intensities are overpredicted by $\sim 30\%$.
The effect of neglecting intermediates on the prediction of the Favre
averaged density, $\tilde{\rho}$, can be seen in Fig. 5.9. For example, eqn. (1.5a)
overpredicts $\tilde{\rho}/\bar{\rho}$ by $\sim 10\text{-}20\%$ at $\tilde{c} = 0.5$ for the conditions of this
experiment. Recall that

$$\frac{\tilde{\rho}}{\bar{\rho}} = 1 + \frac{\overline{\rho'^2}}{\bar{\rho}^2} \tag{1.5a}$$

so that $(\tilde{\rho}/\bar{\rho}) - 1$ also represents the square of the fluctuation inten-
sity normalized by the square of local mean. Again the theoretical
predictions of the Bray-Moss-Libby (B-M-L) model are larger than the
measured values of $\tilde{\rho}/\bar{\rho}$. This indicates that the form of eqns. (1.5a)
and (1.5b) will be altered by including intermediates in the analysis
following the B-M-L model. For example, one might hope that an effec-
tive heat release parameter, τ, could be found to correlate the data
in Figs. 5.7-5.9. However, this was not possible and an analysis based
on more realistic probability density functions is required.

To aid in the search for a more realistic P.D.F., it is worthwhile
to analyse the measured P.D.F.'s to determine their evolution through
the flame and the implication of their behavior in regards the B-M-L
model. It is helpful at this time to review certain aspects of the
B-M-L model. The Favre-averaged reaction progess parameter, $\tilde{c}$, may
still be obtained from eqn. (1.4), i.e.:

$$\tilde{\rho}/\bar{\rho}_u = (1 + \tau\tilde{c})^{-1} \quad . \tag{1.4}$$

The average of a quantity q may be obtained from

$$\overline{q} = \int_0^1 q \; P(\vec{r},c)dc \qquad (5.1)$$

where now

$$P(\vec{r},c) = \alpha(\vec{r})\delta(c)+\beta(\vec{r})\delta(c-1)+[\eta(c)-\eta(c-1)]\gamma(\vec{r})f(c) \; . \qquad (5.2)$$

The functions $\delta(c)$ and $\eta(c)$ are the Dirac delta and Heaviside functions, respectively. The coefficients $\alpha(\vec{r})$, $\beta(\vec{r})$ and $\gamma(\vec{r})$ represent the reactant, product, and intermediate probabilities respectively and $f(c)$ is a continuous function of product mass fraction through the flame. Then it follows that

$$\int_0^1 f(c)dc = 1 \qquad (5.3)$$

and

$$\alpha(\vec{r}) + \beta(\vec{r}) + \gamma(\vec{r}) = 1 \; . \qquad (5.4)$$

The above development is from Bray and Moss [39]. Since $\alpha(\vec{r})$, $\beta(\vec{r})$ and $\gamma(\vec{r})$ are not generally known, the integral in eqn. (5.1) becomes difficult. It is convenient to use $\tilde{c}$ as the independent variable and present the data accordingly, so that the spatial dependence of α, β, and γ are replaced by a dependence on $\tilde{c}$. It remains for this dependence to be determined. This is easily done by analyzing the P.D.F. of density at various locations in the flame and calculating $\tilde{c}$ from eqn. (1.4) for those locations. To illustrate, a P.D.F. is shown in Fig. 5.10. The probability of reactants, α, is determined by comparing with the P.D.F. for 100% reactants (see Fig. 3.2). A similar comparison with the P.D.F.

for 100% products yields the value of β. γ is then obtained from eqn. (5.4). The evolution of the P.D.F. with $\tilde{c}$ for the conditions summarized in Table 2, are shown in Figs. 5.11 to 5.13. Although not apparent (due to scaling restrictions) there are values of $\tilde{c}$ for which the probability of intermediate states is significant. This can best be seen in Figs. 5.14a, b, and c, where the values of α, β, and γ are plotted as a function of $\tilde{c}$ for Re_D = 73, 110, and 500, respectively. As can be seen from Figs. 5.14a and b, the value of γ can get as high as 0.4 or 0.5 in the flames for Re_D = 73 and 110. This means that at some locations in the flame the probability of encountering inter-mediate states can be 40 or 50%. Recall that these are the conditions most likely to correspond to a wrinkled-laminar flame and hence the flame sheet approximation is best applied here. The data shown in Fig. 5.7 for these cases indicated that the flame sheet approximation is a fairly good assumption to make for the purpose of predicting den-sity fluctuation intensities. An upper bound on expected fluctuations which is not too far from the actual fluctuation level can be obtained. However, for the case of a distributed reaction zone which corresponds to Re_D = 500, γ can reach 0.8 and the probability of encountering inter-mediates is as high as 80%, more than both products and reactants. The flame sheet model here is a poor predictor of statistical properties in the flame, which consists of a distributed reaction zone. This conclu-sion is in complete agreement with the expectation of Bray and Moss [39] as quoted earlier. It is curious that subsequently Bray and Libby [38] state that "in situations of practical interest ... the premixed turbulent flame will consist of 'packets' of unburned and fully-burned

gas, separated by narrow reaction zones, and the probability of reaction, γ, will be small compared to unity." This seems to be contrary to the observations in this investigation. It was found here that for the more highly turbulent flame γ is not negligible but may be greater than either α or β.

Phase-Locked Analysis

The application of the ensemble averaging technique described in Chapter 3 has enabled the reconstruction of the density field from a series of point measurements. The most important information to be obtained from this analysis is an understanding of the geometry of the wrinkling of a flame insofar as it is useful to the modeler. In the previous section it was shown that the wrinkled-laminar flame model and the flame sheet approximation may be appropriate for the cases of low vortex-generator Reynolds number, Re_D = 73 and 110. Therefore, it appears reasonable that the flame for these conditions may be treated as a flame sheet which is located at the position where the density is one half the unburned gas density. The effect of the eddies is to wrinkle this flame sheet. The wrinkling of this flame sheet can be seen in Figs. 5.15 a and b for vortex-generator Reynolds numbers of 73 and 110 respectively. The formation of a flame brush resulting from the fluctuations of the flame is readily apparent. A comparison of the two figures shows that the wrinkling is more severe with vortex generator Reynolds number Re_D = 110. For both Reynolds numbers a portion of the flame becomes normal or nearly normal to the streamwise direction, x.

The flame brush is comparatively thin in this region. This is attri-
buted to the interaction in this region with the center of the Kármán
vortex street where the mean velocity and the velocity fluctuations
are lowest. Recall from Table 1 that the location of the cylinder
which was used to generate the Kármán vortex street is $(x_c, y_c) = (-25, 12.5)$.
As shown by the velocity data the flow field upstream of the flame and
hence the vortex street, has been deflected. Where the center of the
vortex street passes through the flame corresponds to the region of the
flame where it becomes nearly normal to the streamwise direction, x.

A qualitative comparison between the data reported here and the
calculations in [52] can be made. Although the problem addressed in
[52] is similar to the one studied experimentally here, there are dif-
ferences in details which make direct quantitative comparisons diffi-
cult. For example, the calculations in [52] are for an enclosed or
ducted flame whereas the measurements made here were for an unconfined
flame. In addition, the vortex shedding frequency in [52] was 50 Hz
as opposed to ~ 25-30 Hz found in this experiment. The vortices in
[52] were not allowed to be altered by the flame but were found to be
"consumed" in the present study. Nevertheless, the flow velocities, U,
the vortex street separation, the strength of the vortices, and the
laminar flame speed used in the calculation in [52] were similar to the
experimental values. Finally, the value of the Markstein parameter, μ,
for different flames is not well documented and the choice is rather
arbitrary. However, [21-23] suggest that $\mu = 1$ is a reasonable value
for most flames and that was the value used in [52] to calculate the
flames in Fig. 5.16 which shows the flame at five different phase

angles. By comparing Figs. 5.15 with 5.16 the models used in [52] may be evaluated. First it is apparent that the measured and calculated flames do not resemble each other in the vicinity of the flameholder (located at the origin). This suggests that a better model for the behavior of the flame in the vicinity of the flameholder is needed, perhaps by an adjustment of the flame speed or the density ratio across the flame. This is reasonable since flame stabilization is, at least partly, accomplished by heat transfer to the stabilizer or flameholder.

A more important discrepancy between the measured and calculated results is that the numerical method employed in [27] and [52] does not allow the flame to be double-valued in the cross-stream coordinate, y. From Fig. 5.15 it is clear that the measured flames can become double-valued in y. Therefore, it is suggested that a more general description of the flame be adopted. For example, numerical instabilities which might occur when the flame tries to become multi-valued would be avoided by representing the flame surface with a function of both x and y. As a consequence of the simplified representation of the flame, a flame brush as thick as observed in Fig. 5.15 will not be obtained.

Overall, however, the data presented here indicates that the techniques described in [27,28,51,52] show promise of being capable of predicting turbulent flame behavior correctly.

CHAPTER 6: SUMMARY AND CONCLUSIONS

Rayleigh scattering and LDA have been used to make non-intrusive space and time resolved density and velocity measurements in a flame interacting with a Kármán vortex street. The vortex shedding Reynolds numbers were 73, 110, and 500. Phase-locked measurements of velocity and density were only made for Re_D = 73 and 110. The velocity measurements show that the flow is deflected upstream of the flame due to the pressure drop across the flame. This pressure change is significant in comparison to the dynamic pressure of the flow and cannot be neglected except in order to neglect variations of thermodynamic properties with pressure. In addition, there is evidence that the vortex street does not persist beyond the flame. It is indicated that the eddies in the vortex street are "consumed" in the flame by a combination of dilatation and increased rate of dissipation, which is 11 times greater behind the flame than ahead of it for τ = 4.

Spectral analysis of the Rayleigh scattering density measurements confirm that the dominant flame fluctuations occur at the vortex shedding frequency and its harmonics. The statistical properties of the density fluctuations were compared with the Bray-Moss-Libby model. For all cases the B-M-L model overpredicted density fluctuation intensities. The worst case was for the vortex shedding Re_D = 500 where the maximum was overpredicted by about 30%. In this case, the flame consisted of a distributed reaction zone and not what could be described as a wrinkled-laminar flame or a flame sheet. The overprediction of density fluctuation intensities was not too severe for Re_D = 73 or 110 where a wrinkled-laminar flame model and the flame sheet approximation

may be more valid. In the comparison between the measured and predicted values of the ratio of the Favre-averaged density to the mean density, $\tilde{\rho}/\bar{\rho}$ the maximum deviation was about 10-20%. Probability density functions of density were computed. From these the probabilities of products, reactants, and intermediates were determined. The probability of intermediates in the flame were found to be significant for all the cases studied. The maximum probability of intermediate states was ~ 40% for Re_D = 73 and 110 while for Re_D = 500 the probability was found to be as high as 80%. It is clear that the flame sheet approximation used in the B-M-L model which neglects intermediate states, is not satisfactory and more realistic P.D.F.'s are required. More experimental data are required on the evolution of the P.D.F. for flames for different turbulent flows, in order to construct an appropriate model for flames in which significant intermediates are present.

Comparison of the phase-locked ensemble averaging of the time varying flame location with the calculations carried out in [52] show reasonable qualitative agreement. Suggestions for improving assumptions and the choice of parameters have been made. These include the use of a more general representation of the flame position. In addition, the flame behavior near the flameholder must be more accurately modeled. Finally, a better representation of the vortices is required if their "consumption" by the flame is to be predicted. Nevertheless, some qualitative agreement was found and the effect of the pressure drop across the flame was accurately predicted.

ACKNOWLEDGEMENTS

REFERENCES

1. B. Karlovitz, "Selected Combust. Probs." Butterworths, London, 1954, 248-274.

2. A. C. Scurlock and J. H. Grover, "Selected Combustion Problems," Butterworth, London, 1954, 215-247.

3. F. A. Williams, "Combustion Theory," Addison-Wesley, Redding, Mass., 1965.

4. G. E. Andrews, B. Bradley and S. B. Lwakabamba, Combustion and Flame, v. 24, 1975, 285-304.

5. F. Robben, LBL-3294, Lawrence Berkeley Laboratory Report, 1975.

6. F. Durst, A. Melling and J. H. Whitelaw, Principles and Practice of Laser Doppler Anemometry, Academic Press, New York, 1976.

7. R. W. Schefer and F. Robben, LBL-9684, Lawrence Berkeley Laboratory Report, 1979, also to appear in Combustion and Flame.

8. R. K. Cheng, R. G. Bill, Jr. and F. Robben, to appear in 18th Symposium (Int.) on Combustion.

9. G. Z. Damkohler, Elektrochon, v. 46, 1940, 601; English translation, NACA Tech. Memo, no. 1112, 1947.

10. F. A. Williams, Combustion and Flame, v. 26, 1976, 269-270.

11. D. B. Spalding, Combustion and Flame, v. 1, no. 3, 1957, 287-295.

12. B. Karlovitz, D. B.Denniston and F. E. Wells, J.Chem. Phys., v. 19, no. 5, 1951, 541-547.

13. A. C. Scurlock and J. H. Grover, 4th Symposium (Int.) on Combustion, 1953, 645-658.

14. K.N.C. Bray and P. A. Libby, Phys. Fluids, v. 19, no. 11, 1976, 1687-1701.

15. I. Gökalp, _Acta Astronautica_, _v. 6_, 1979, 847-870.

16. J. L. Richmond, J. M. Singer, E. B. Cook, J. R. Oxendine, J. Grumer and D. S. Burgess, _Sixth Symp. (Int.) on Combustion_, 1957, 303-310.

17. J. K. Richmond, J. Grumer and D. S. Burgess, _Seventh Symp. (Int.) on Combustion_, 1960, 615-620.

18. K. O. Smith and F. C. Gouldin, _Paper No. 77-183_, presented at AIAA 15th Aerospace Sciences Meeting, Los Angeles, California, 1977.

19. R. G. Bill, Jr., I. Namer, L. Talbot, R. K. Cheng and F. Robben, "Flame Propagation in Grid-Induced Turbulence," submitted for publication to _Combustion and Flame_, 1980.

20. P. Clavin and F. A. Williams, _J. Fluid Mech._, _v. 90_, no. 3, 1979, 589-604.

21. G. H. Markstein, _J. Aero. Sci._, _v. 18_, 1951, 199-209.

22. R. E. Peterson and H. W. Emmons, _Phys. of Fluids_, _v. 4_, no. 4, 1961, 456-464.

23. G. H. Markstein, ed., "Nonsteady Flame Propagation," MacMillan Co., New York, 1964.

24. A. H. Lefebvre and R. Reid, _Combustion and Flame_, _v. 10_, no. 4, 1966, 355-366.

25. D. R. Ballal and A. H. Lefebvre, _Acta Astronautica_, _v. 1_, 1974, 471-483.

26. L. D. Landau and E. M. Lifshitz, "Fluid Mechanics," Addison-Wesley, Reading, Mass., 1959, 474-498.

27. I. Karasalo, A. J. Chorin, I. Namer, F. Robben, L. Talbot, "Numerical Simulation of the Interaction of a Flame with a Kármán Vortex Street," _LBL-10679_, Lawrence Berkeley Laboratory Report, 1980.

28. A. F. Ghoniem, A. J. Chorin and A. K. Oppenheim, "Numerical Modelling of Turbulent Combustion in Premixed Gases," submitted for publication to J. Fluid Mech, 1980.

29. A. R. Granji and R. F. Sawyer, AIAA J., v. 18, no. 7, 1980, 817-824.

30. A. W. Marris, J. Basic Engineering, v. 36, 1964, 185-196.

31. H. Lamb, "Hydrodynamics," Dover, 1945, 224-229.

32. A. Fage and F. C. Johansen, Proc. Roy. Soc. A, 1927, 1116.

33. L. Rosenhead and M. Schwabe, Proc. Roy. Soc. A, v. 129, 1930.

34. L.S.G. Kovasznay, Proc. Roy. Soc. London A, v. 198, 1949, 174-190.

35. A. Roshko, NACA TN 2913, 1953.

36. A. Roshko, NACA TN 3169, 1954.

37. D. J. Tritton, J. Fluid Mech., v. 6, 1959, 547-567.

38. P. A. Libby and K.N.C. Bray, AIAAJ, v.15, no. 18, 1977, 1186-1193.

39. K.N.C. Bray and J. B. Moss, Acta Astro., v. 4, 1977, 291-319.

40. I. Namer, Y. Agrawal, R. K. Cheng, F. Robben, R. W. Schefer and L. Talbot, UCB Report FM-77-3, 1977.

41. F. A. Jenkins and H. E. White, "Fundamentals of Optics," 2nd ed., McGraw-Hill Book Co., New York, 1950, 453-461.

42. C. M. Penney, J.O.S.A., v. 59, 1969, 34-42.

43. I. Namer and R. W. Schefer, "Interpretation of Rayleigh Scattering in Premixed Flames," submitted for publication in Combustion and Flame, 1980.

44. M.J.R. Schwar and F. J. Weinberg, Combustion and Flame, v. 13, 1969, 335-374.

45. F. Durst, A. Melling, J. H. Whitelaw, Combustion and Flame, v. 18, 1972, 197-201.

46. S. A. Self and J. H. Whitelaw, Comb. Sci. and Tech., v. 13, 1976, 171-198.

47. Y. Yeh and H. Z. Cummings, Appl. Phys. Letters, v. 4, 1964, 176-178.

48. M. J. Rudd, J. of Phys. E, v. 2, 1969, 55-58.

49. J. S. Bendat, and A. C. Piersol, "Measurement and Analysis of Random Data," Wiley, New York, 1971, 286-343.

50. J. W. Colley and J. W. Tukey, Math. of Computation, v. 19, no. 90, 1965, 297-301.

51. A. J. Chorin, "Flame Advection and Propagation Algorithms," to be published in J. Comp. Phys., 1980.

52. I. Karasalo and I. Namer, "Numerical Study of a Flame in a Kármán Vortex Street," to be submitted for publication, 1980.

53. H. Schlichting, "Boundary-Layer Theory," 6th ed., McGraw-Hill Book Co., New York, N.Y., 1968.

TABLE 1

U (cm/s.)	φ	D (mm)	y_c (mm)	Data rate (KHz)	Rayleigh Scattering					LDA		
					Mean	RMS	Spectra	PDF	Ensemble	Mean	RMS	Ensemble
55	0.0	2.0	12.5	1.0	No	No	No	No	No	Yes	Yes	Yes
55	0.52	-	-	1.0	Yes	Yes	Yes	Yes	No	No	No	No
55	0.52	2.0	12.5	1.0	Yes	Yes	Yes	Yes	Yes	Yes	Yes	Yes
55	0.52	3.0	12.5	1.0	Yes	Yes	Yes	Yes	Yes	Yes	Yes	Yes
250	0.5	-	-	2.0	Yes	Yes	Yes	Yes	No	No	No	No
250	0.5	3.0	10.0	2.0	Yes	Yes	Yes	Yes	No	No	No	No
500	0.7	-	-	4.0	Yes	Yes	Yes	Yes	No	No	No	No
500	0.7	3.0	10.0	4.0	Yes	Yes	Yes	Yes	No	No	No	No

TABLE 2

U (cm/s)	D (mm)	Re_D	S_t	f_t (Hz)	f_s (Hz)	f (Hz)
55.0	2.0	73	0.143	39	23 ± 4	30 ± 2
55.0	3.0	110	0.171	31	23 ± 4	24 ± 2
250.0	3.0	500	0.205	171	171 ± 8	-

U = Flow velocity

D = Diameter of vortex generating cylinder

$Re_D \equiv UD/\nu$ = Reynolds number of vortex generating cylinder based on the viscosity of the reactants at room temperature

$S_t \equiv$ Strouhal number from the correlation in [35]

$f_t \equiv S_t U/D$ = Vortex shedding frequency based on S_t

f_s = Vortex shedding frequency from spectrum of Rayleigh scattering

f = Vortex shedding frequency from the reference hot-wire

LIST OF FIGURES

Figure 1.1

XBL 805-9543

Figure 1.2
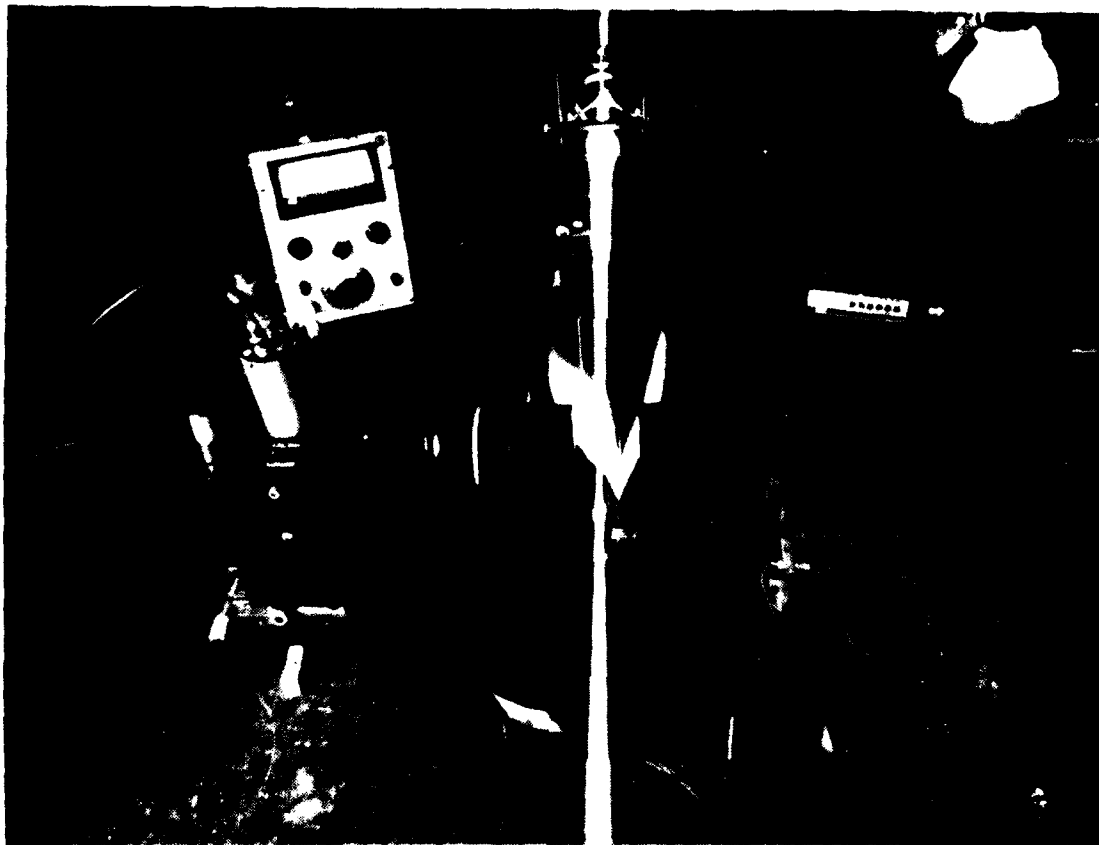
Figure 2.1
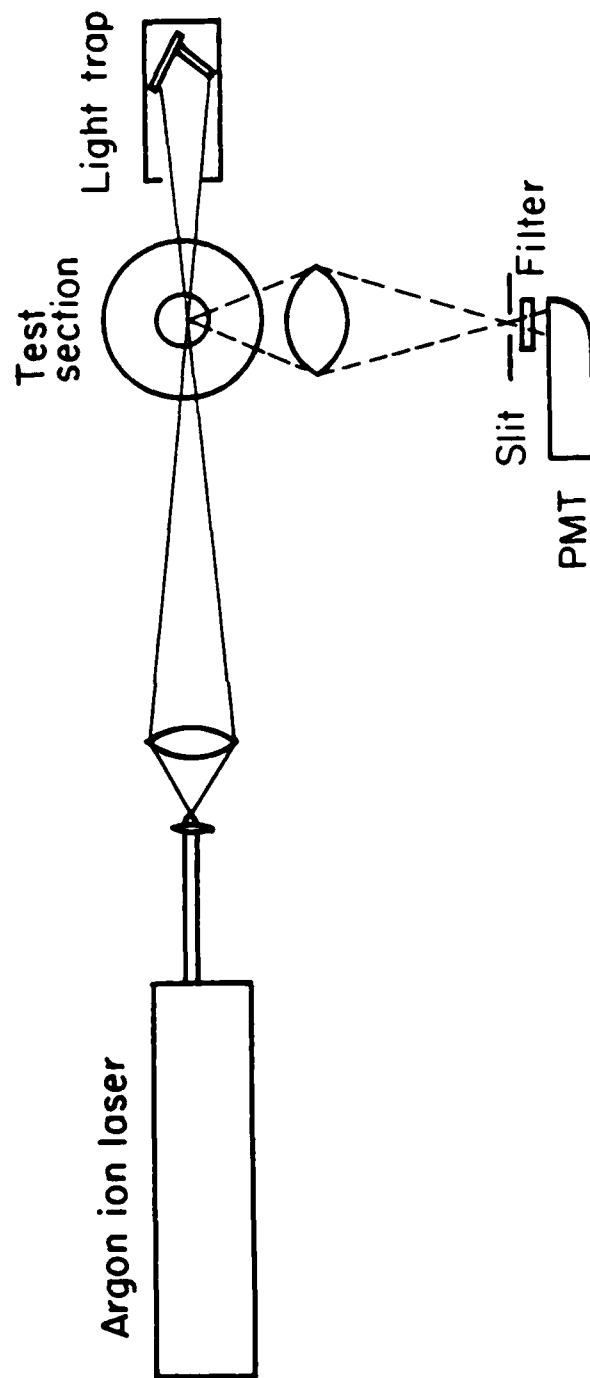
OPTICS FOR RAYLEIGH SCATTERING

XBL803-3178

Figure 2.2

Light trap

Test section

Beam splitter

Argon ion laser

LDV Detector

Pinhole

Filter

Photomultiplier
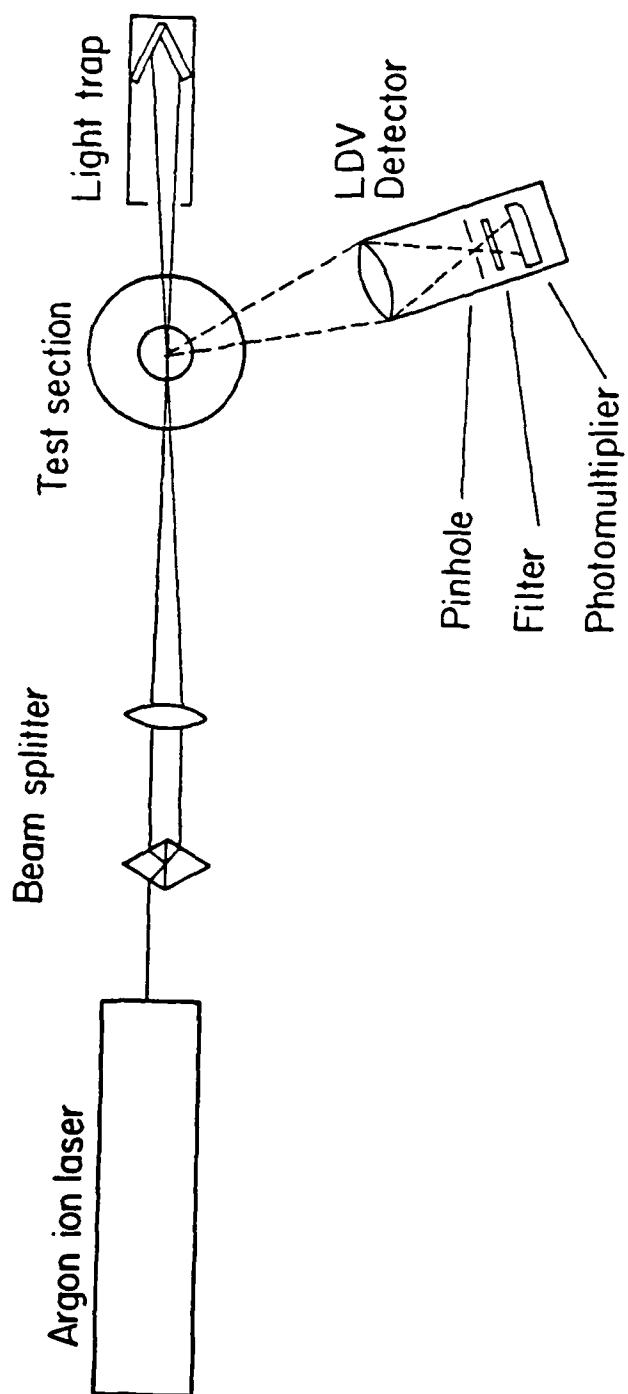
XBL 804-4130
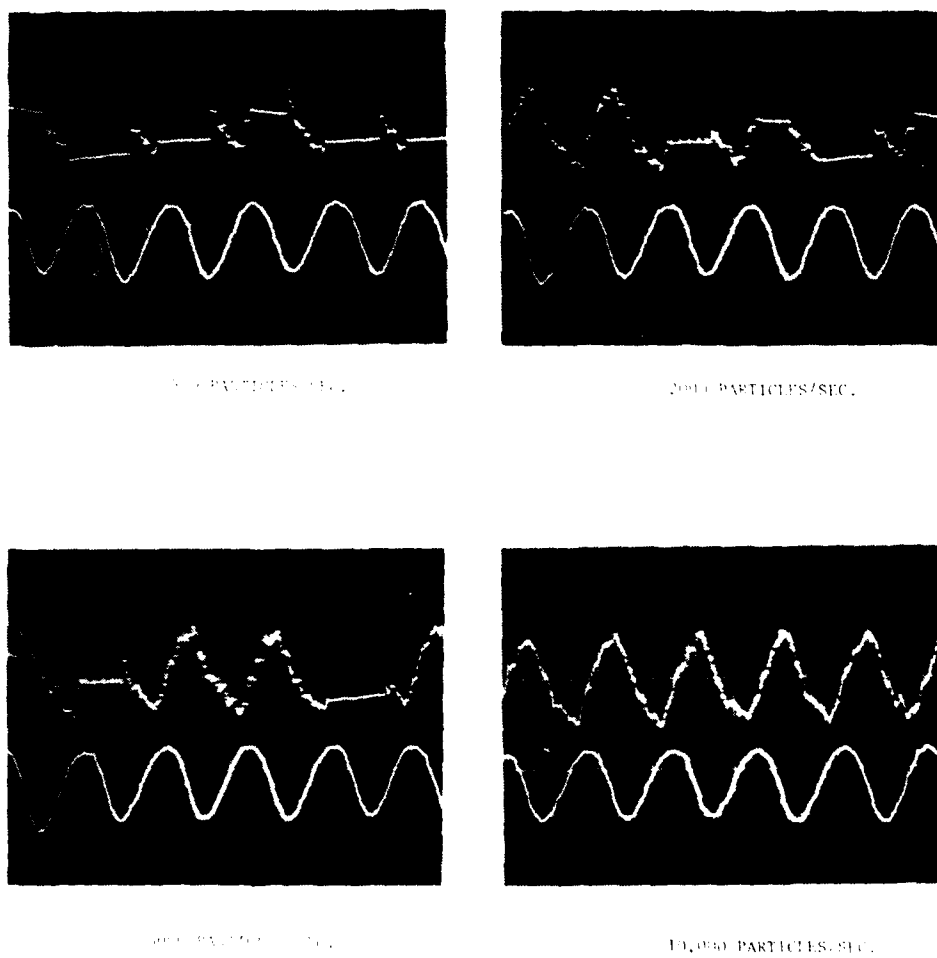
Figure 2.3

COMPARISON OF LDV OUTPUT (UPPER TRACE) WITH HOT WIRE (LOWER TRACE)
AT VARIOUS PARTICLE RATES, IN THE CORE OF A JET.
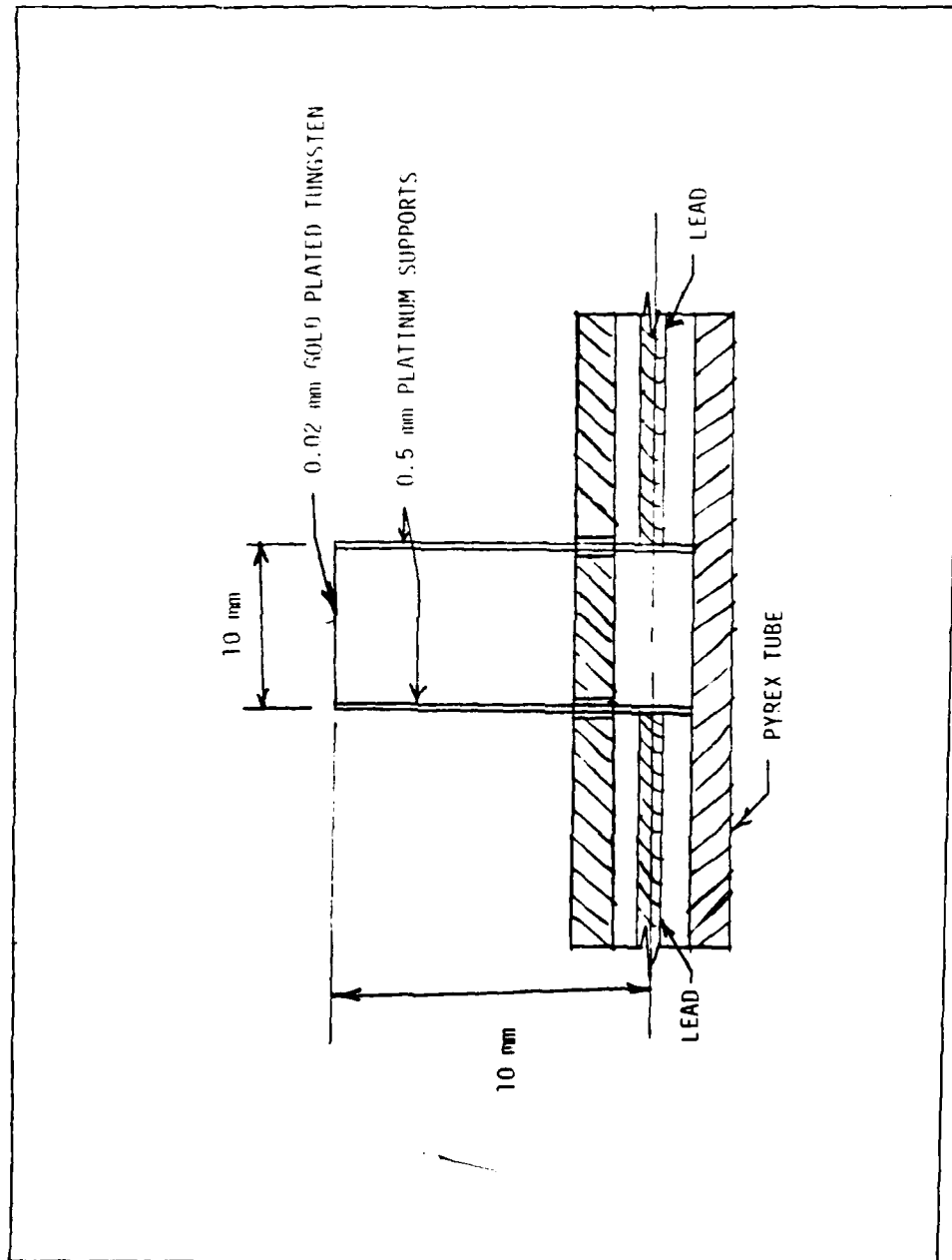
Figure 2.4

Figure 2.5

XBL 805-9544
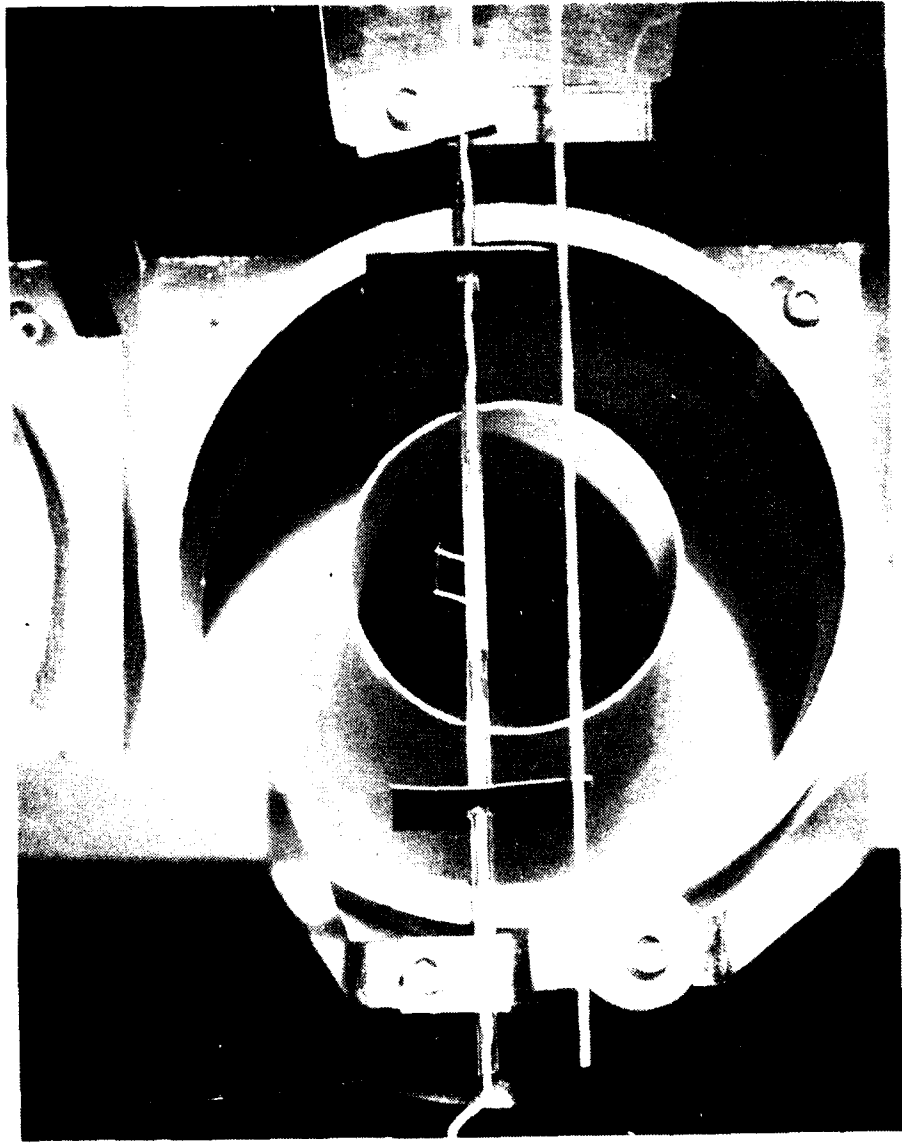
Figure 2.6
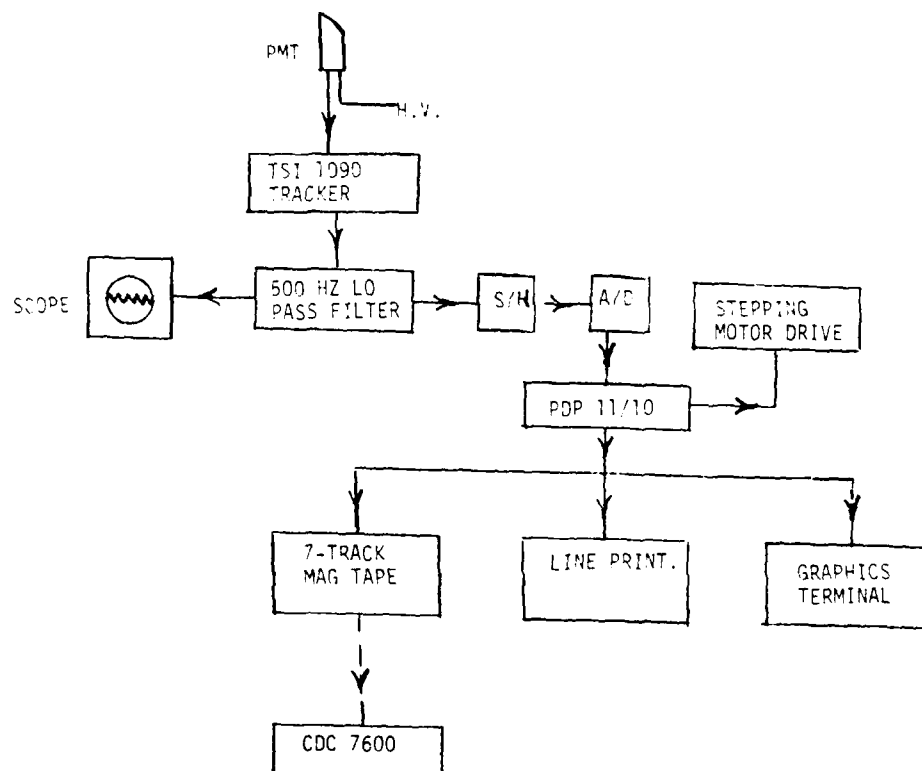
SCHEMATIC OF LDV DATA ACQUISITION SYSTEM

XBL 808-11111

Figure 2.7
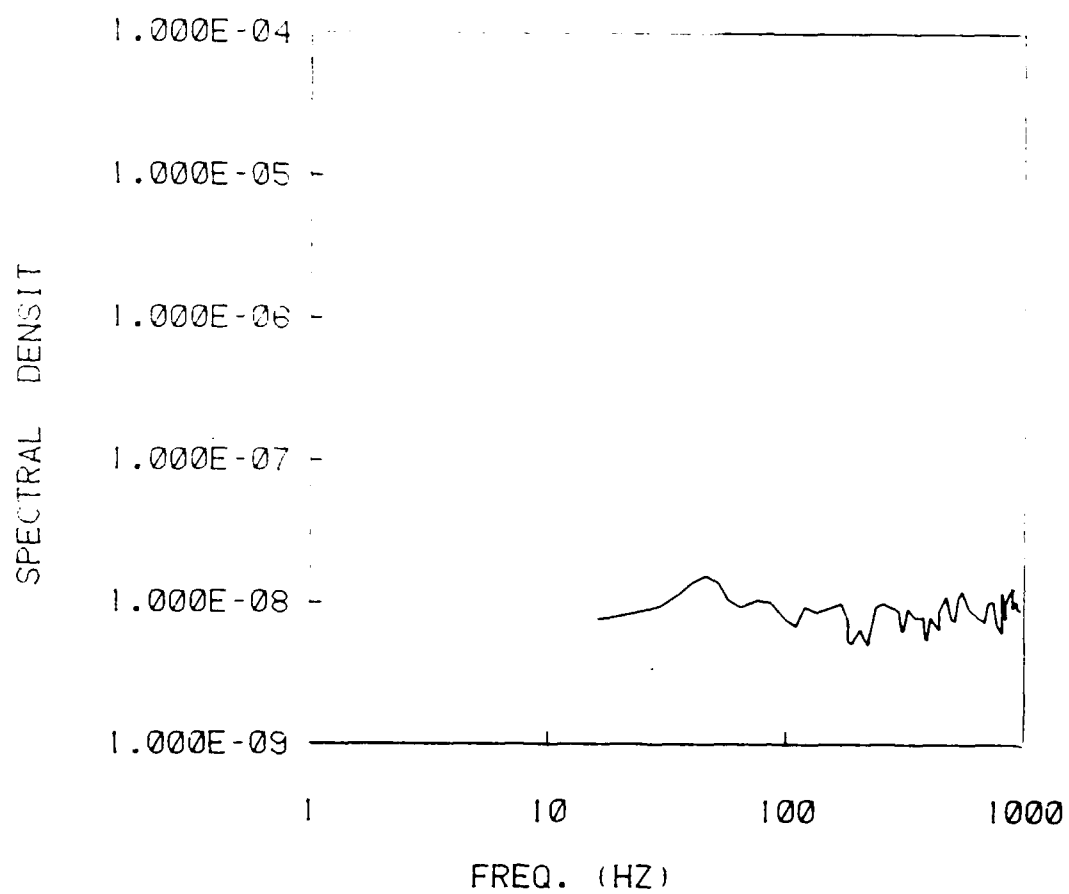
Figure 3.1a

XBL 808-10840
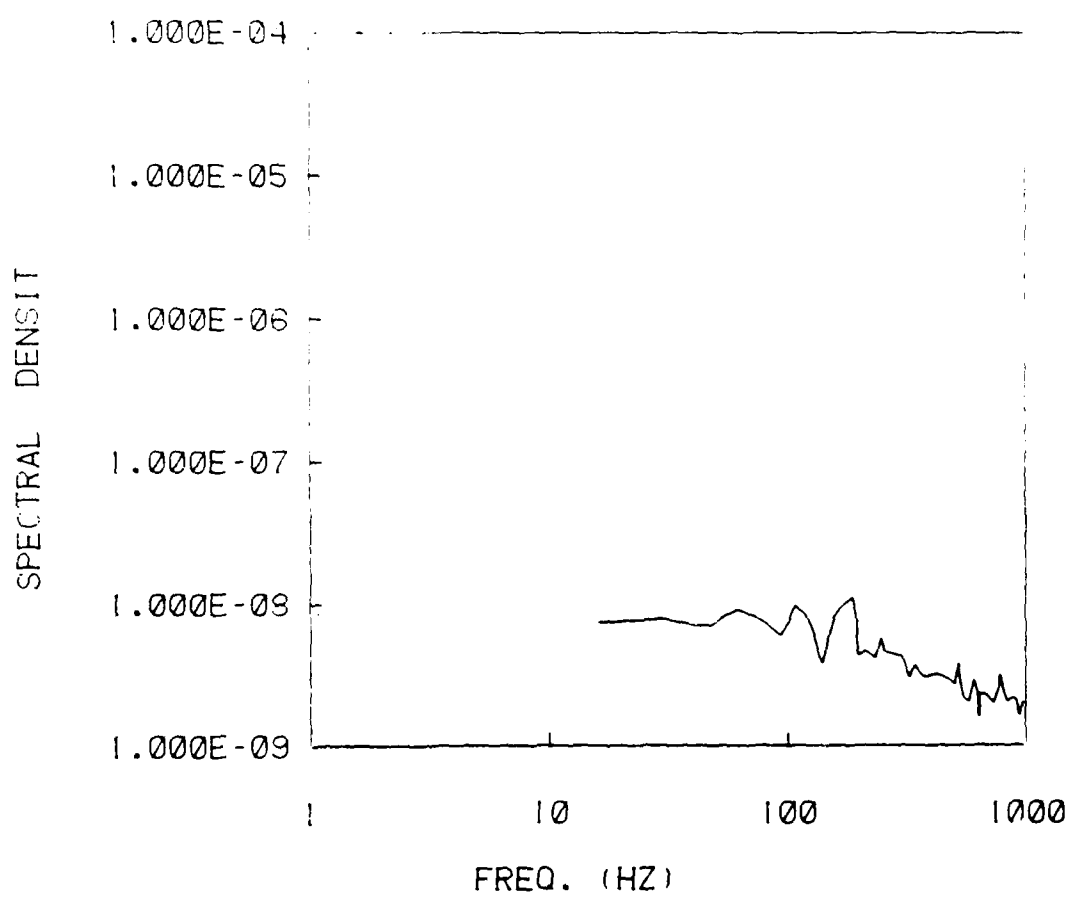
Figure 3.1b

XBL 808-10844

XBL 808-10837
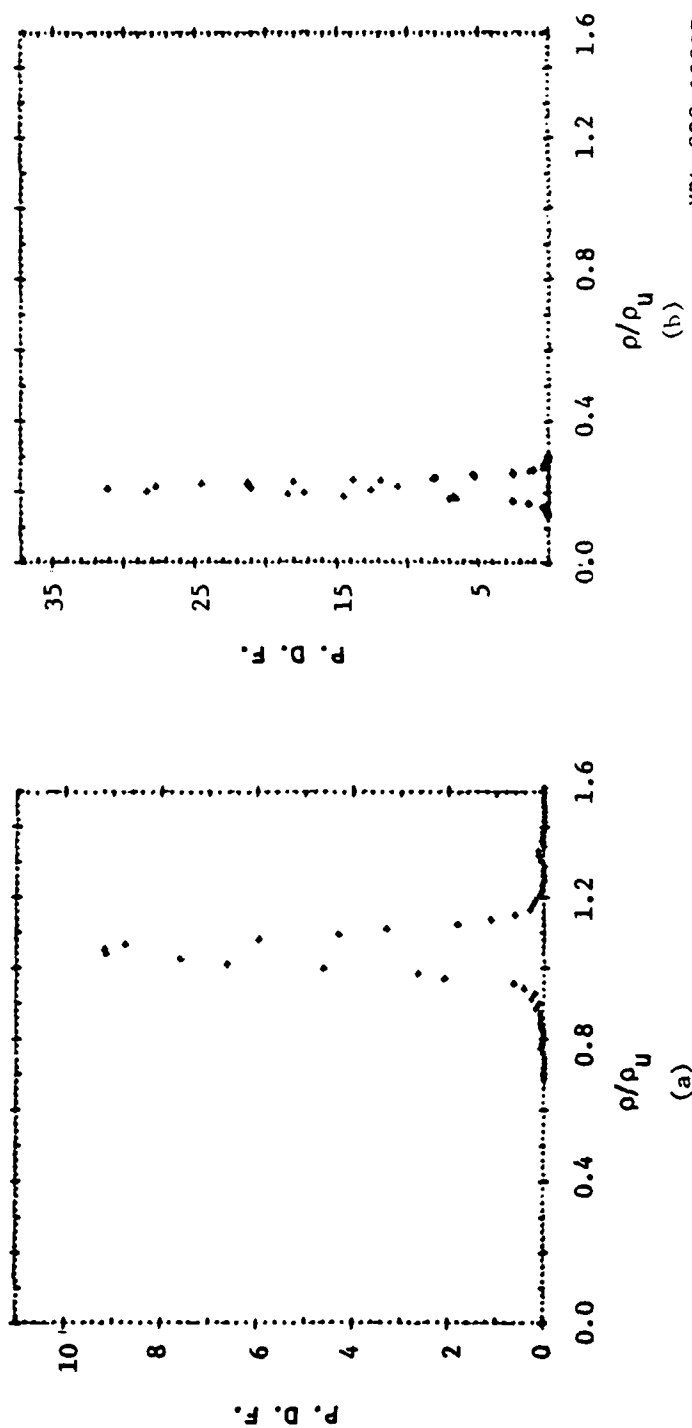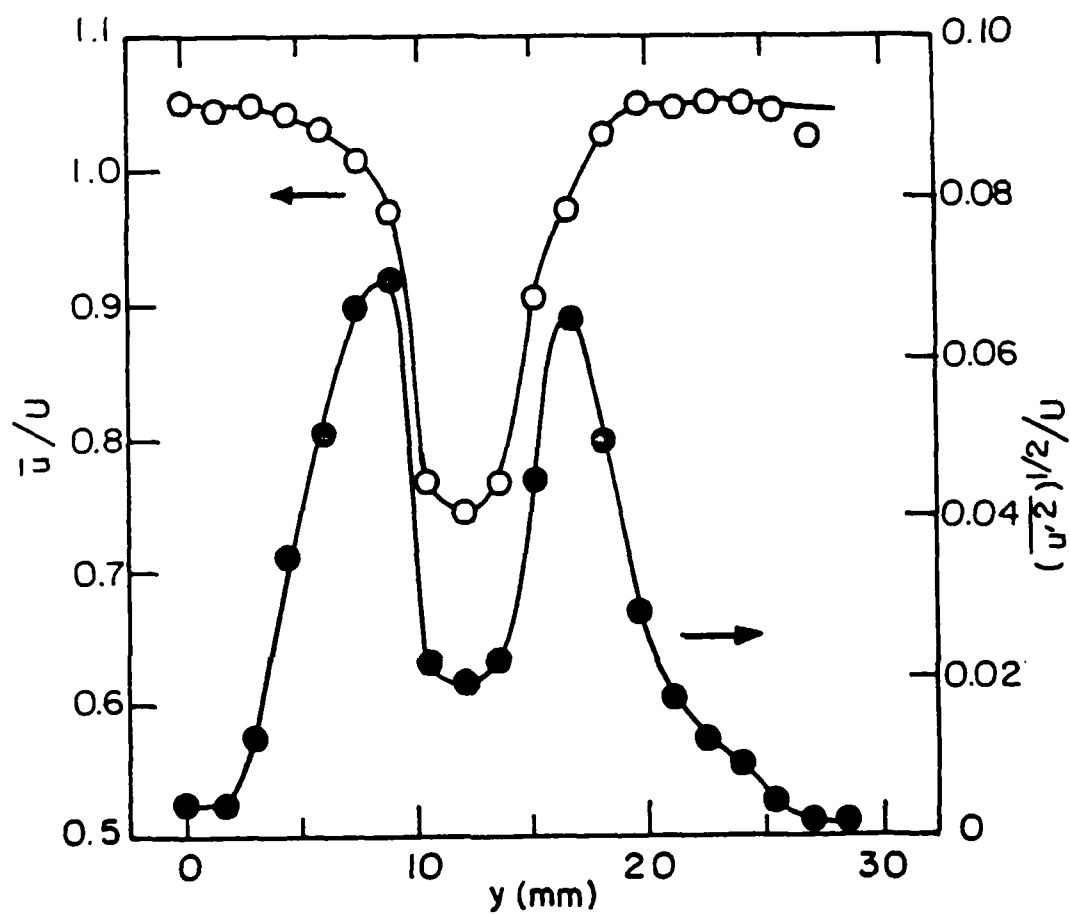
Figure 3.2

XBL 808-5623

Figure 4.1
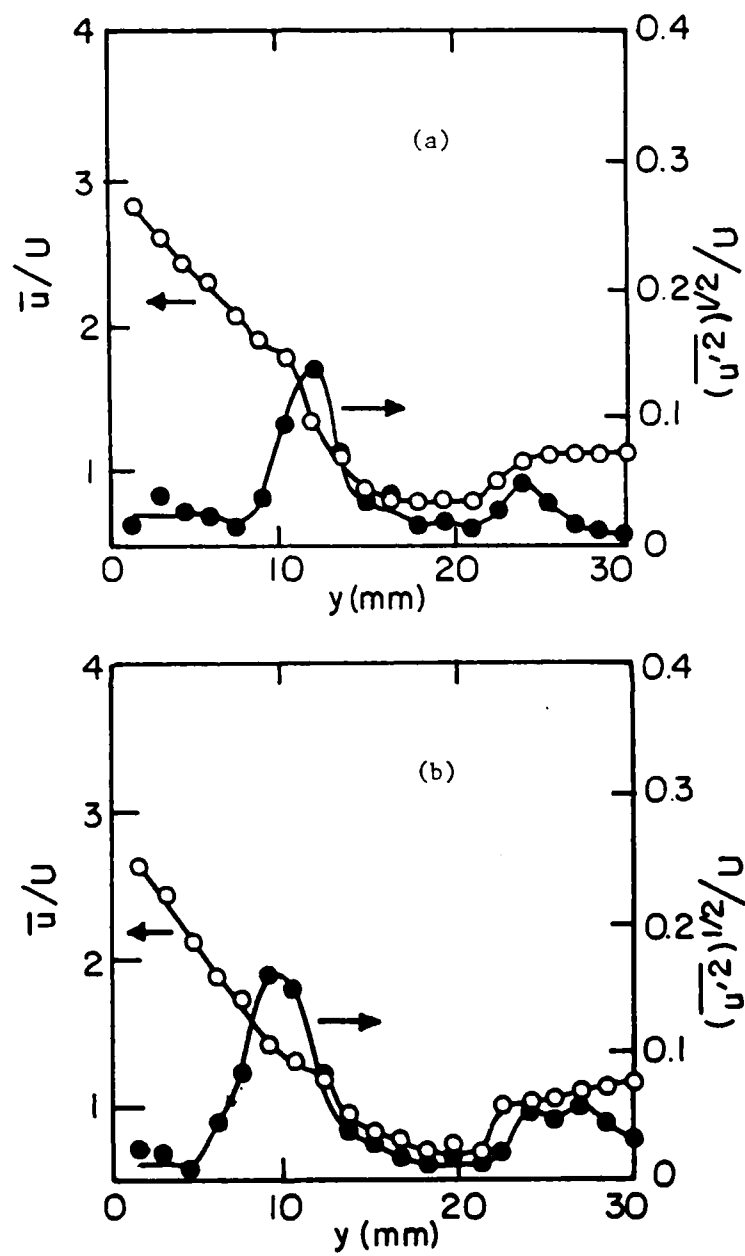
XBL 808-5624

Figure 4.2
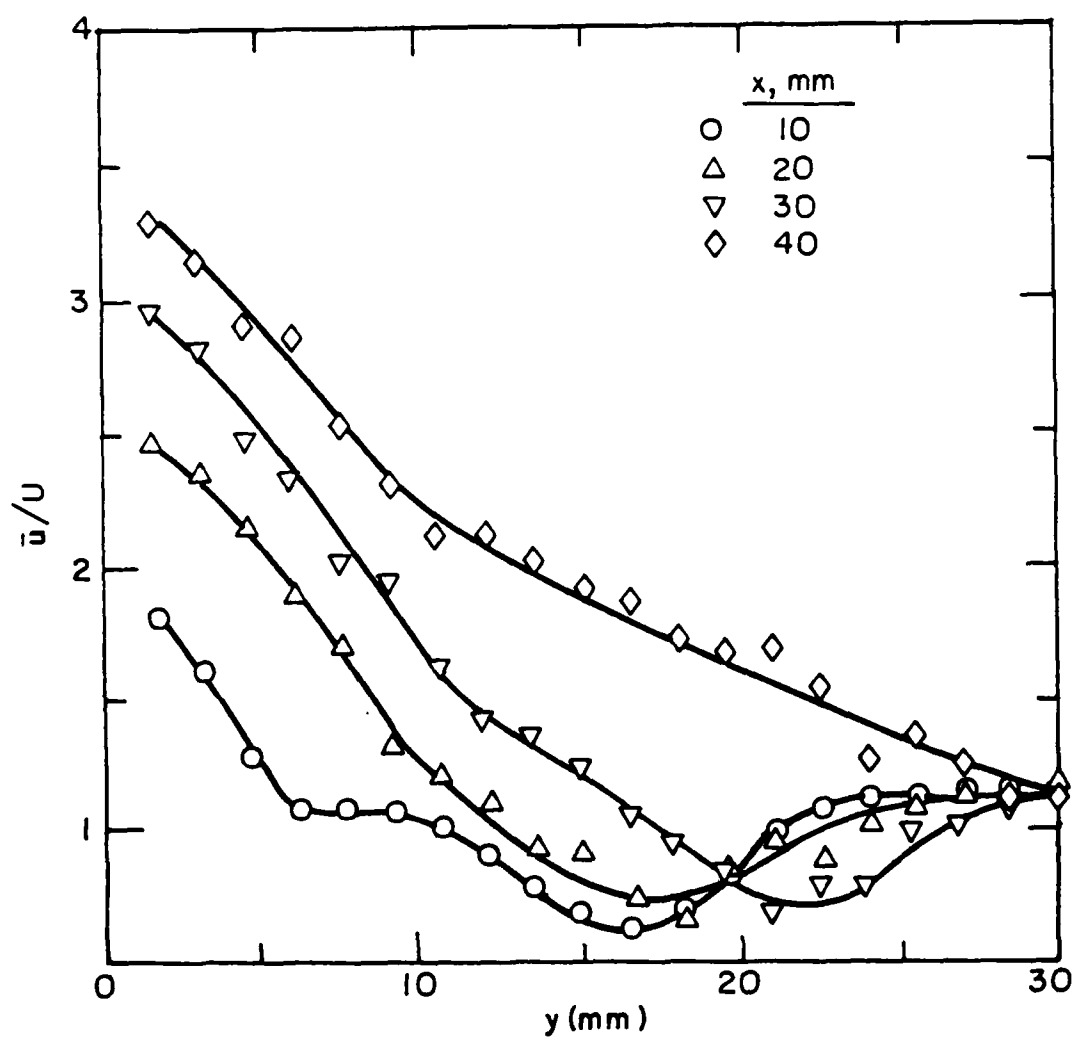
XBL 808-5626

Figure 4.3a
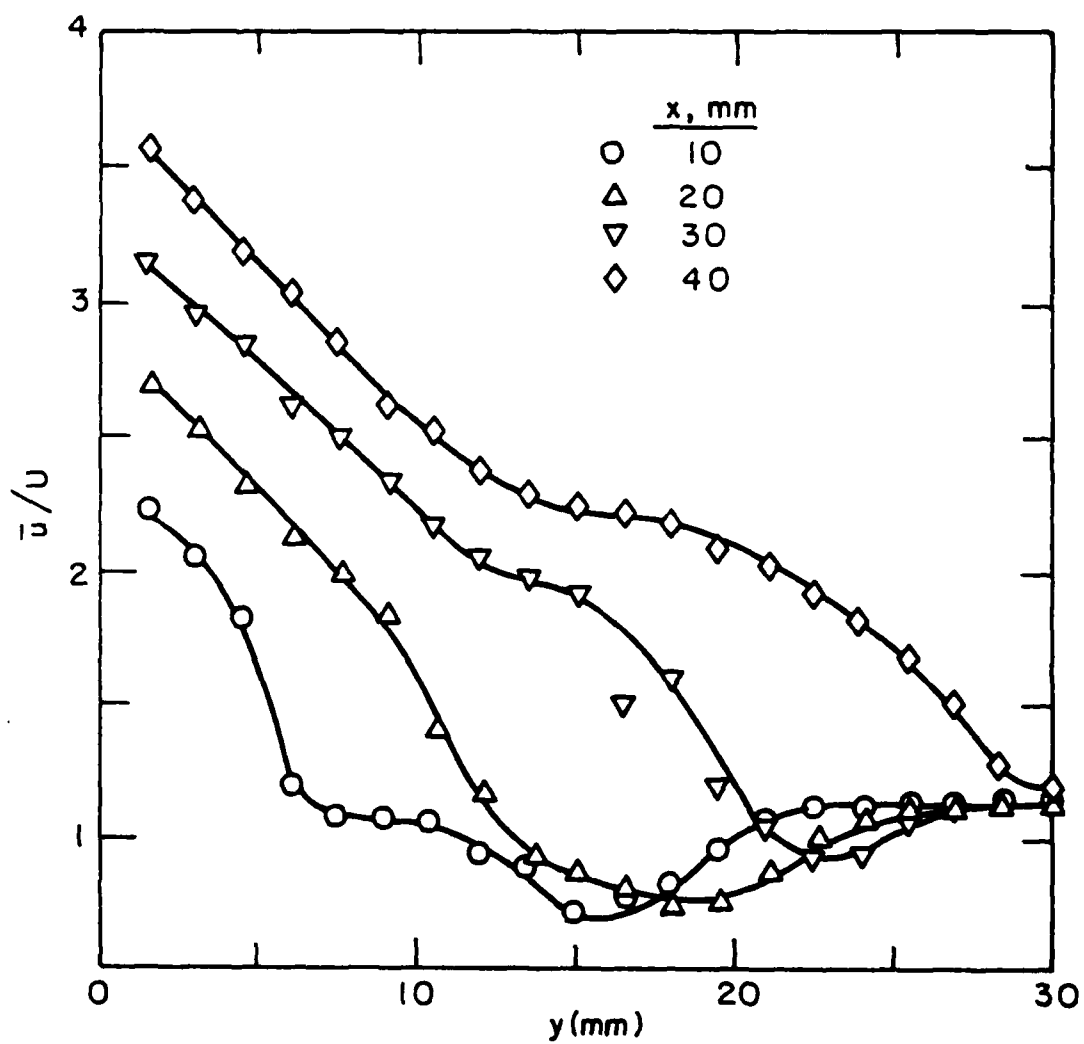
Figure 4.3b

XBL808-5625
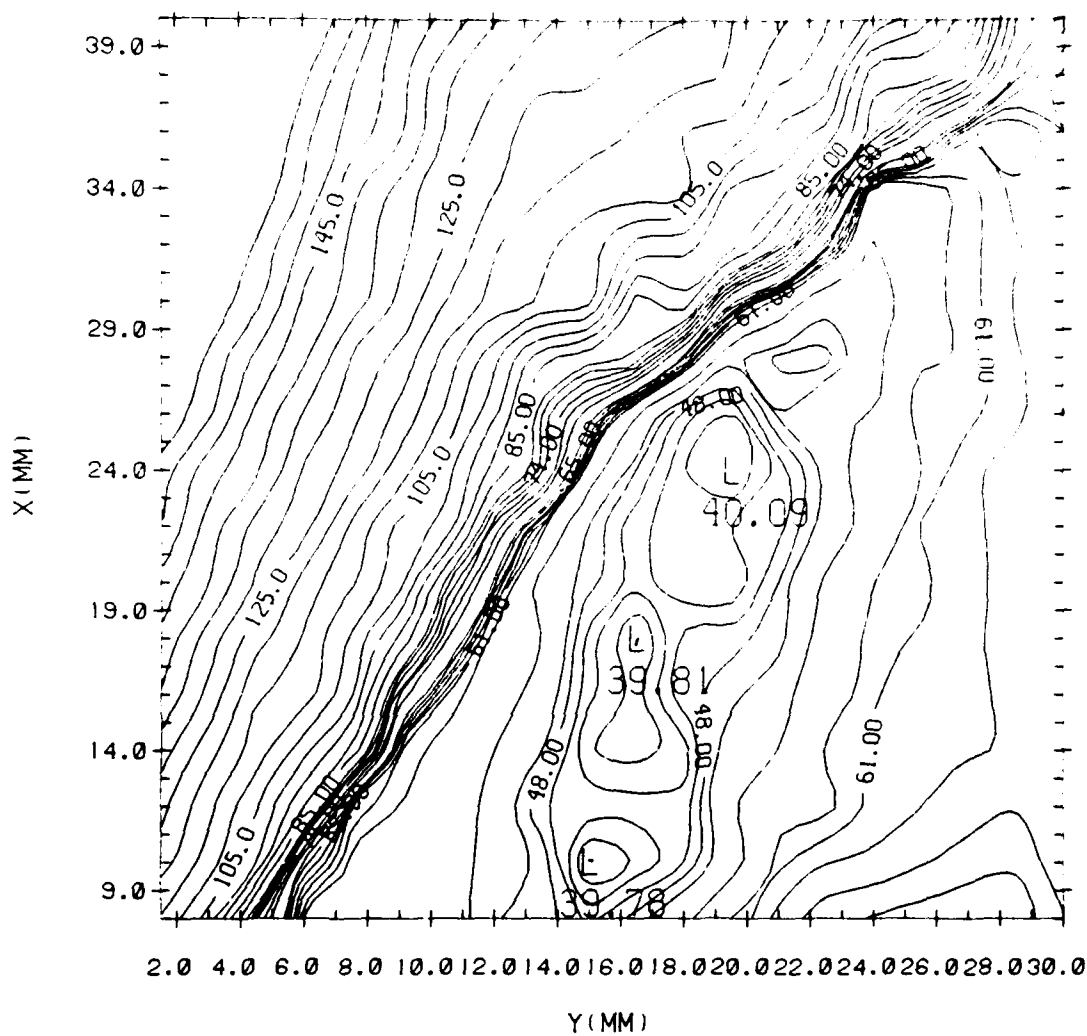
F2F07 UMEAN CONTOURS U00=55.0, D=2.00

CONTOUR FROM   39.776   TO   196.75   CONTOUR INTERVAL OF   0.   PT(3.31=   105.49
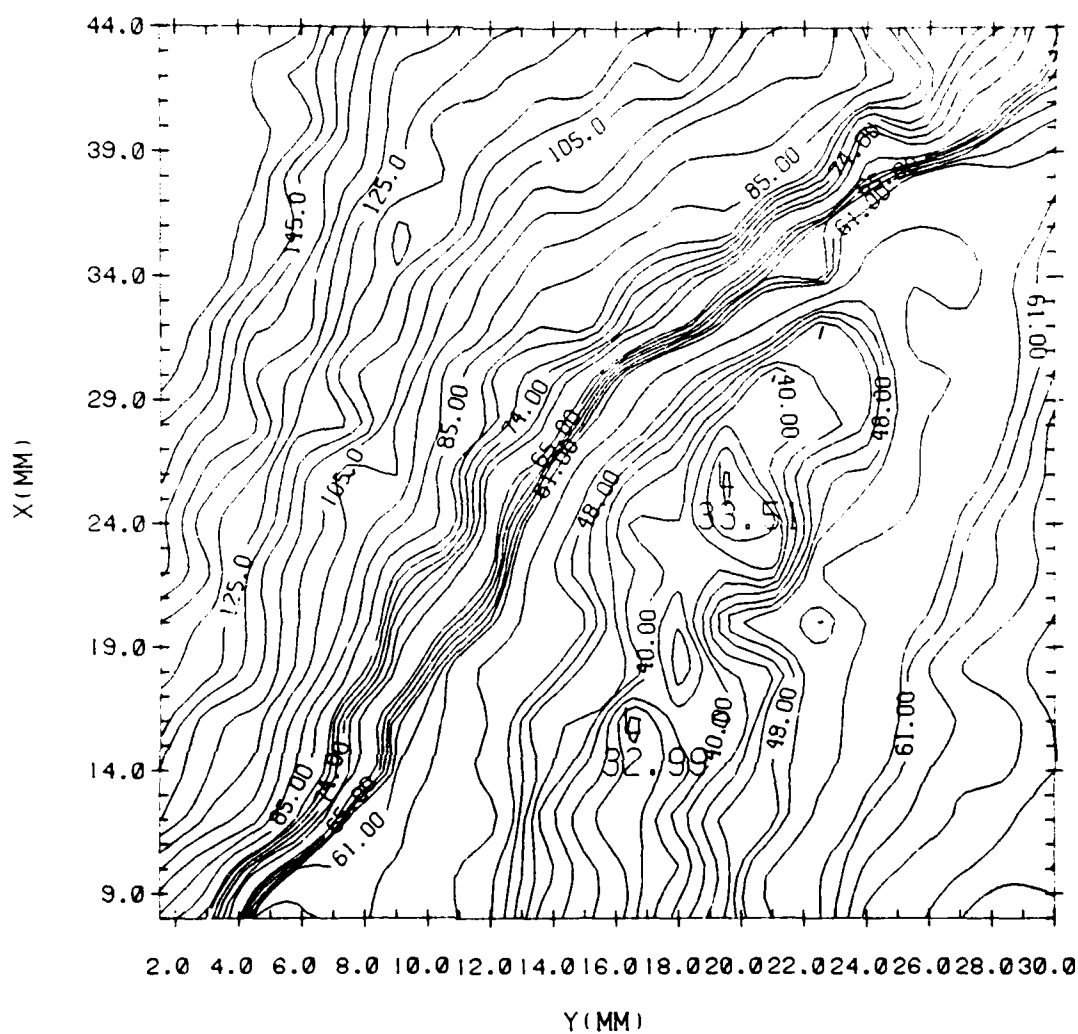
Figure 4.4a

F3F10 UMEAN CONTOURS U00=55.0, D=3.00

CONTOUR FROM   32.987   TO   187.27   CONTOUR INTERVAL OF   0.   PT(3.3)=   96.799

Figure 4.4b

CONSTANT U CONTOURS KARMAN VORTEX STREET

(b)

Y(MM)

X(MM)

KARMAN VORTEX STREET

(a)
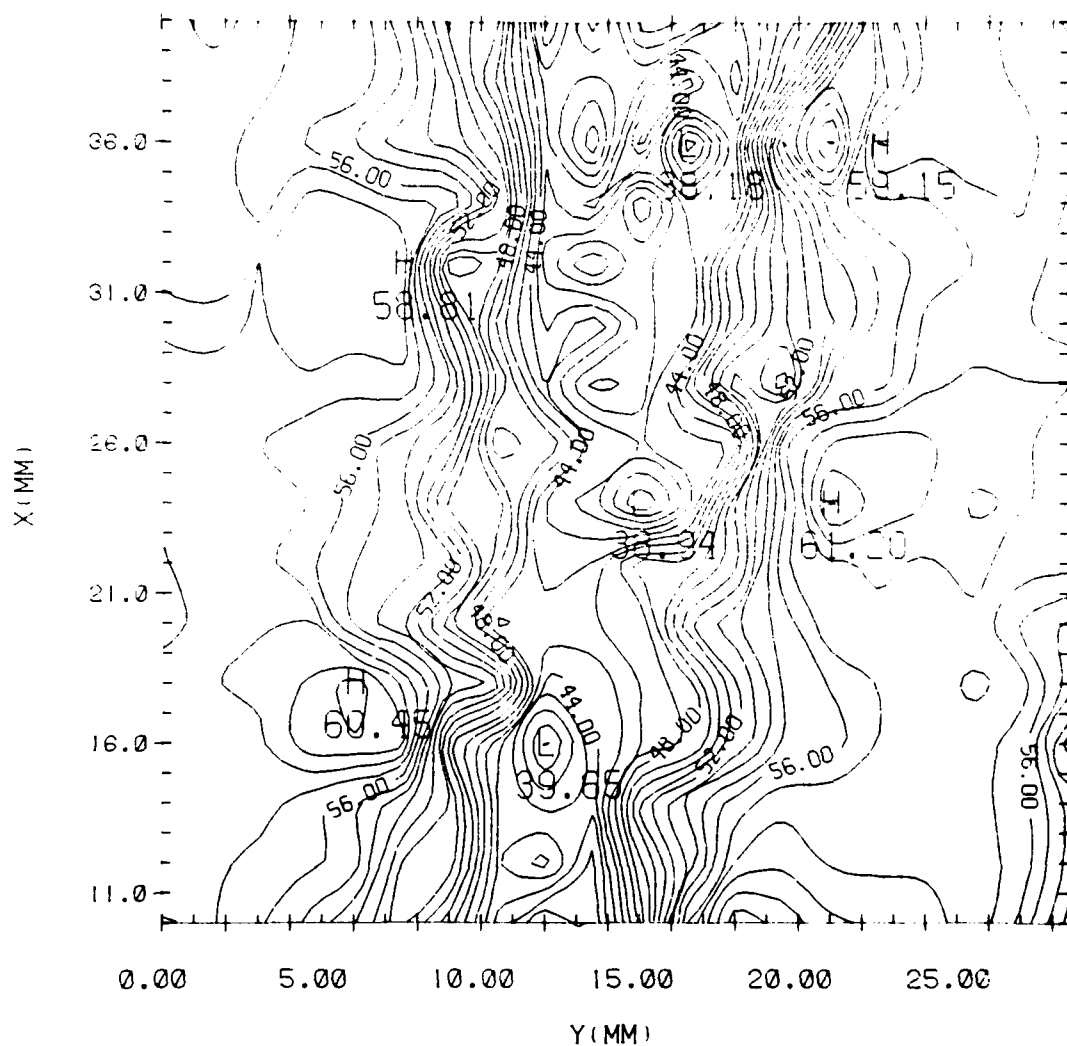
Figure 4.5

CONSTANT U CONTOURS T/TAU=0.25

CONTOUR FROM   38.000   TO   61.000   CONTOUR INTERVAL OF   1.0000   PT(3.3)=   57.488

Figure 4.6a
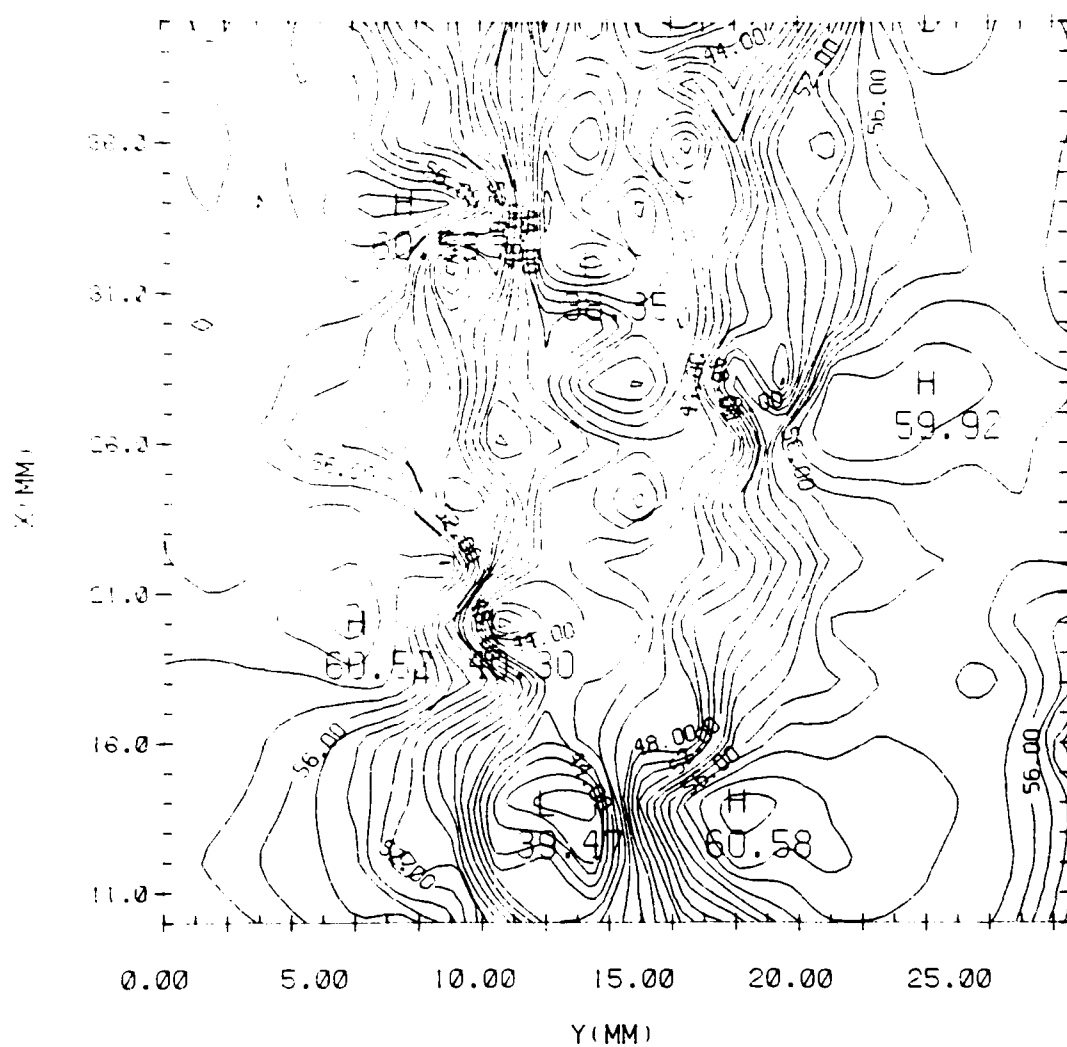
CONSTANT U CONTOURS T/TAU=0.50

CONTOUR FROM 38.000 TO 60.000 CONTOUR INTERVAL OF 1.0000 PT(3.31= 56.755

Figure 4.6b
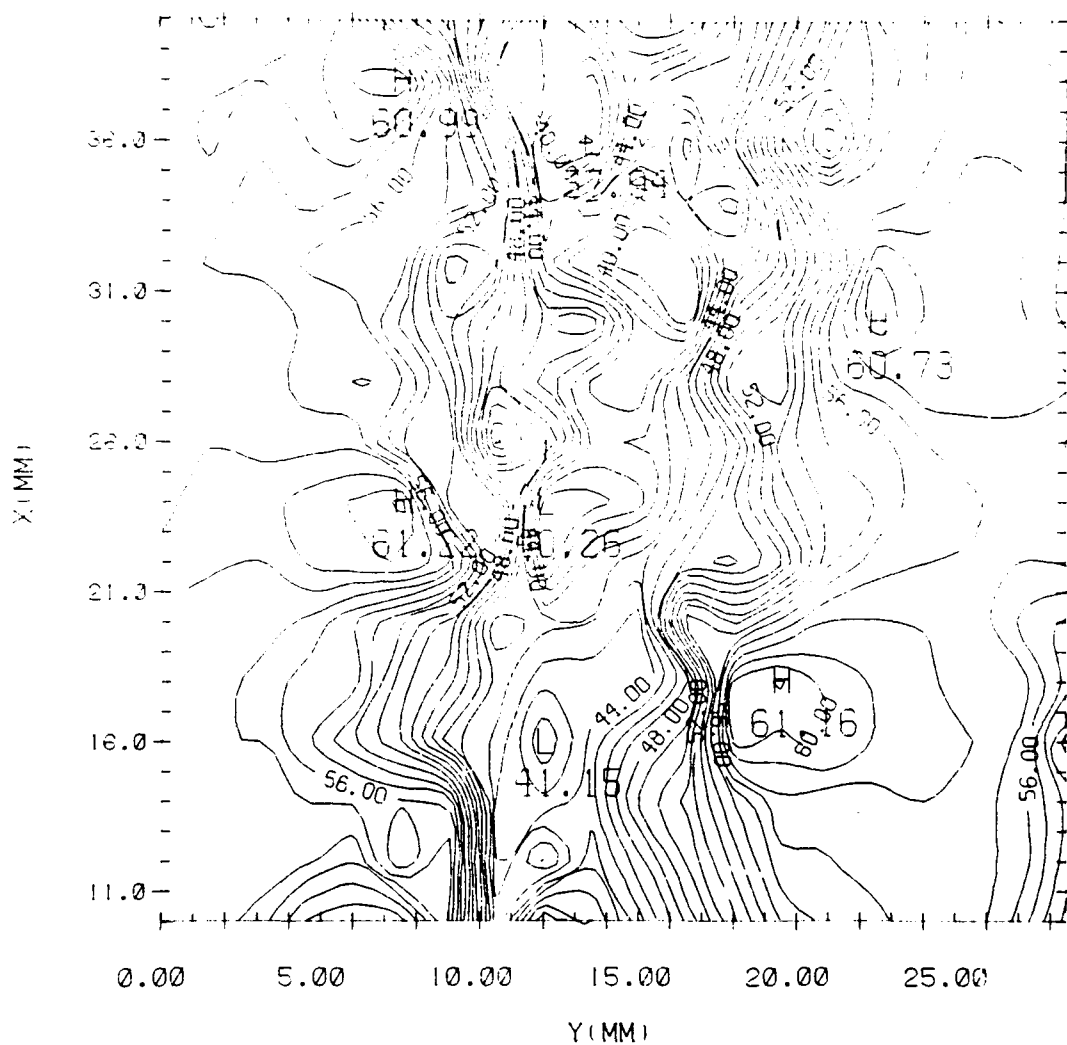
CONSTANT U CONTOURS T/TAU=0.75

CONTOUR FROM 37.000 TO 61.000 CONTOUR INTERVAL OF 1.0000 PT(3.3)= 57.543
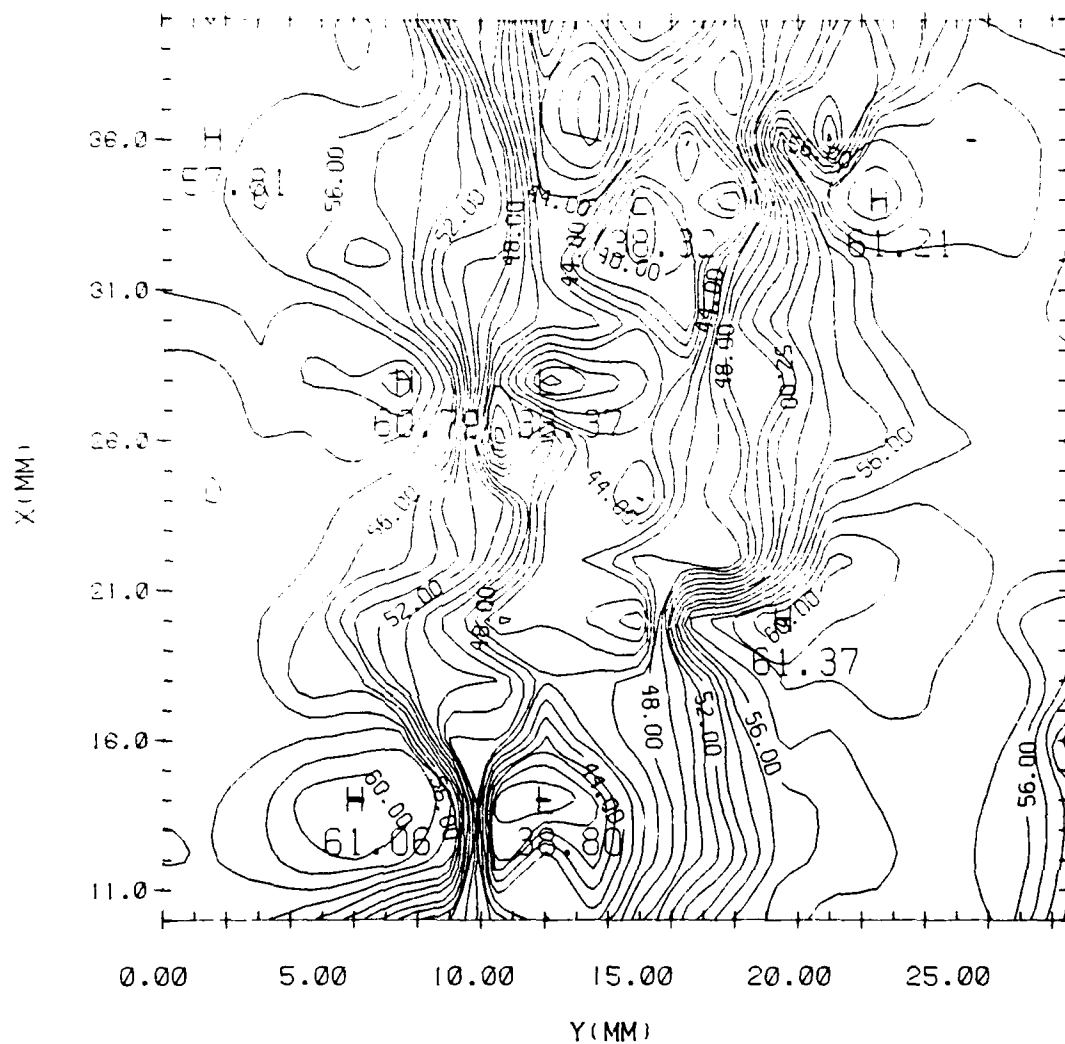
Figure 4.6c

CONSTANT U CONTOURS T/TAU=1.00

CONTOUR FROM   38.000   TO   61.000   CONTOUR INTERVAL OF   1.0000   PT(3.3)=   58.626

Figure 4.6d
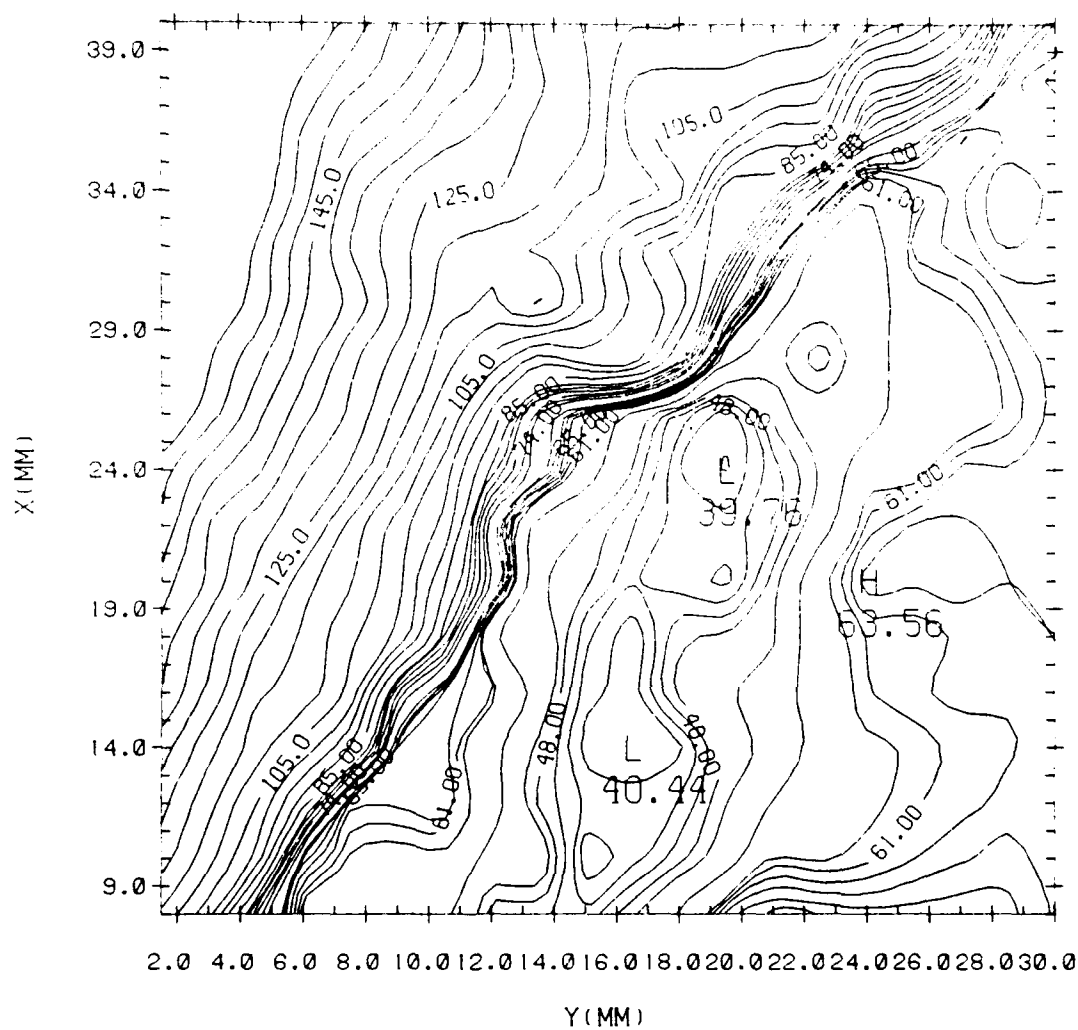
CONSTANT U CONTOURS T/TAU=0.25

CONTOUR FROM 39.757 TO 196.72 CONTOUR INTERVAL OF 0. PT(3.3)= 104.80

Figure 4.7a

CONSTANT U CONTOURS T/TAU=0.50

CONTOUR FROM   38.262   TO   196.64   CONTOUR INTERVAL OF   0.   PT(3.31=   104.88
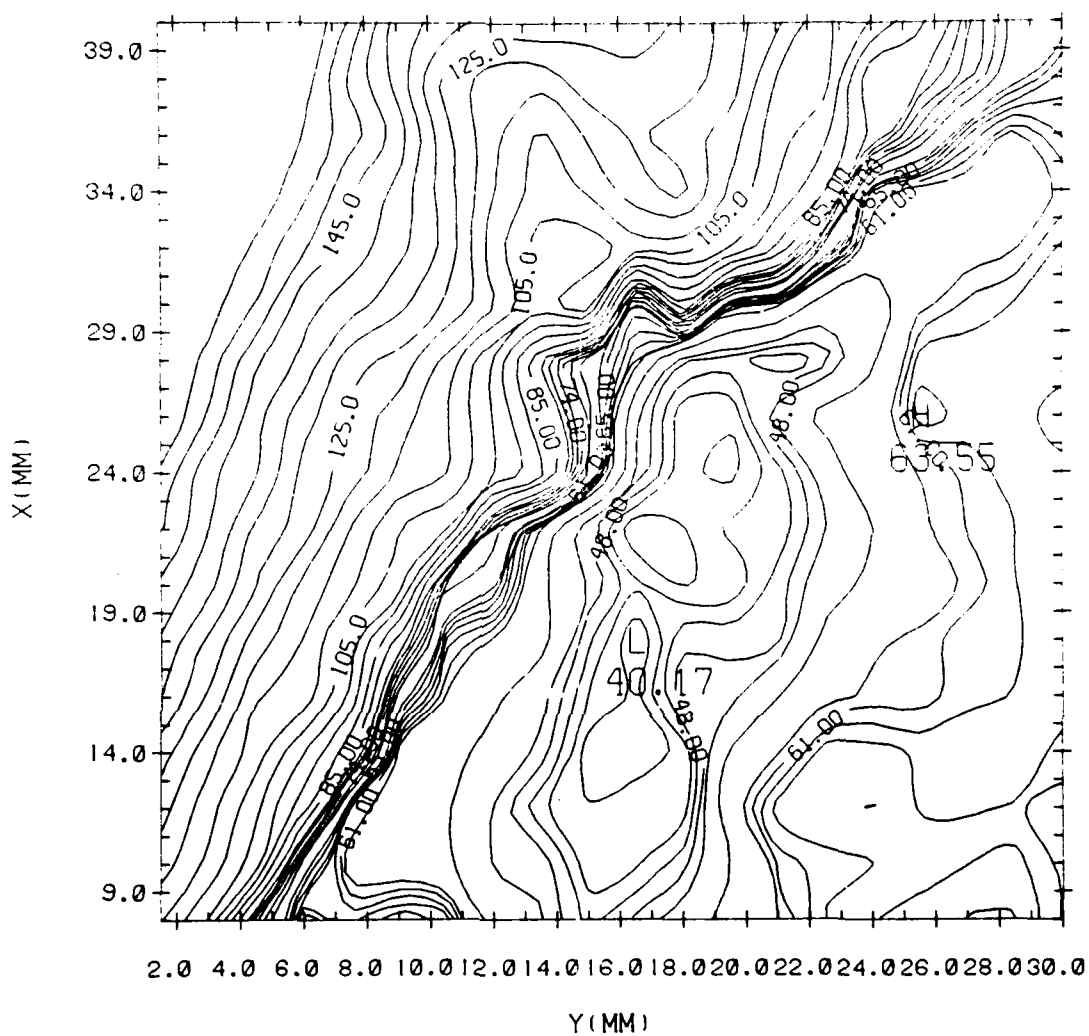
Figure 4.7b

CONSTANT U CONTOURS T/TAU=0.75

CONTOUR FROM   40.170   TO   198.05   CONTOUR INTERVAL OF   0.   PT(3,3)=   105.85

Figure 4.7c

CONSTANT U CONTOURS T/TAU=1.00
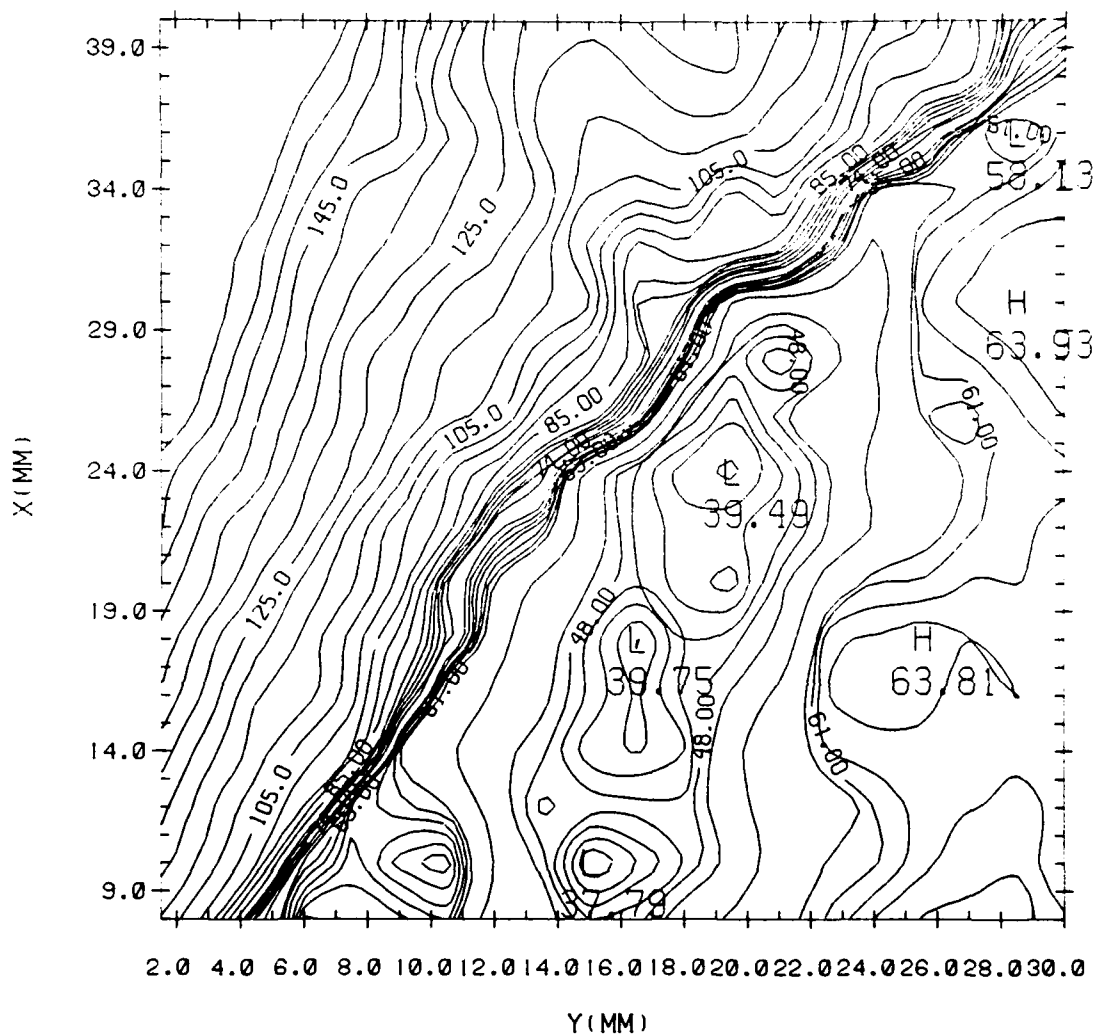
CONTOUR FROM 37.768 TO 195.60 CONTOUR INTERVAL OF 0. P.3.31= 106.49
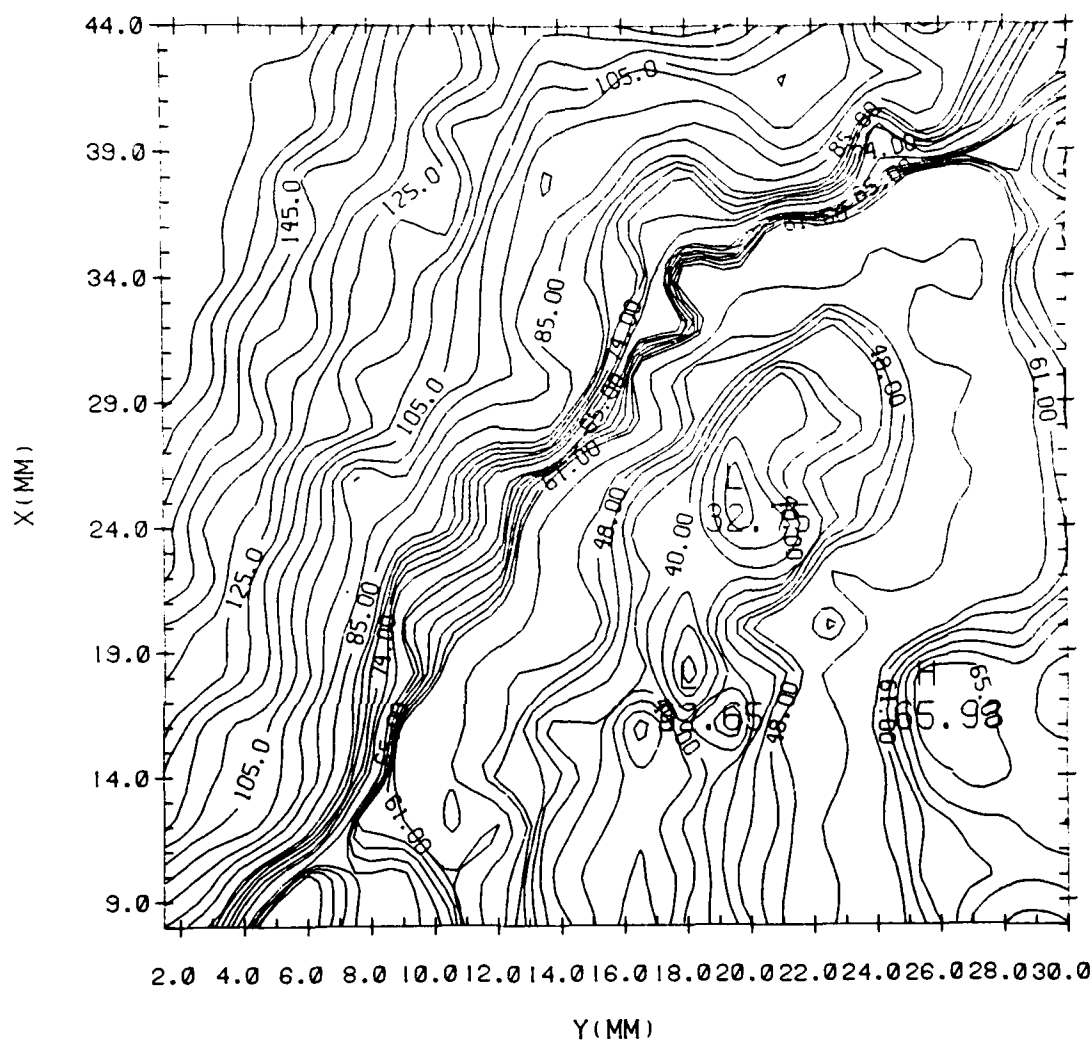
Figure 4.7d

CONSTANT U CONTOURS T/TAU=0.25

CONTOUR FROM   32.650   TO   186.53   CONTOUR INTERVAL OF   0.   PT(3.3)=   99.616

Figure 4.8a

Y(MM)
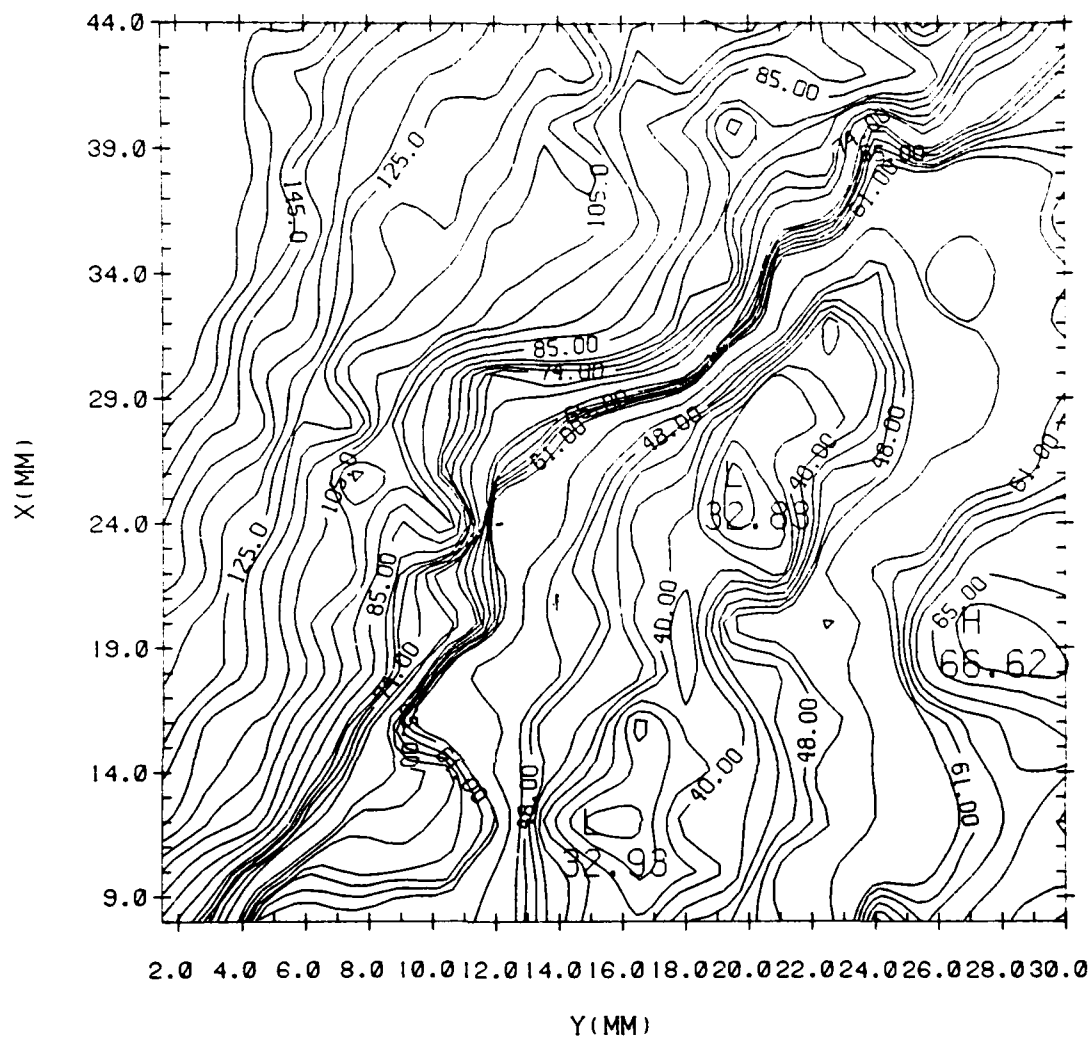
CONSTANT U CONTOURS T/TAU=0.50

CONTOUR FROM   32.833   TO   189.35   CONTOUR INTERVAL OF   0.   PT(3.31=   97.161

Figure 4.8b

CONSTANT U CONTOURS T/TAU=0.75

CONTOUR FROM 31.598   TO   188.42   CONTOUR INTERVAL OF   0.   PT(3,3)=   94.412

Figure 4.8c

CONSTANT U CONTOURS T/TAU=1.00

CONTOUR FROM 32.316 TO 190.21 CONTOUR INTERVAL OF 0. PT(3.3)= 96.008
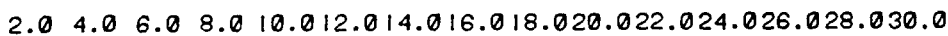
Figure 4.8d
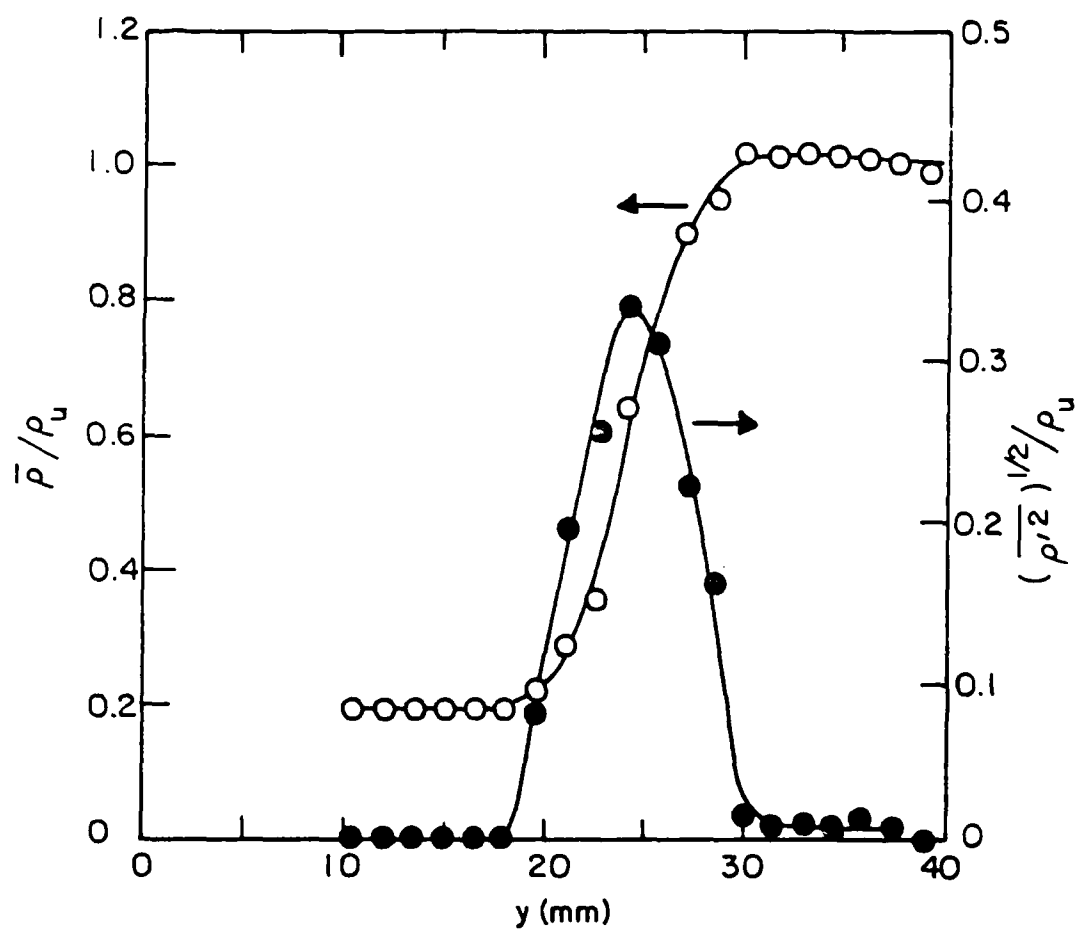
XBL 808-5619

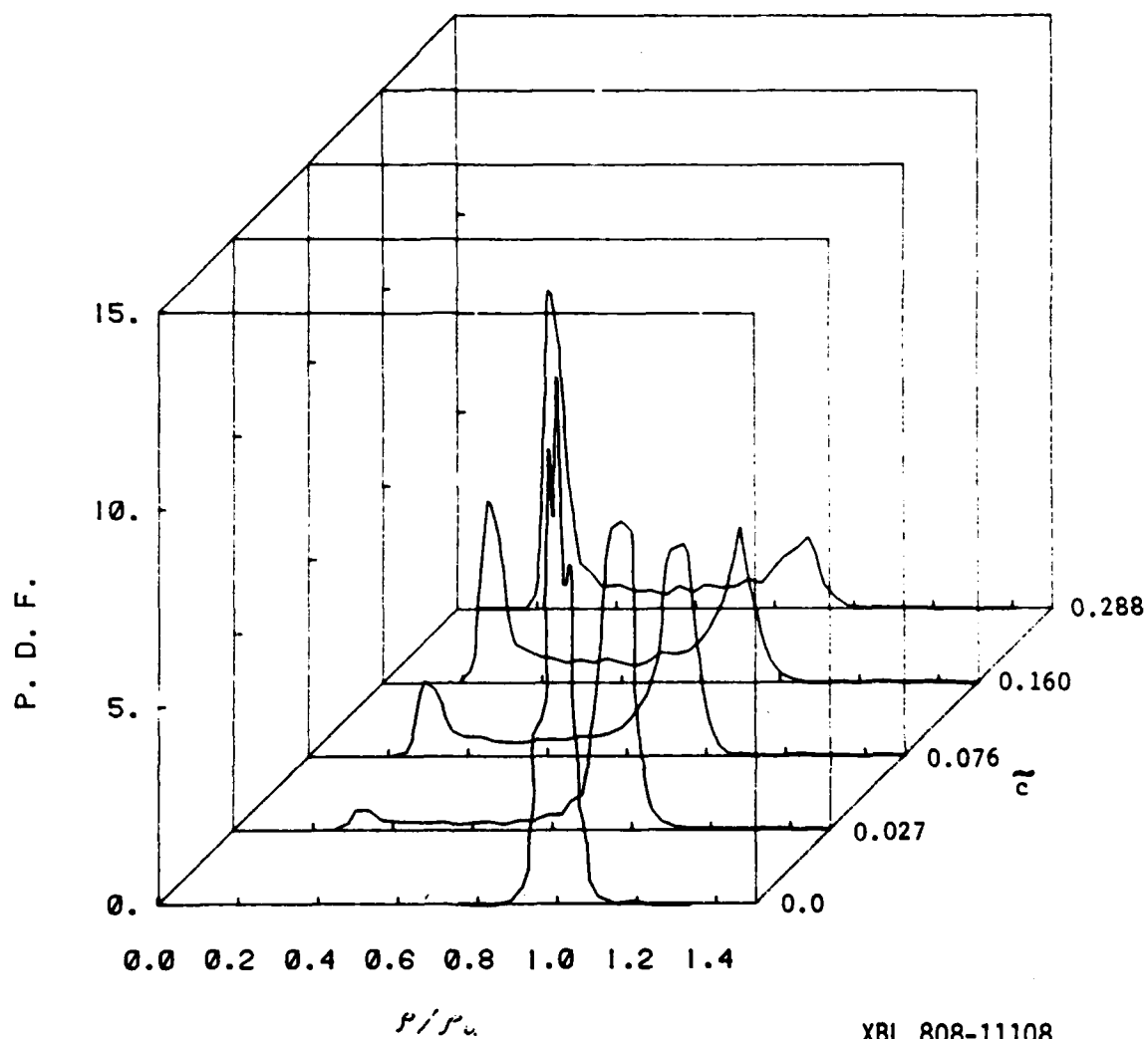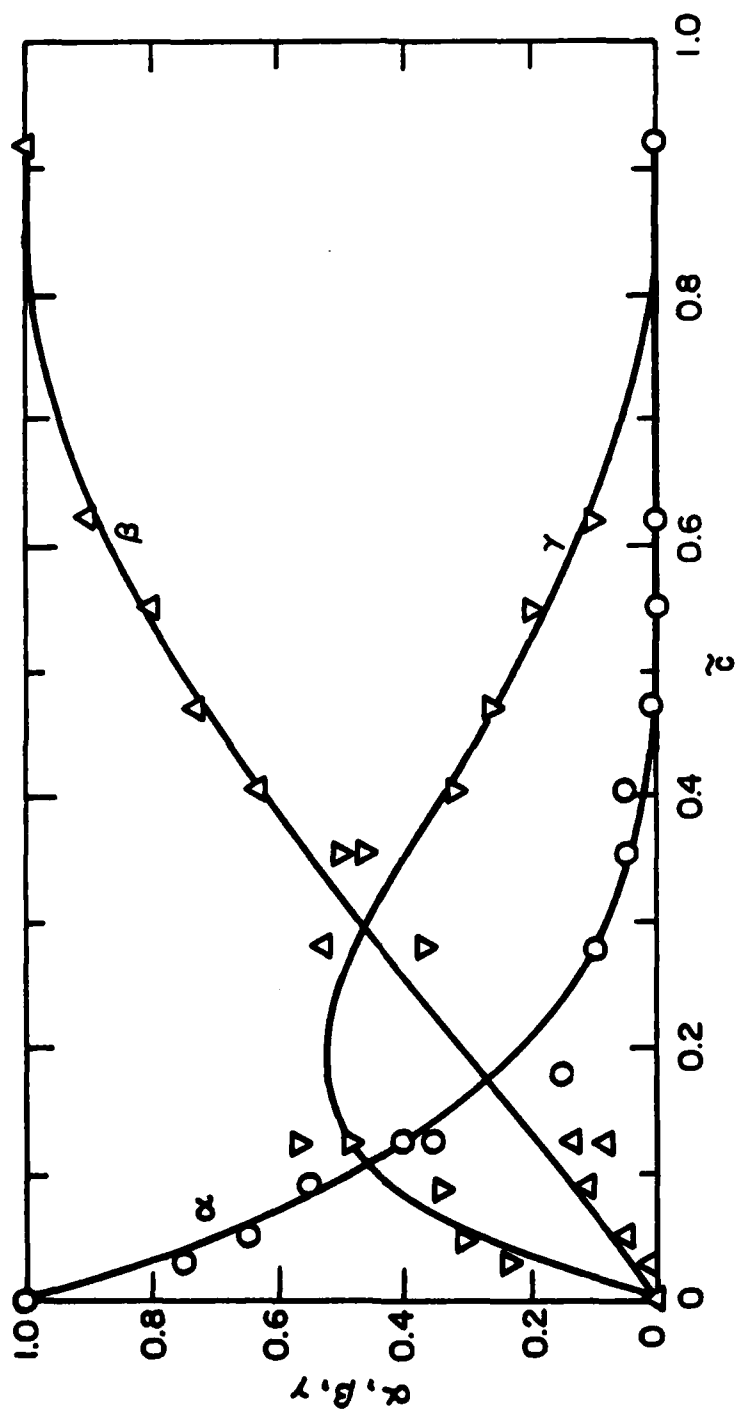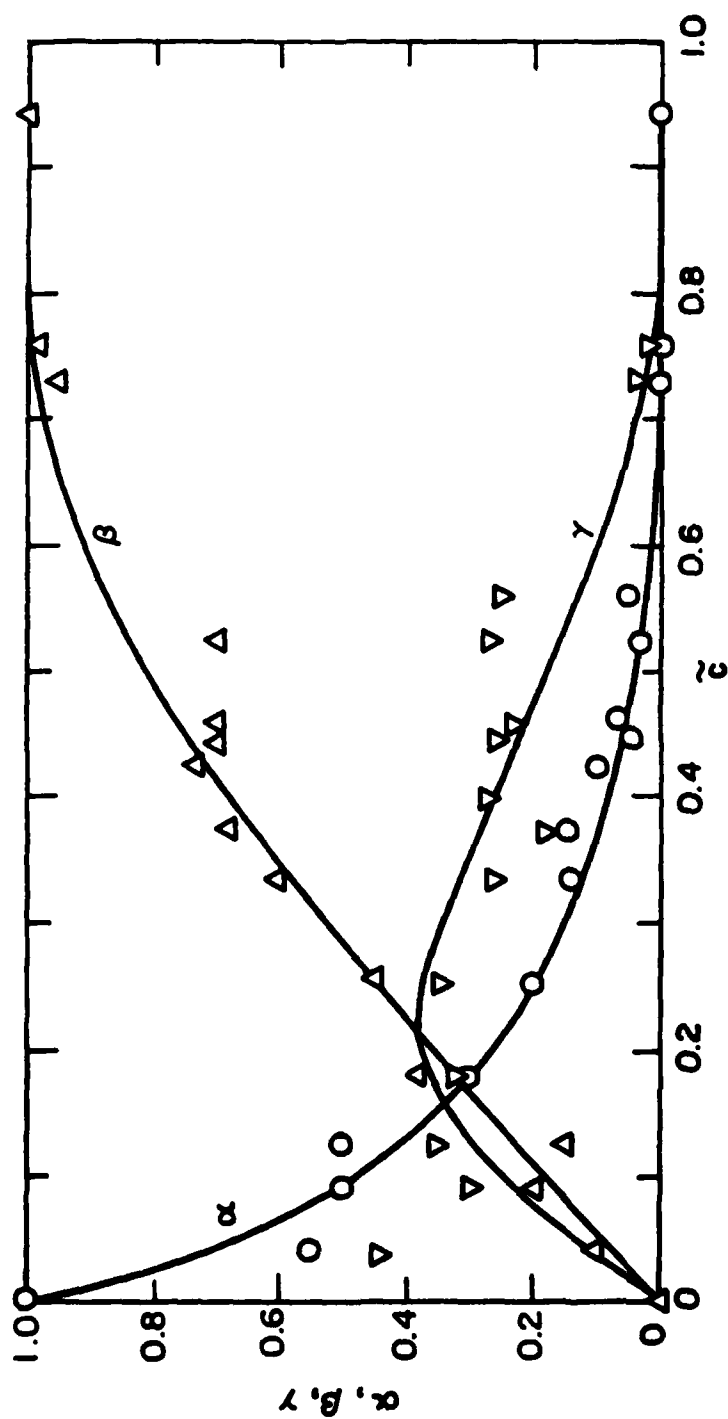Figure 5.1
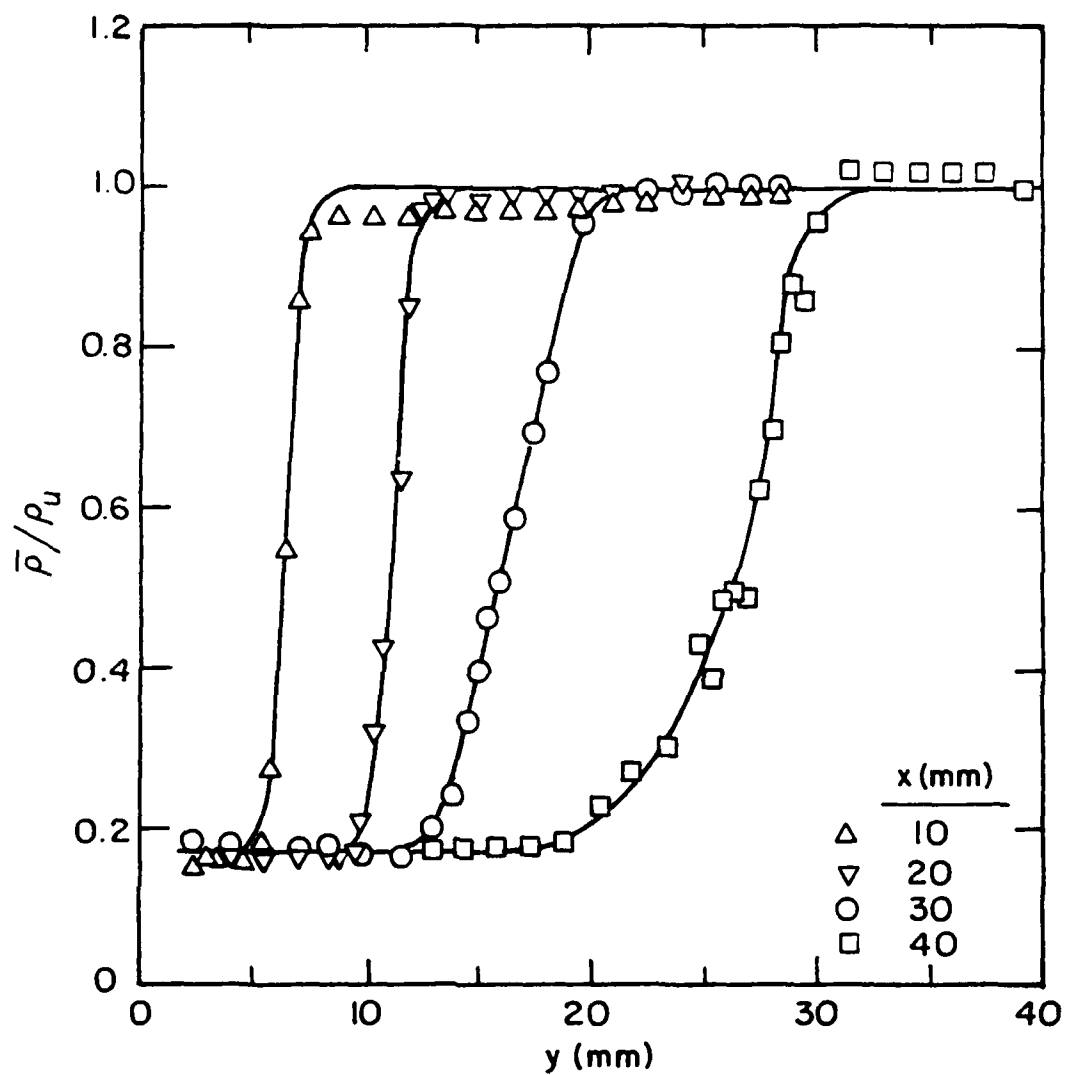
XBL 808-5608

Figure 5.2a
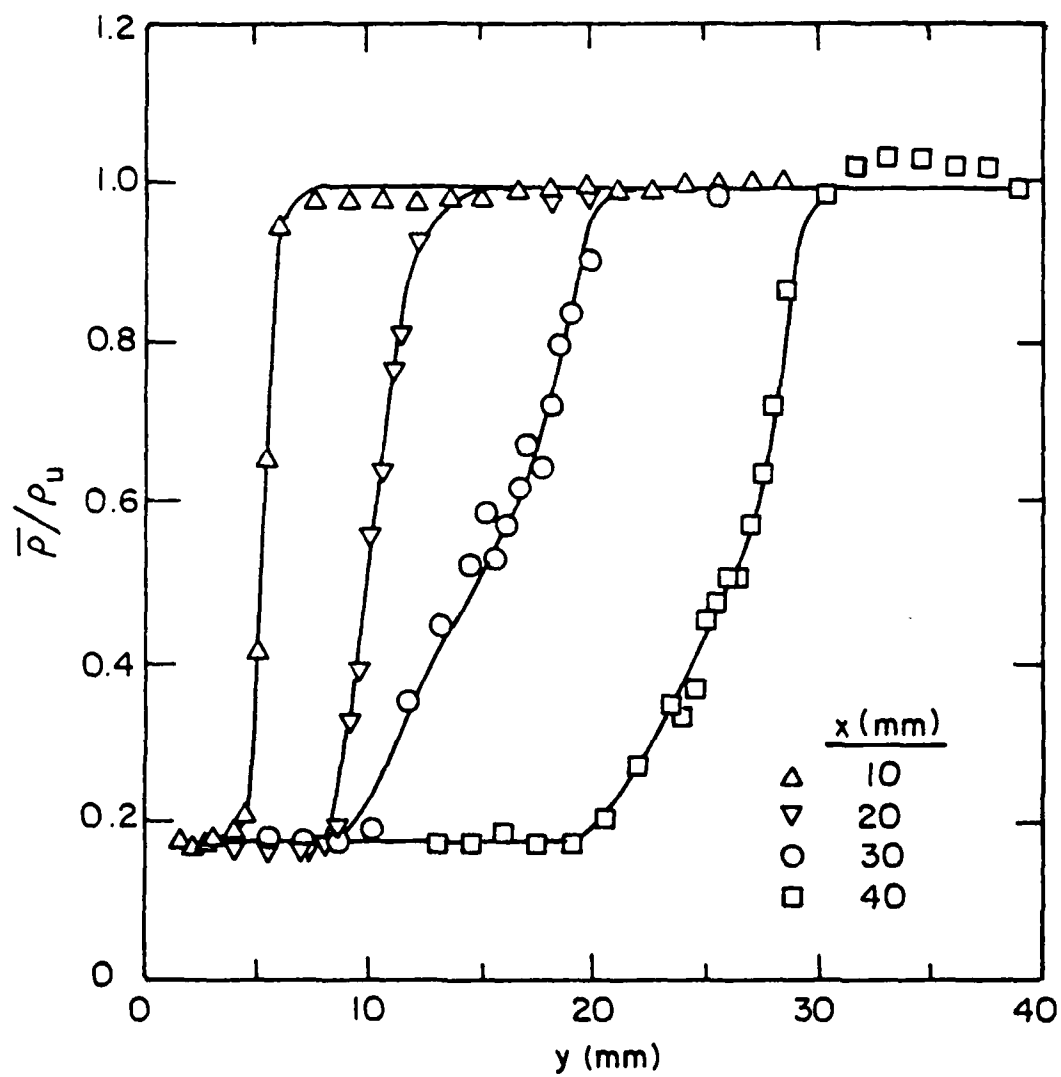
XBL 808-5613

Figure 5.2b
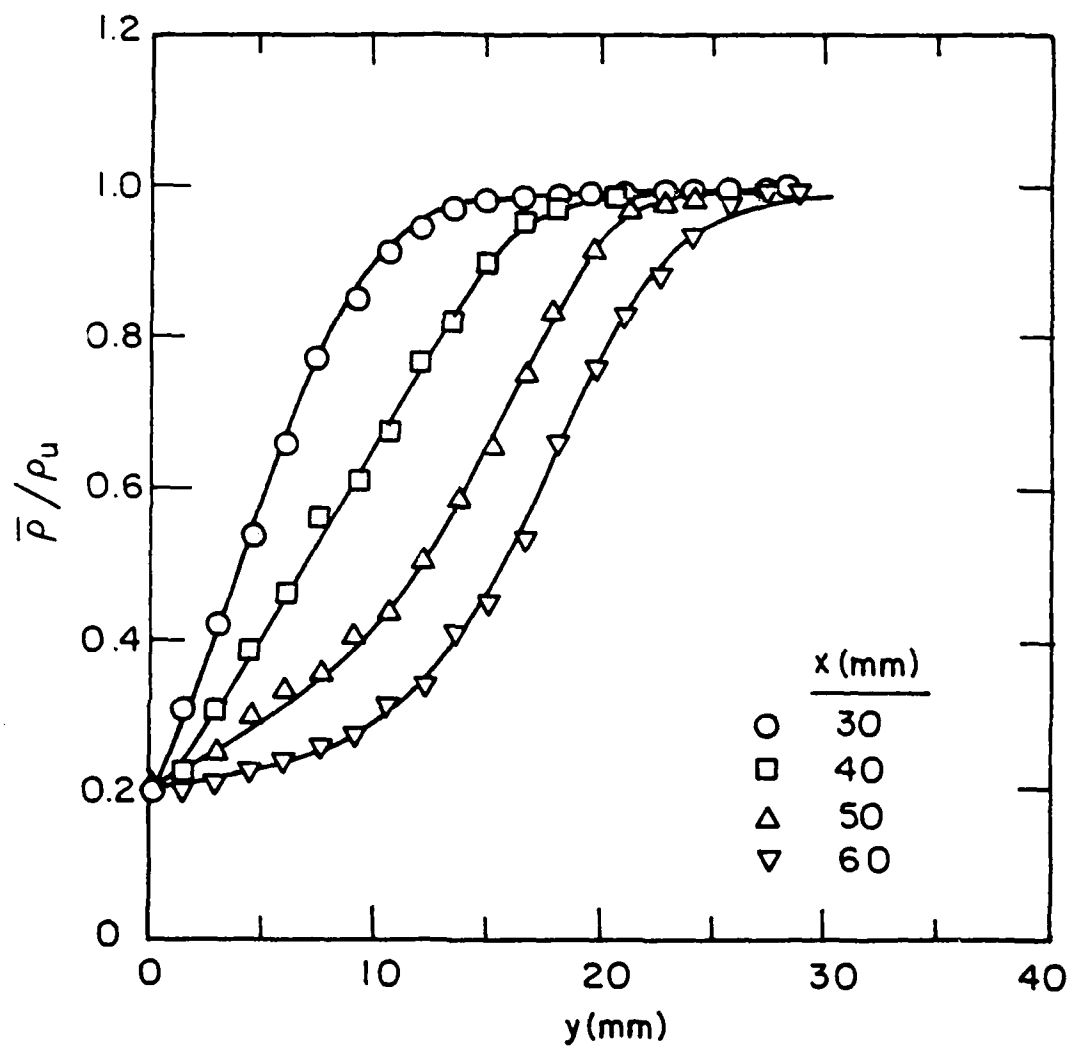
XBL 808-5610

Figure 5.2c
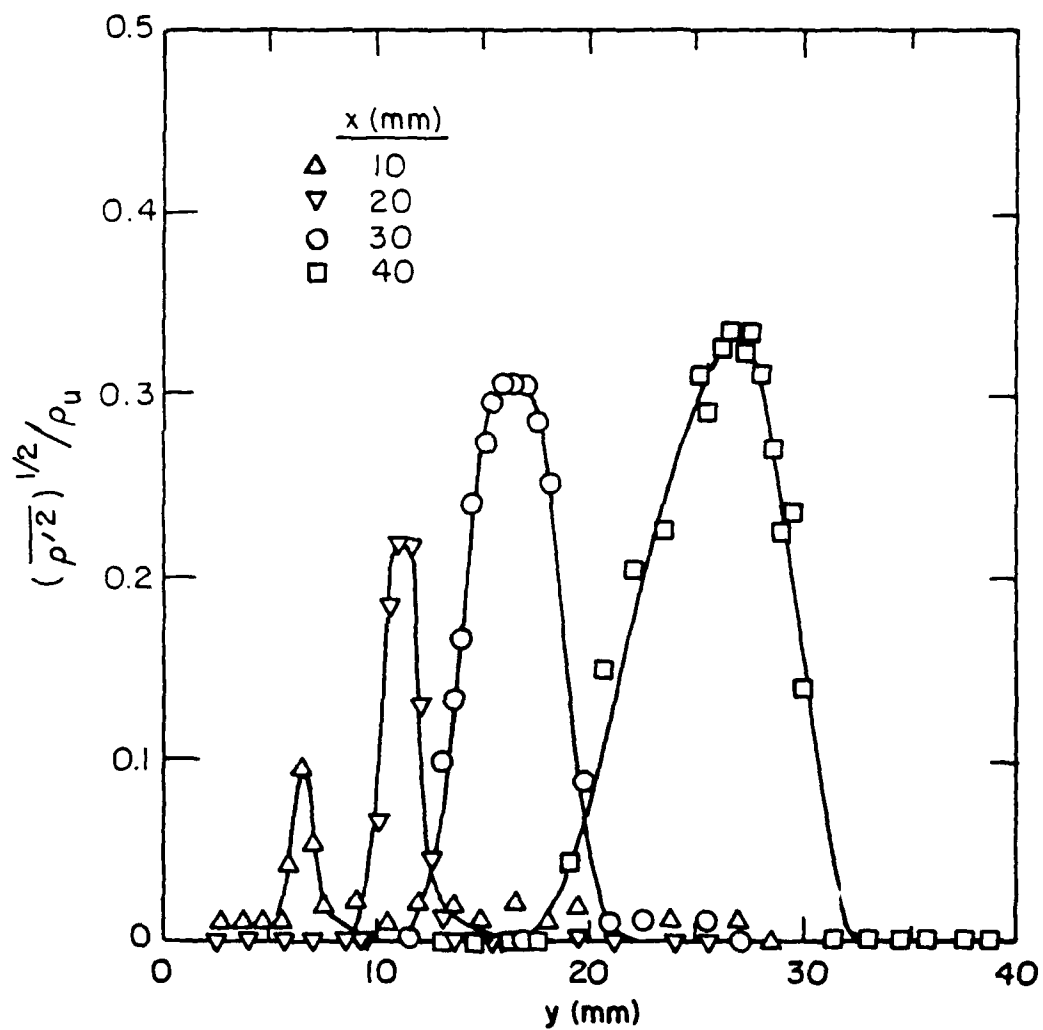
XBL 808-5612

Figure 5.3a
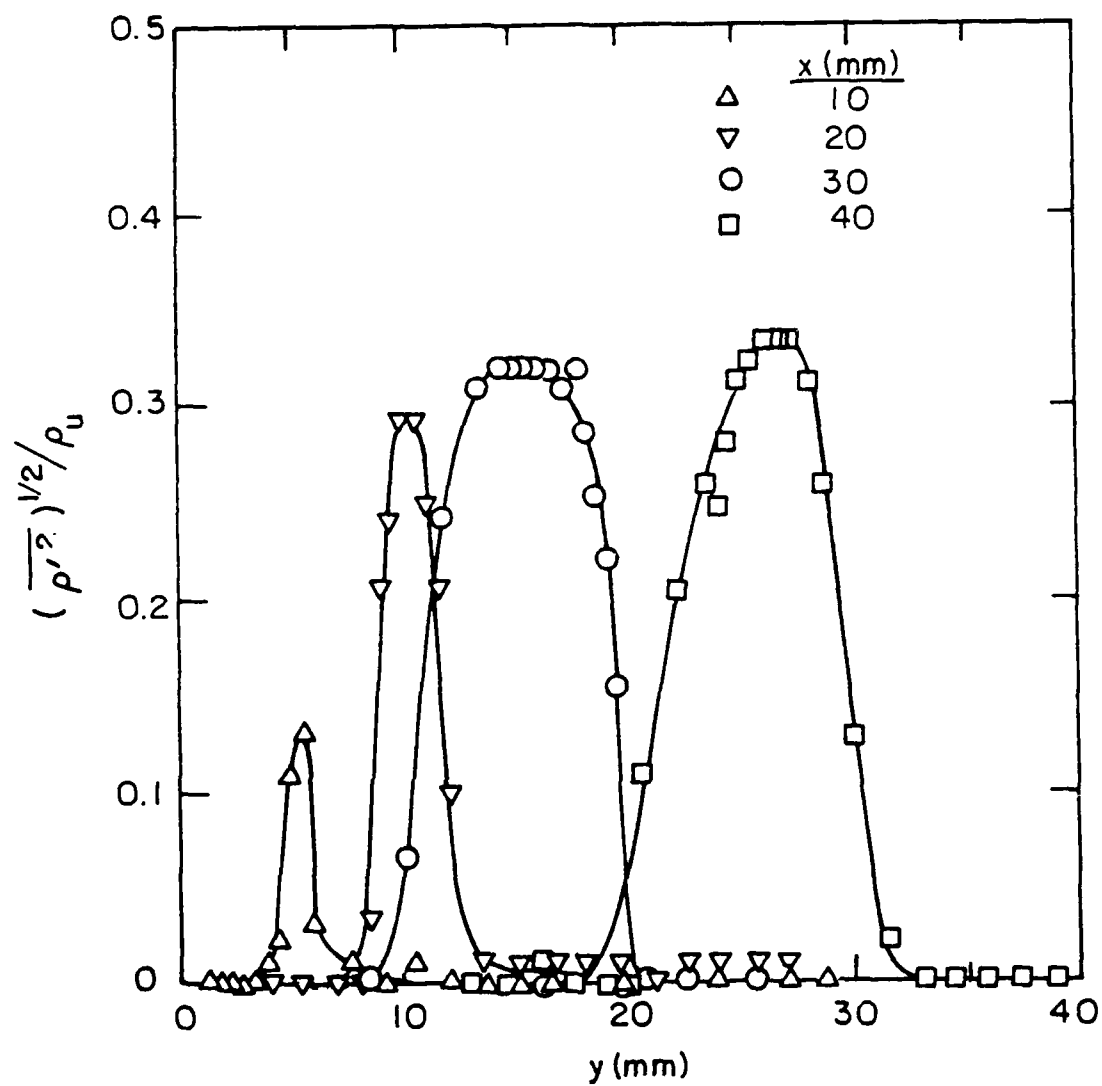
XBL 808-5611

Figure 5.3b
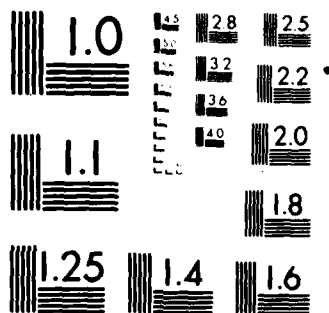
MICROCOPY RESOLUTION TEST CHART
NATIONAL BUREAU OF STANDARDS 1963 A
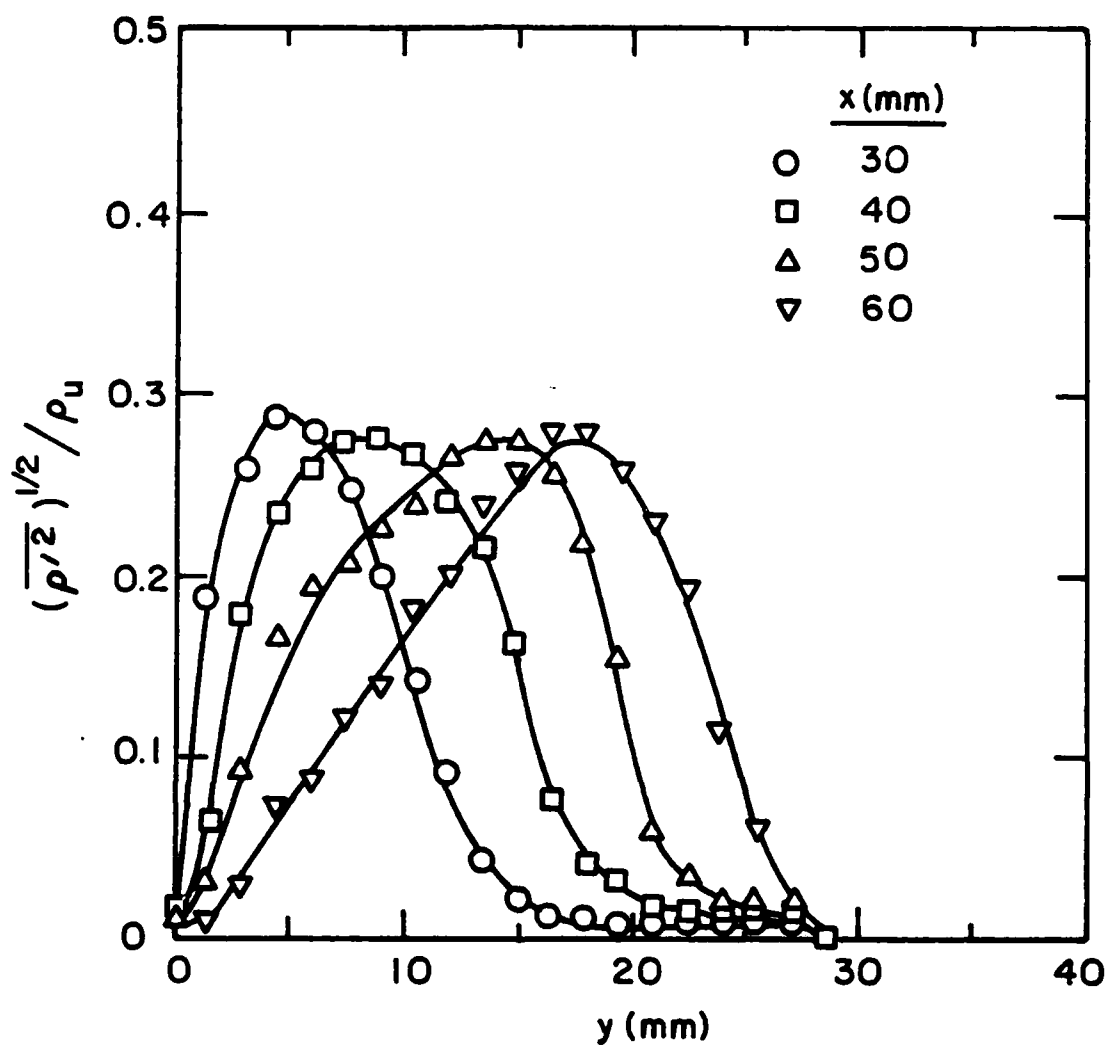
XBL 808-5609

Figure 5.3c
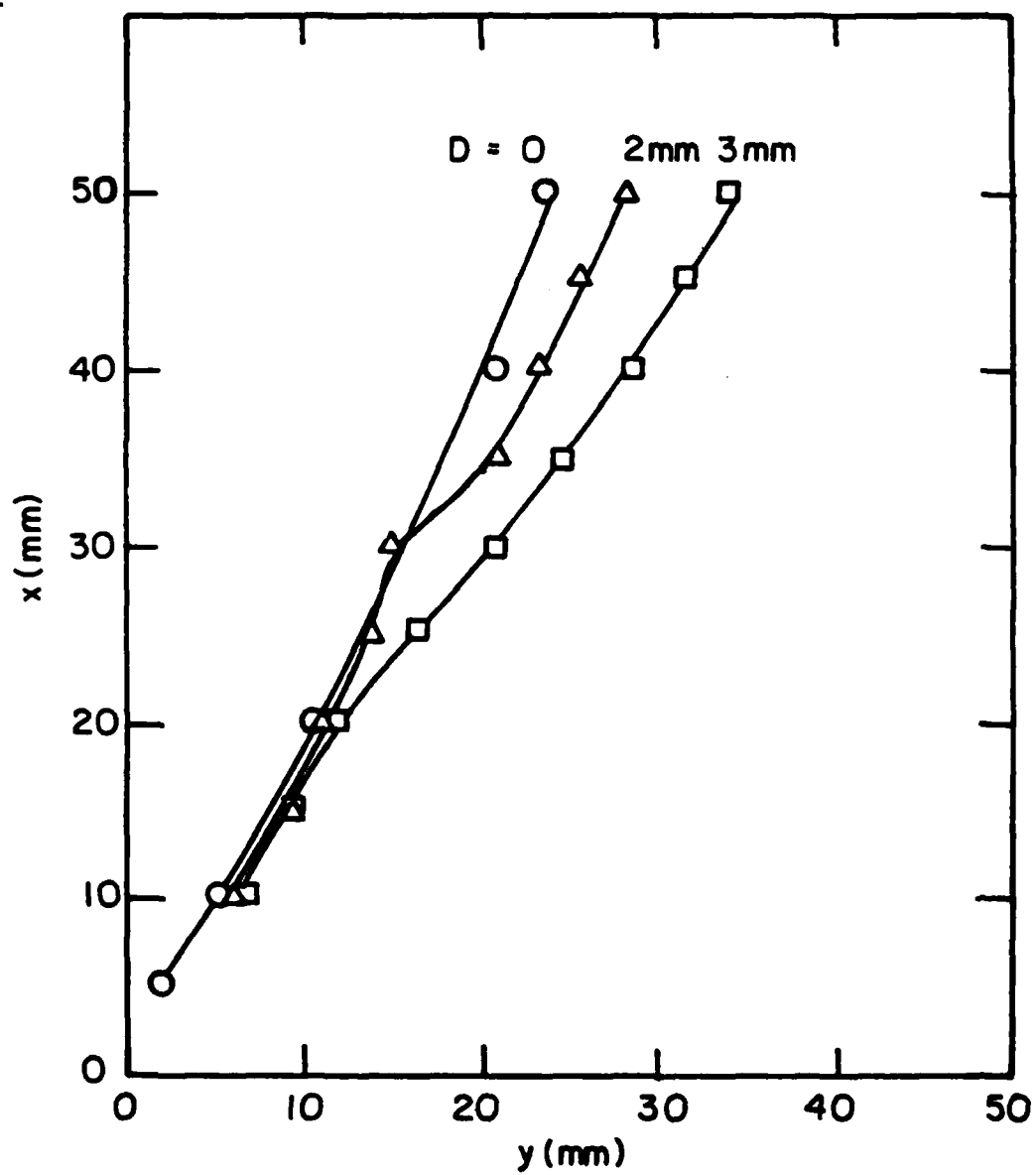
XBL808-5614

Figure 5.4
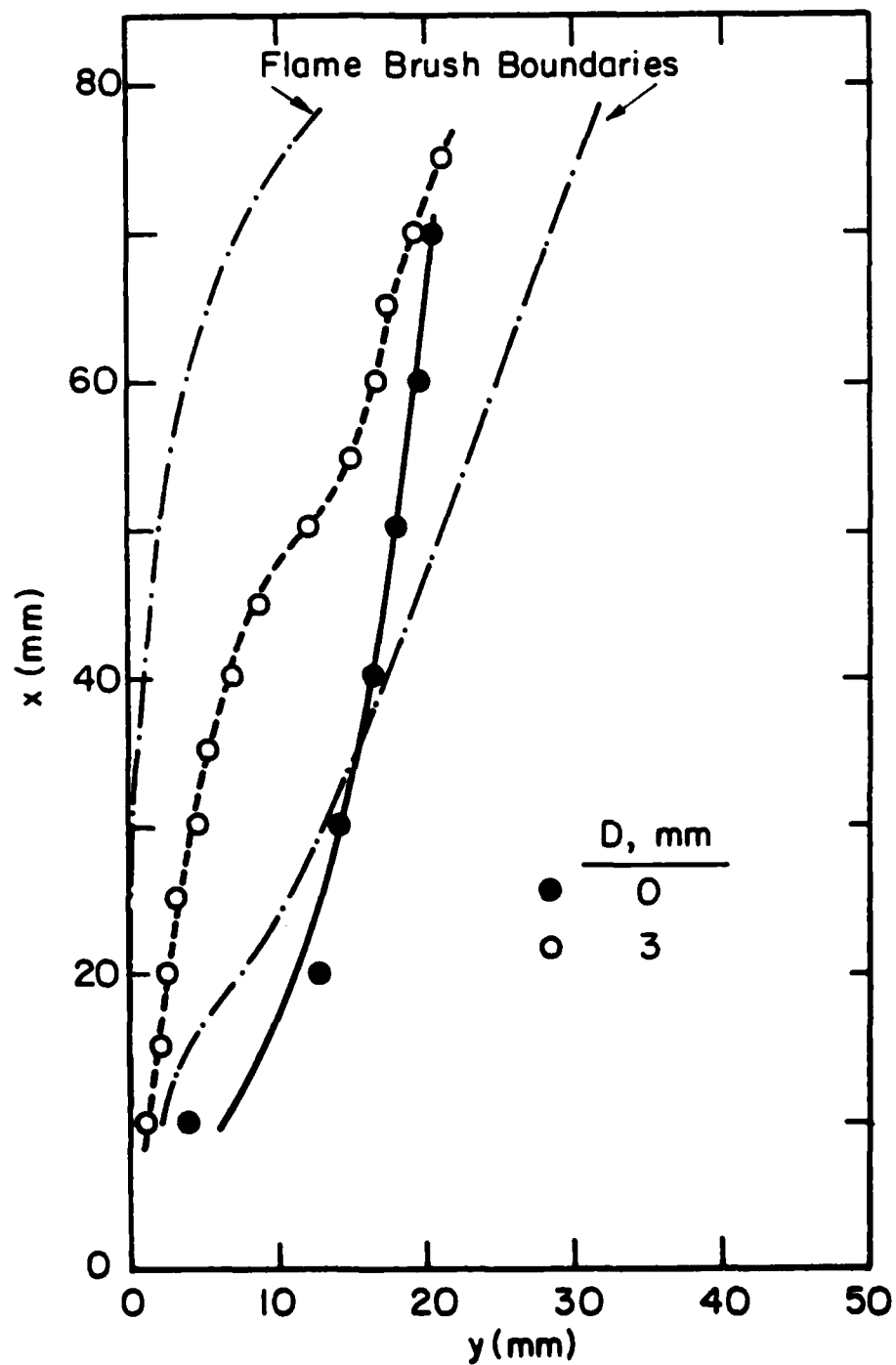
XBL 808-5618

Figure 5.5
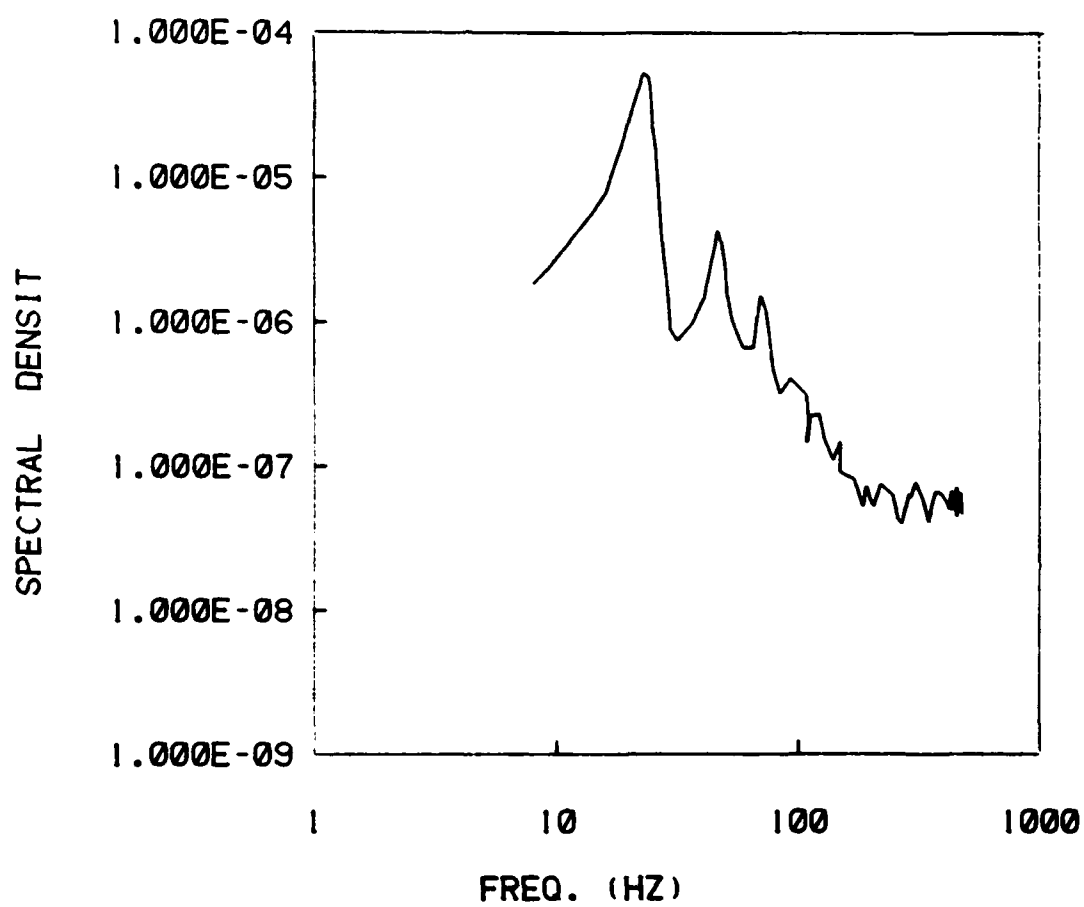
XBL 808-10838

Figure 5.6a

FREQ. (HZ)
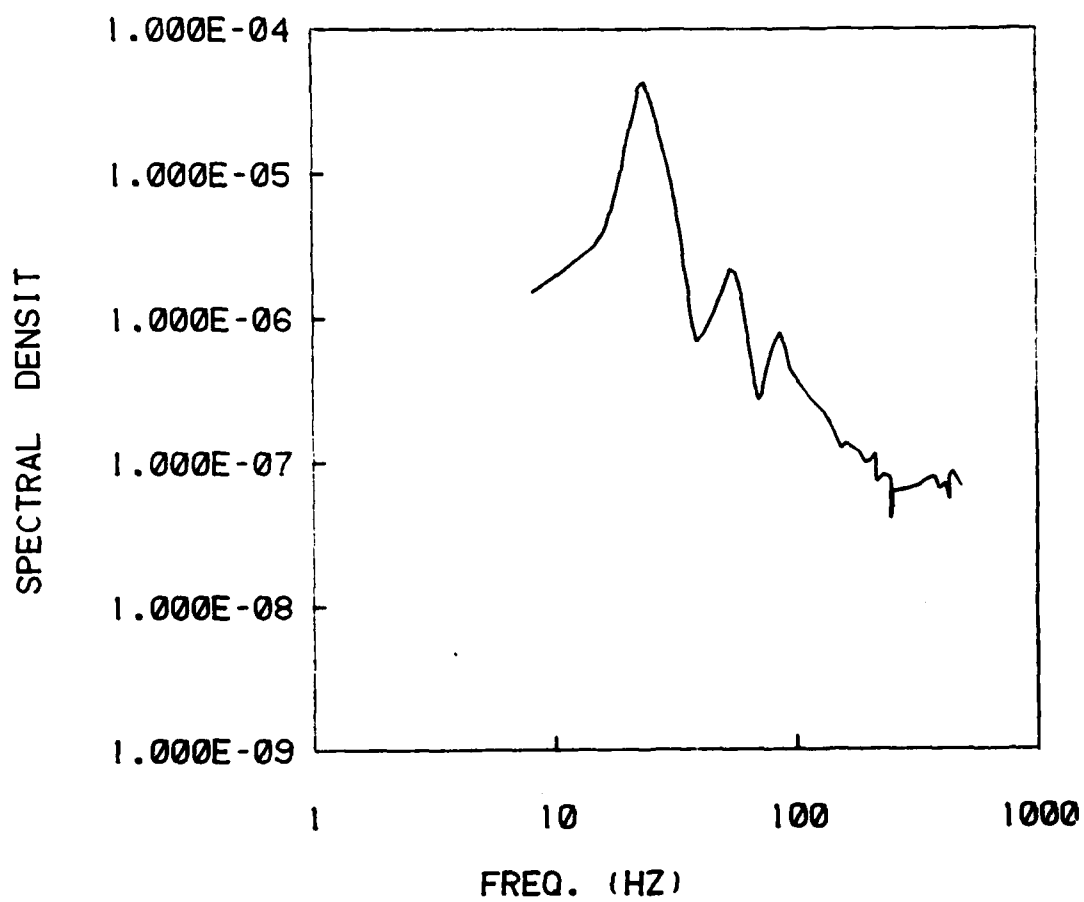
XBL 808-10845

Figure 5.6b
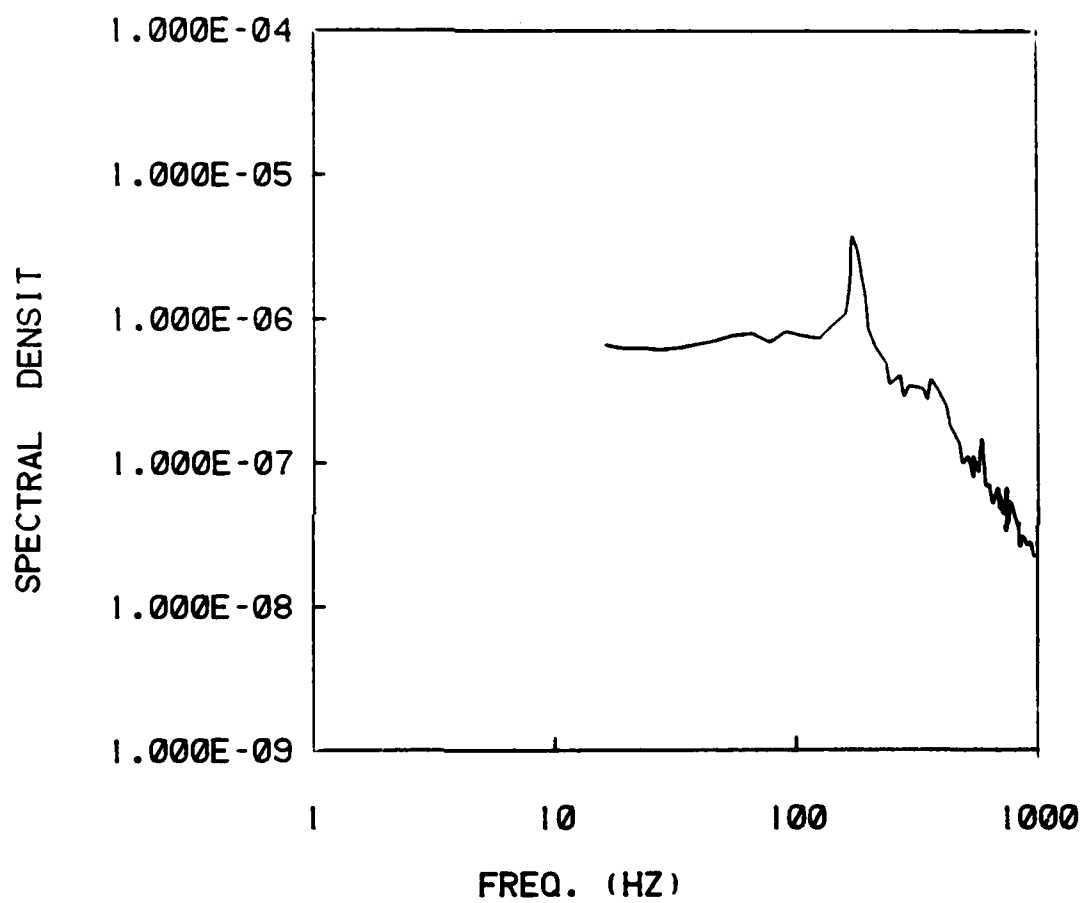
XBL 808-10841

Figure 5.6c
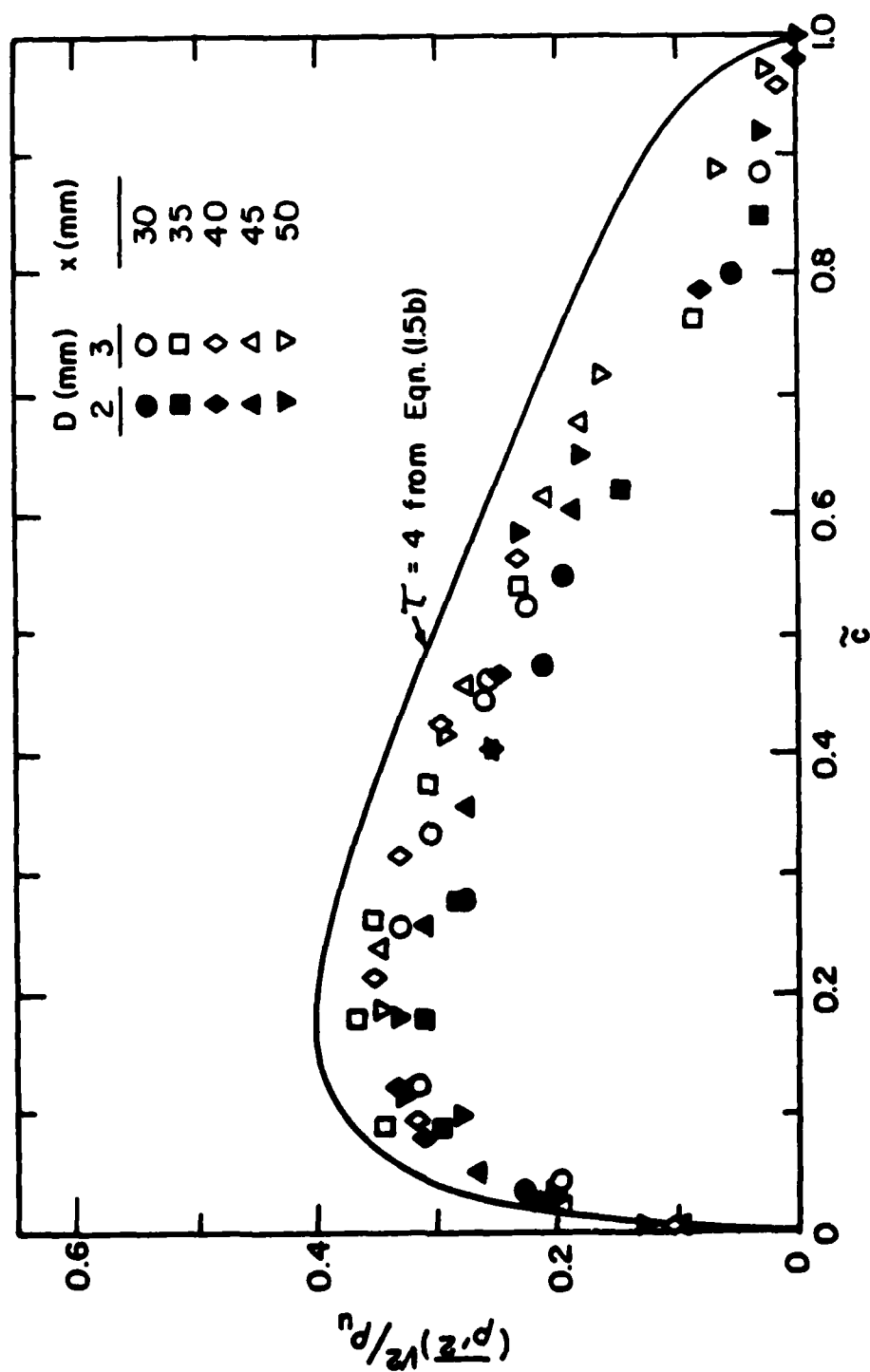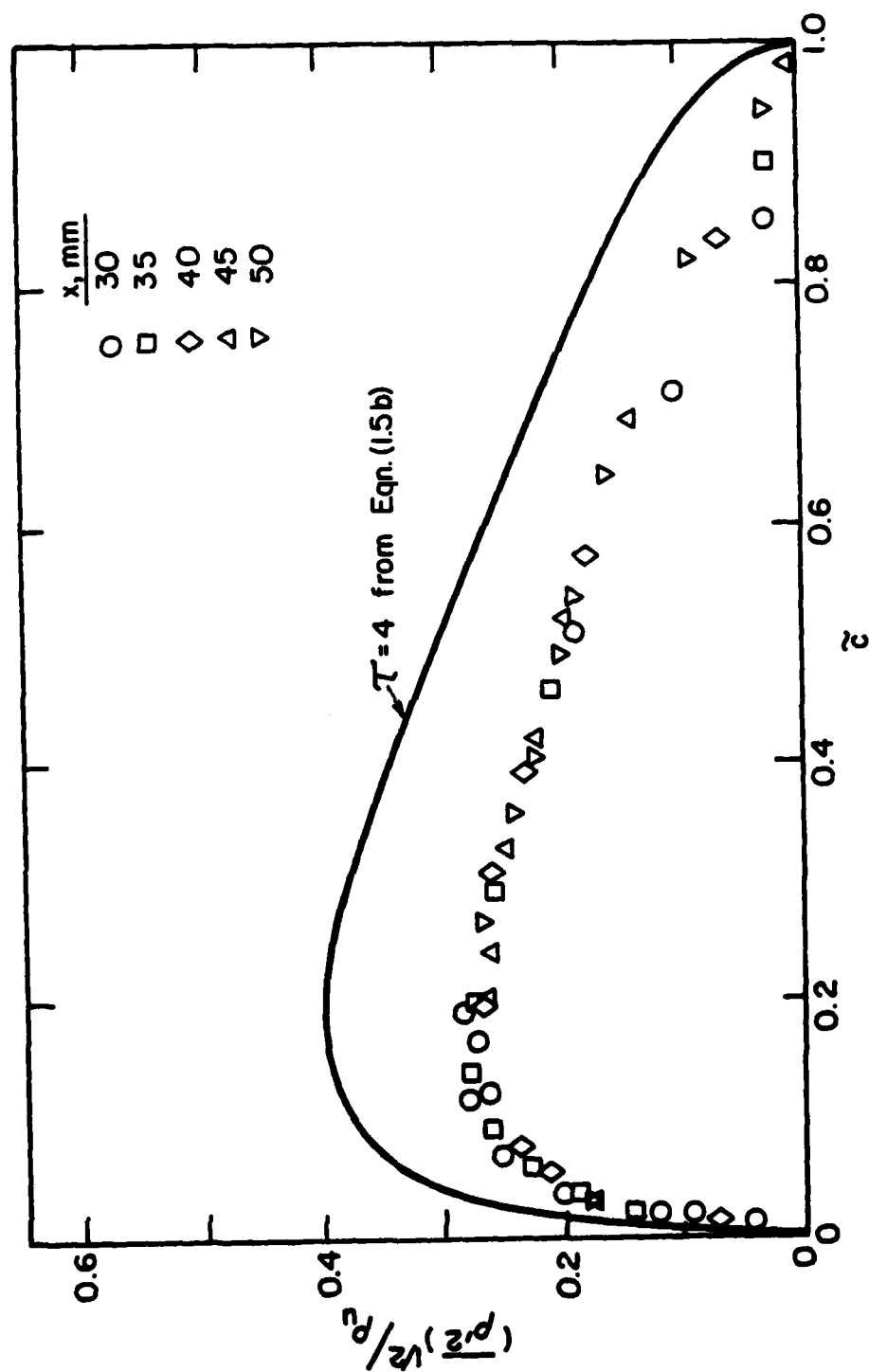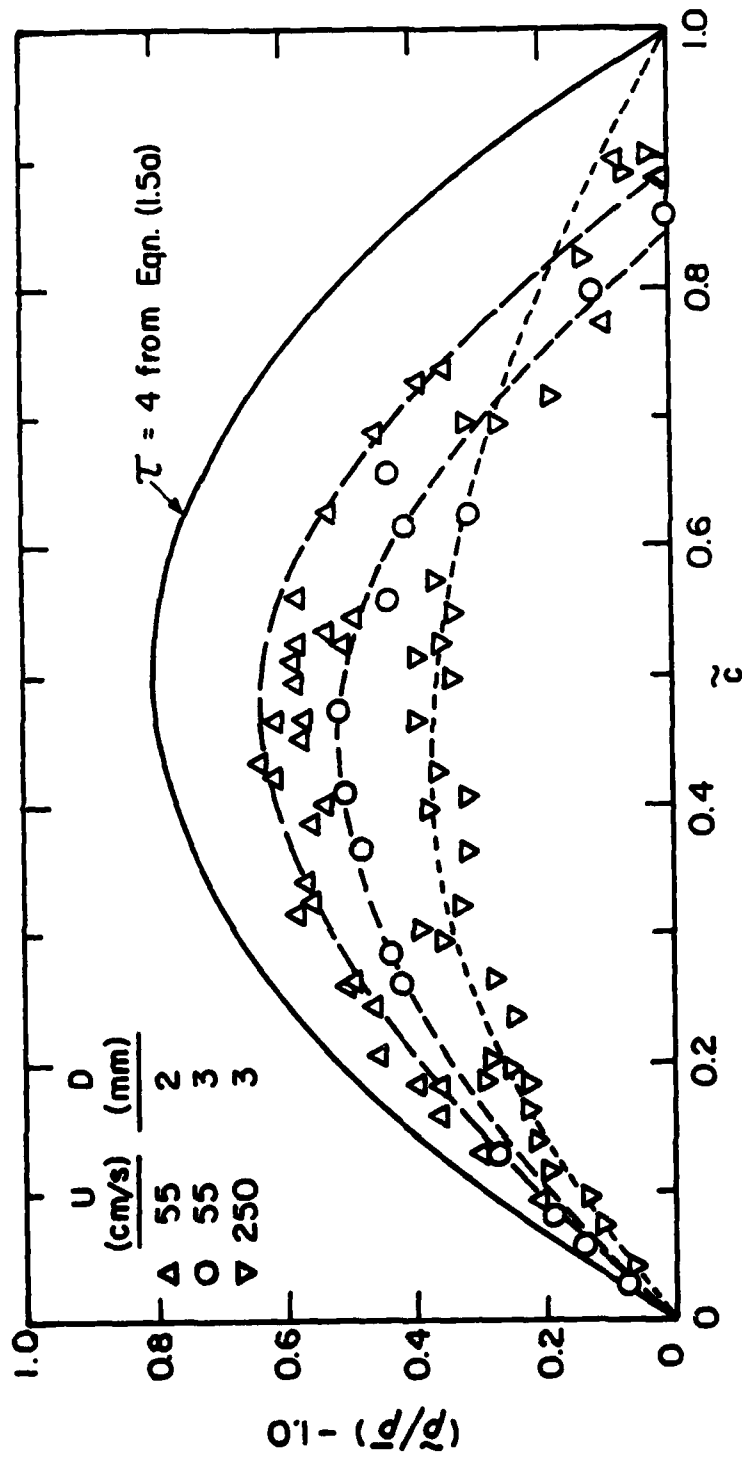
Figure 5.7

Figure 5.8

XBL 808-5616

Figure 5.9
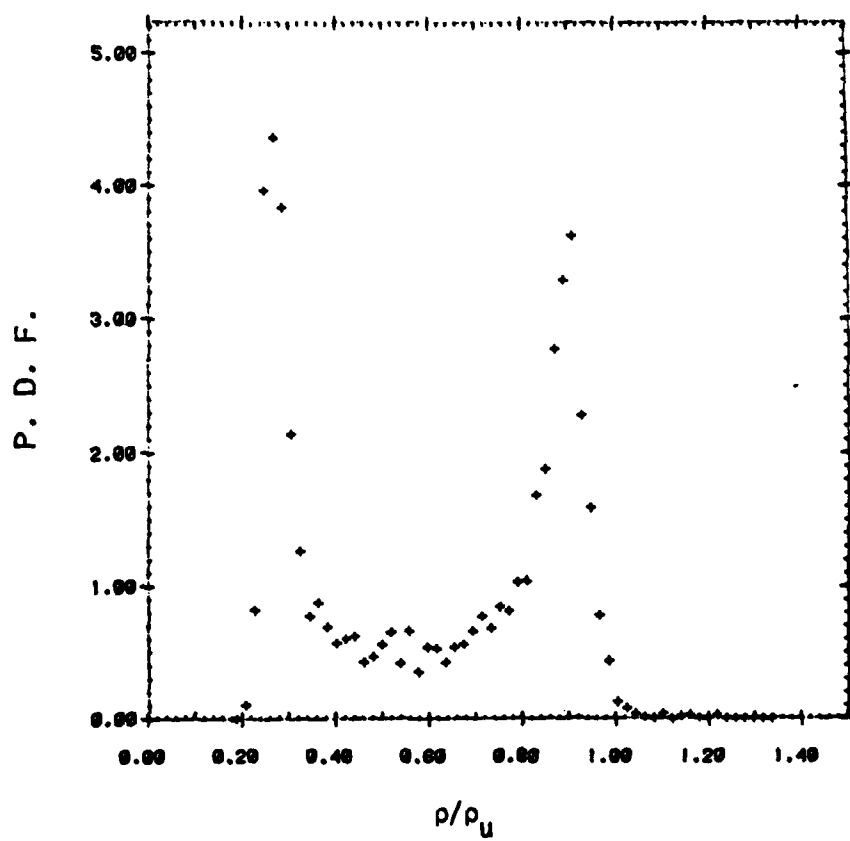
XBL 808-10836

Figure 5.10
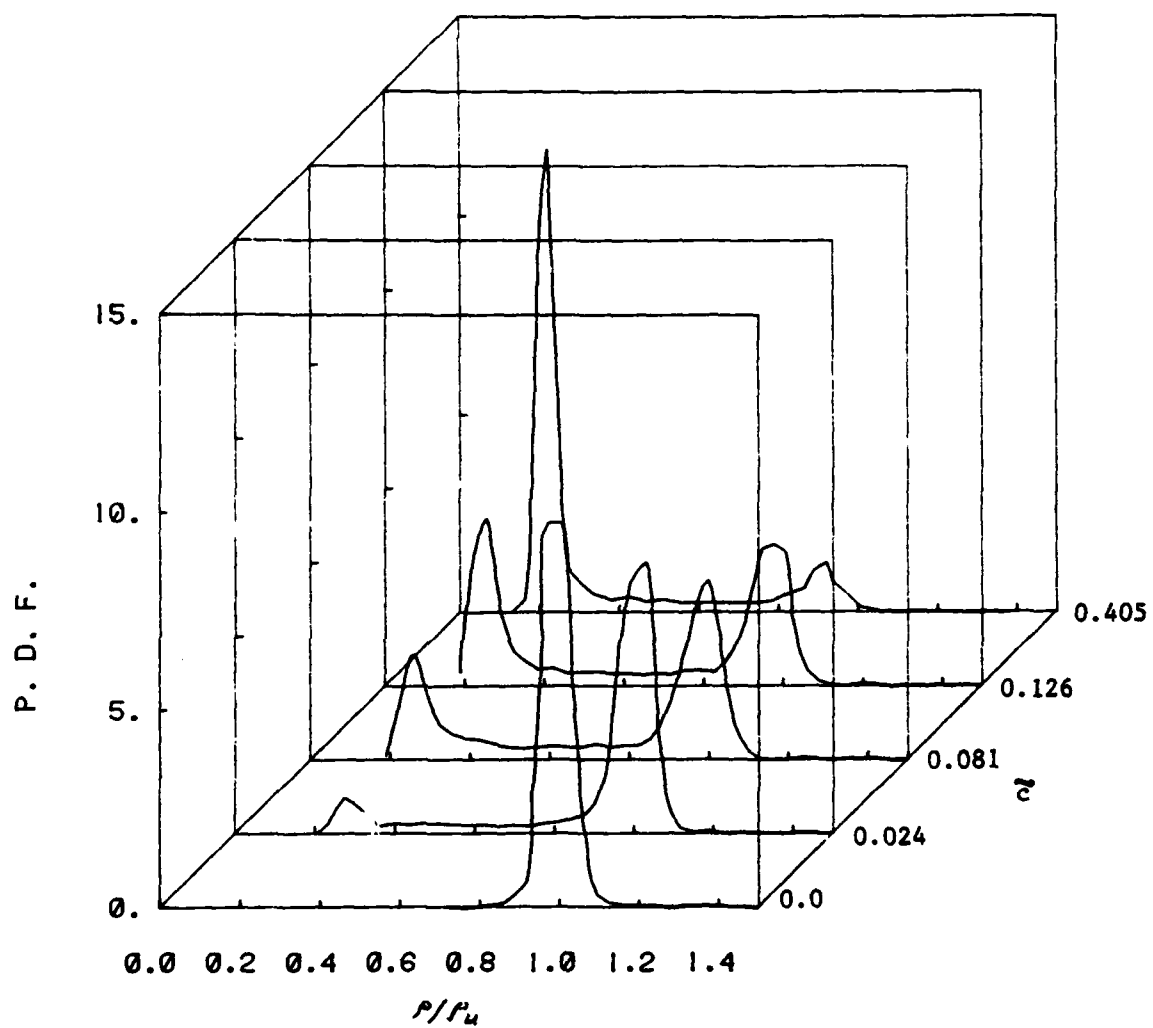
XBL 808-11109

Figure 5.11
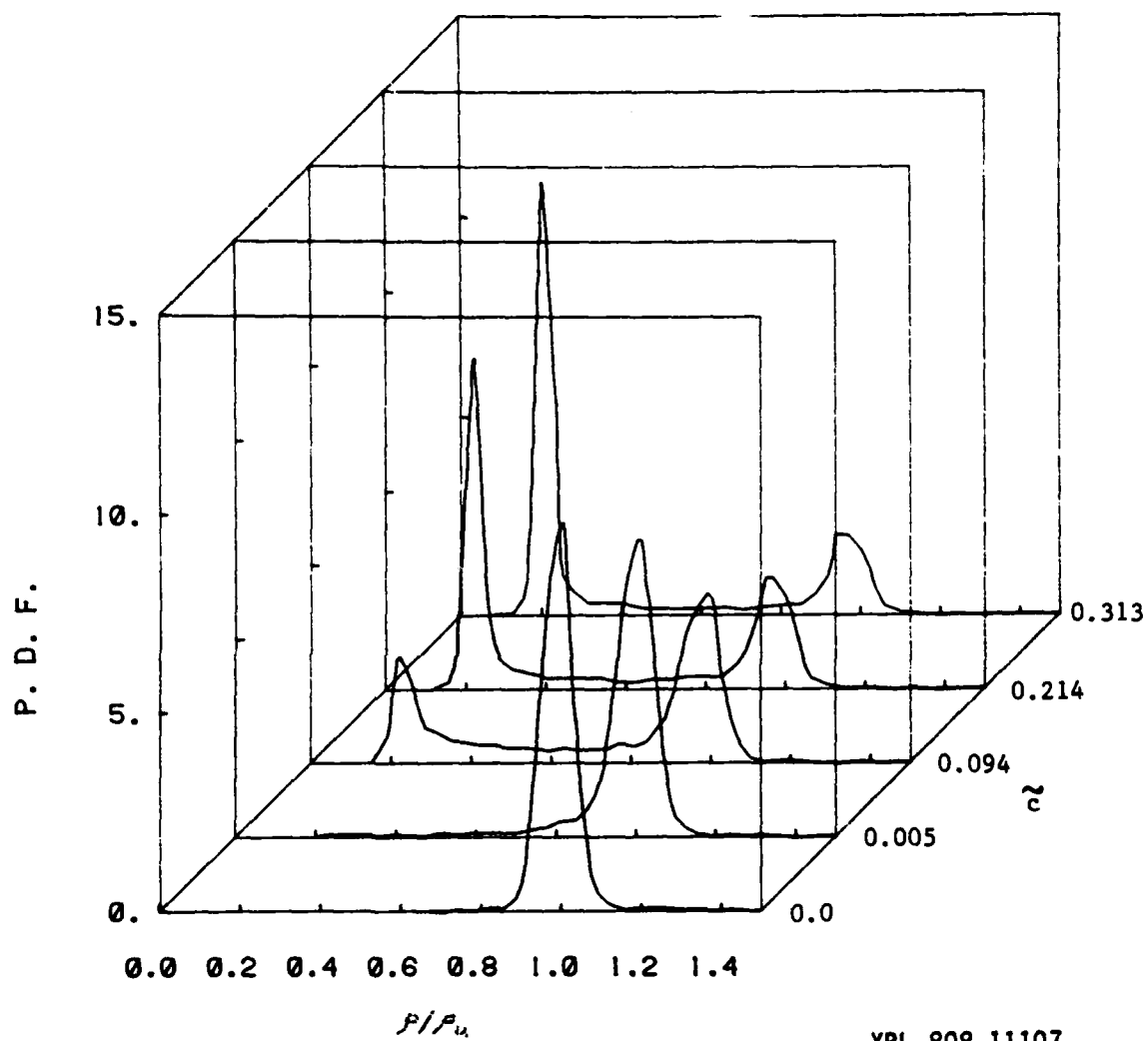
Figure 5.12

XBL 808-11107

P. D. F.

p / p_u

XBL 808-11108

Figure 5.13

XBL 808-5621

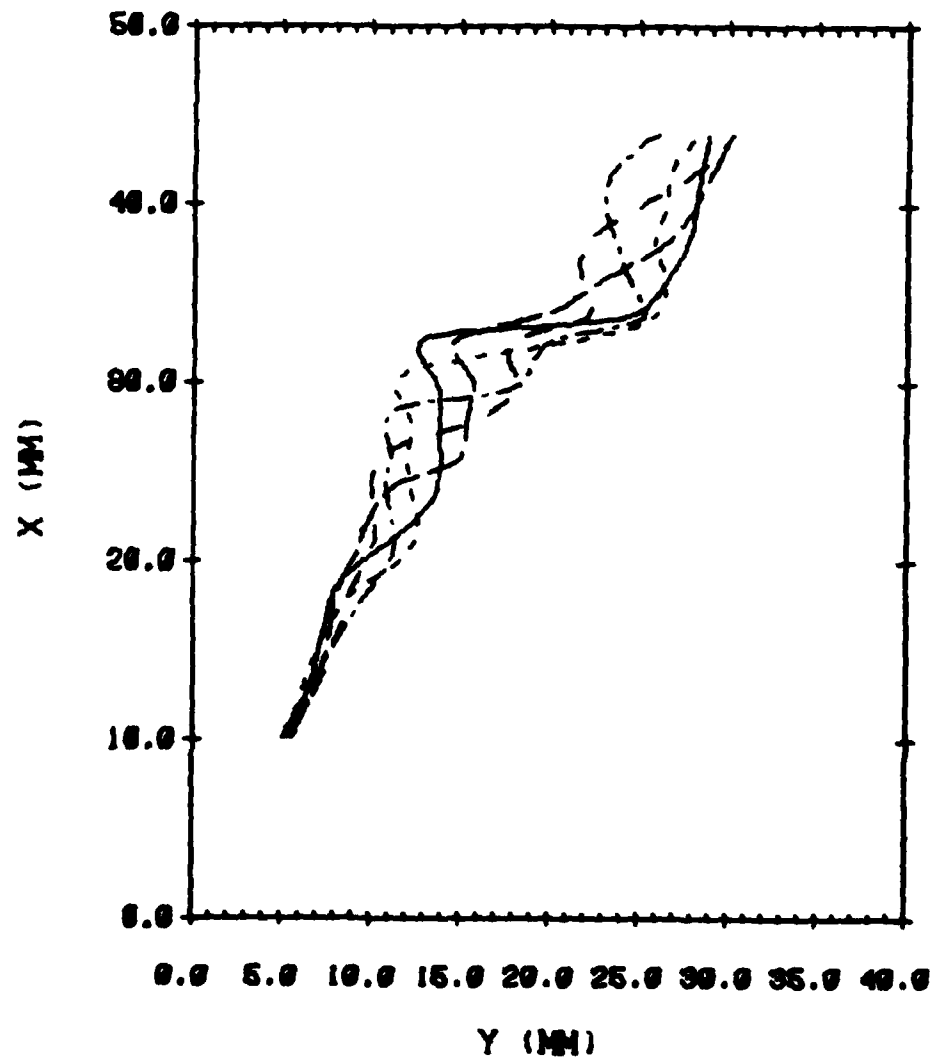Figure 5.14a

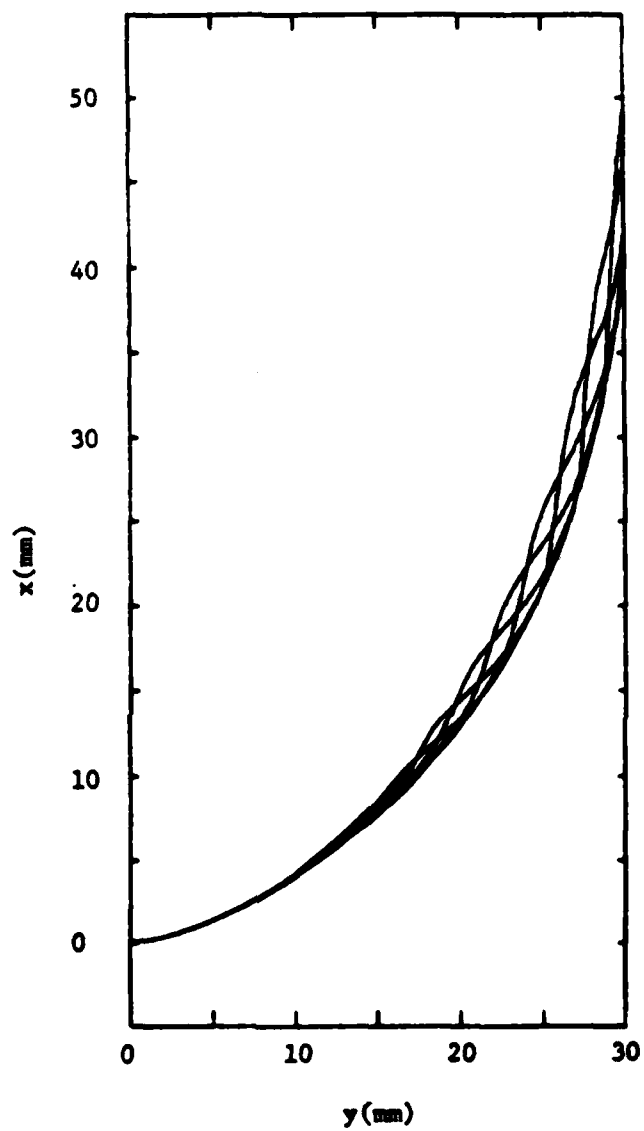Figure 5.14b

XBL 808-5622

Figure 5.14c
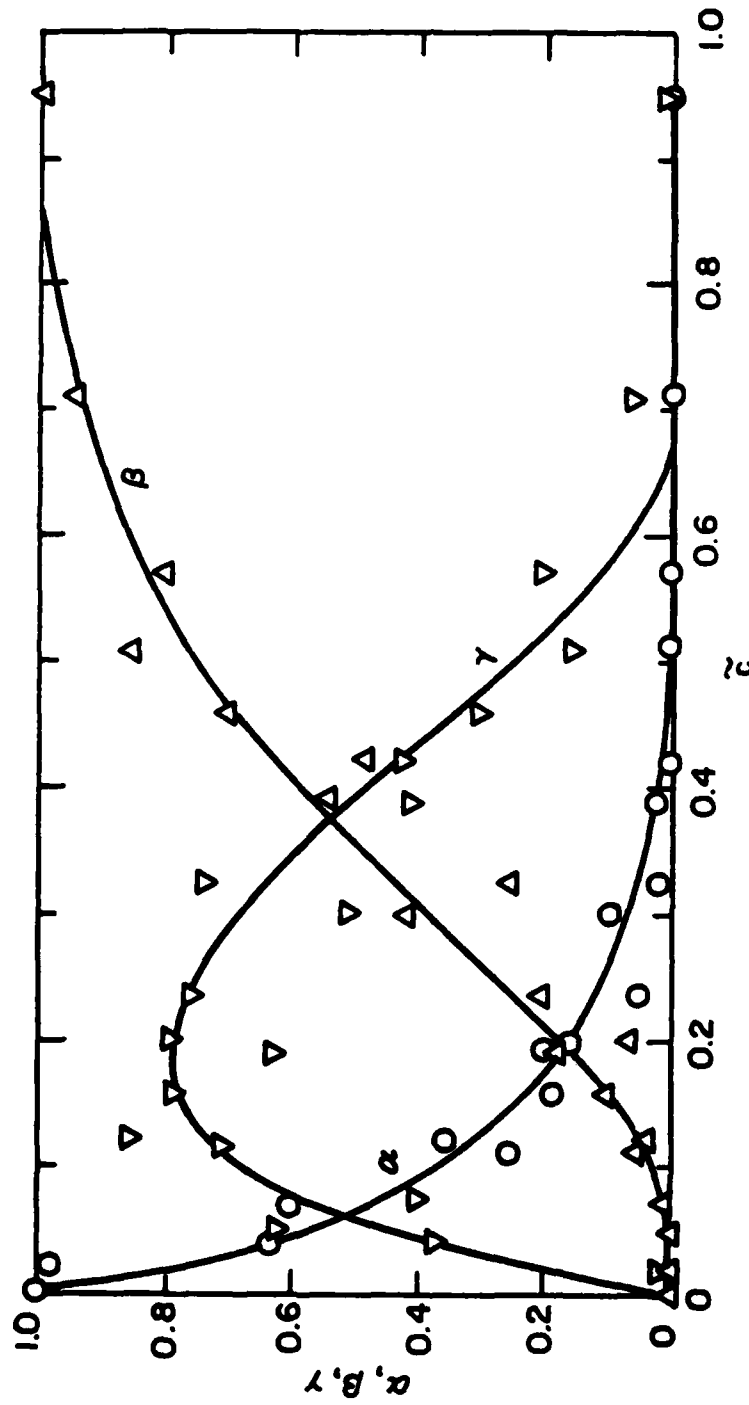
X BL 808-5620
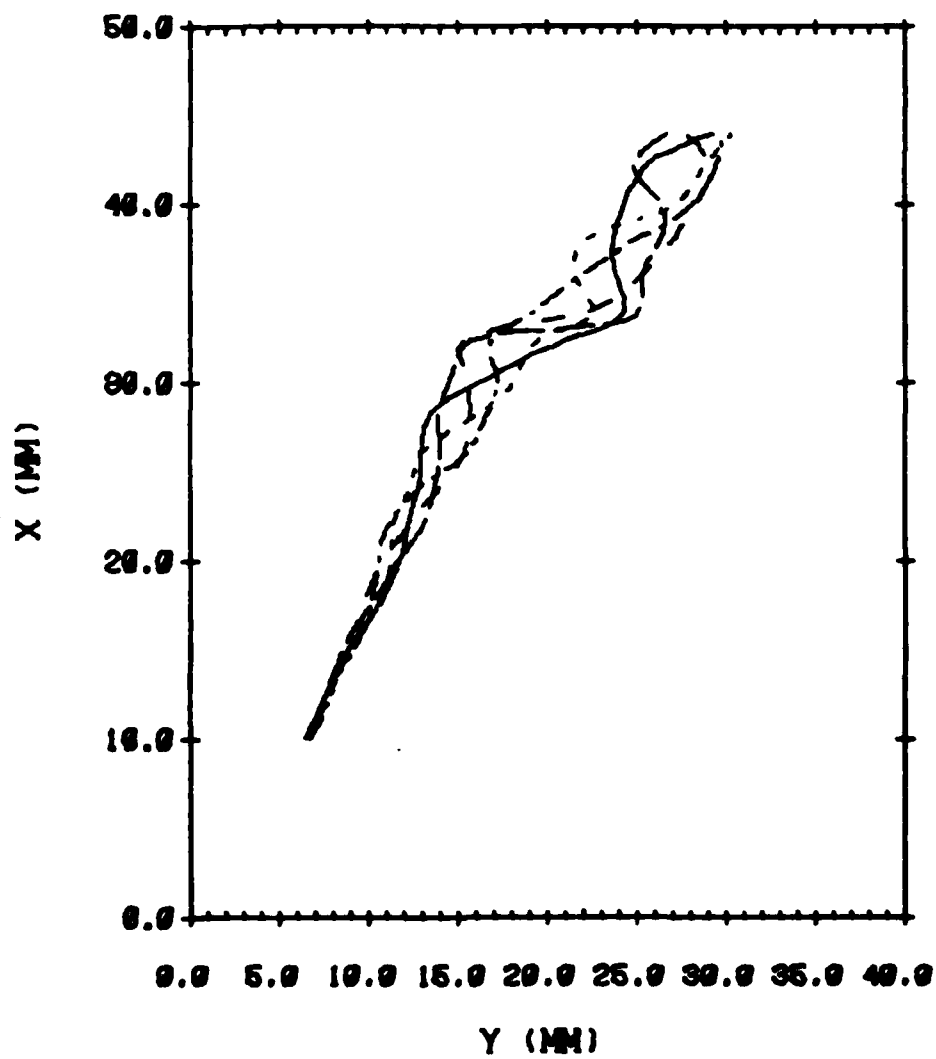
XBL 807-10673

Figure 5.15a

XBL 807-10672

Figure 5.15b

XBL 808-11110

Figure 5.16